



---

PHD THESIS

---

# Oceanic Vertical Mixing, Marine Biogeochemistry and Atmospheric Carbon Dioxide

---

*Author*  
Søren Borg Nielsen

*Academic advisor*  
Markus Jochum

*Department*  
Niels Bohr Institute,  
Physics of Ice, Climate and Earth

This thesis has been submitted to the PhD School of The Faculty of Science, University of Copenhagen, on January 31st, 2019 in partial fulfillment of the requirements of the PhD program







---

## Abstract

A key feature of the ocean circulation is the meridional overturning circulation, where warm surface waters flow from the tropics to high latitudes where they are cooled and sink. One of the key mechanisms for bringing deep water back to the surface is breaking internal waves that mix watermasses of different densities.

Despite its crucial importance to the ocean circulation, this process is often parameterized through diffusion of tracers using semi-empirical parameterizations of tidal induced mixing and a constant background diffusivity. While this method generally reproduces observed ocean circulation, issues arise from such parameterization: It is not energetically consistent, violating one of the key principles of physics, and it is tuned to match the modern day internal wave field, which is believed to have been significantly different in the past due to changes in wind and tidal forcing.

The ocean holds multiple times as much carbon as the atmosphere, and is therefore of key importance to the carbon cycle. Previous studies have shown that the vertical diffusivity is important for the global carbon cycle through its impact on ocean solubility and nutrient cycling. Thus, the current use of semi-empirical parameterizations that are tuned to present day climate may damp the ocean carbon cycle response to climate change.

A recently proposed parameterization for mixing induced by breaking internal waves is implemented in a general circulation model. The first set of simulations compares the climate simulated using the new and the existing semi-empirical parameterization. With the new parameterization the thermocline gets sharper and shallower, a result of too little dissipation in the thermocline compared to observations, and the overturning circulation is weaker and more sensitive to changes in Southern Ocean wind stress.

In the next set of simulations, two simulations using the new, energetically consistent, stratification-dependent mixing parameterization are performed, investigating the response of the carbon cycle to a collapse of the Atlantic Meridional Overturning Circulation. The global carbon cycle responds on two timescales, a centennial terrestrial release of carbon to the atmosphere, and a slow, centennial to millennial ocean outgassing. The terrestrial release is related to a southward migration of the tropical precipitation, the ocean response is due to a reduced productivity and a global ocean release of carbon to the atmosphere. The latter is in part caused by increased oceanic stratification, particularly in the Atlantic, which reduces the diffusive transport of nutrients to the surface ocean. This adds to the surface nutrient depletion caused by the increased North Atlantic freshening, which shoals the winter mixed layer that normally brings nutrients from the abyss to the surface ocean.

As a result it is demonstrated that, in line with previous studies, oceanic vertical mixing is of key importance to the global carbon cycle. The current paradigm for parameterizing vertical mixing results in the ocean stratification being less sensitive to climate change. To fully grasp the impact it has on the carbon cycle, the

---

response of ocean mixing to changes in ocean circulation must be better understood, and caution must be exercised when using constant background diffusivities in general circulation and Earth System models.

---

## Resumé

Et centralt element i klimasystemet er den termohaline cirkulation, hvor varme vandmasser fra troperne strømmer mod høje breddegrader, hvor de afkøles og synker til dybet. De dybe vandmasser bringes med tiden mekanisk tilbage til overfladen. En af de vigtigste mekanismer hertil er små-skala turbulens, hvor interne bølger bryder, hvilket sammenblander vandmasser af forskellig densitet og derved hæver havets massemidt punkt og øger den potentielle energi af systemet.

På trods af dens afgørende betydning for havcirkulationen parametriseres denne proces ofte gennem diffusion ved hjælp af en konstant baggrundsdiffusivitet samt en semi-empirisk parametrisering af tidevandsinduceret bølgebrydning. Selvom denne metode generelt reproducerer den observerede havcirkulation, er der flere problemer ved en sådan parametrisering: Den er ikke energibevarende, og bryder således et af fysikkens grundprincipper, og den er tunet til at reproducere det moderne interne bølgefelt, som menes at have været væsentligt anderledes i fortiden på grund af ændringer i vind- og tidevandsforcering af havet.

Havet opbevarer adskillige gange så meget kulstof som atmosfæren, og er derfor af afgørende betydning for kulstofkredsløbet. Tidligere studier har vist, at den vertikale diffusivitet er vigtig for det globale kulstofkredsløb grundet dens indvirkning på kulstofs opløselighed i vand, samt næringtoffernes cyklus. Således kan den nuværende anvendelse af semi-empiriske parametriseringer, der er indstillet til nutidens klima, dæmpe oceanets biogeokemiske respons på klimaforandringer.

I denne afhandling implementeres en nyligt udviklet parametrisering af vertikal diffusivitet i en global oceanmodel. Det første sæt af simulationer sammenligner klimaet som er simuleret ved brug af den nye og den eksisterende, semi-empiriske parametrisering. Termoklinen bliver stærkere og mindre dyb, hvilket skyldes for lidt dissipation i termoklinen sammenlignet med observationer, og den termohaline cirkulation er svagere og mere følsom over for ændringer i styrken af vindene over det Sydlige Ocean.

I det næste sæt af modelkørsler sammenlignes to simuleringer med den nye, energibevarende parametrisering, og kulstofkredsløbets reaktion på et sammenbrud af den termohaline cirkulation analyseres. Det globale kulstofkredsløb reagerer på to tidsskalaer, en århundredelig udledning af kulstof fra den terrestriske sfære til atmosfæren, og et langsomt udslip fra havet som virker over en tidsskala på hundreder til tusinder af år. Frigivelsen af plantebundet kulstof skyldes en sydlig migration af det tropiske nedbørsbælte, og havets udgasning skyldes et svækket marint økosystem og en global frigivelse af kulstof fra oceanet til atmosfæren. Oceanets vertikale diffusion reduceres globalt, især i Atlanterhavet, hvilket fører til en reduceret diffusiv transport af næringsstoffer til overfladehavet. Dette medvirker til overfladevandets udtømmning af næringsstoffer, hvilket i forvejen forårsages af den reducerede nordatlantiske salinitet, der udtønder det turbulente mixed layer, der normalt opretholder næringsstofsbalancen i Nordatlanten.

Således demonstreres det, i overensstemmelse med tidligere studier, at vertikal opblanding i havet er afgørende for det globale kulstofkredsløb. Som følge heraf

---

betyder det nuværende paradigme for parametrisering af vertikal opblanding, at havet er mindre følsomt over for klimaforandringer end det muligvis er i virkeligheden. For fuldt ud at forstå hvorledes det påvirker kulstofkredsløbet, skal ændringer i havcirkulationens påvirkning af småskala turbulens forstås bedre, og forsigtighed skal udvises ved anvendelse af konstante baggrundsdiffusiviteter i simulationer af fortidens og fremtidens klima.

---

## Acknowledgments

At the end of a blockbuster movie, the end credits list all the involved people without whom the film would undoubtedly be different. While it can hardly be compared to a blockbuster movie, the same dependency on other people goes for a scientific dissertation, but in its written form and without background music, tradition tells us to stick with a few honorable mentions. The following list is without doubt incomplete, and to those whom I have forgotten, please forgive my distracted nature.

I would like to thank my supervisor, Markus Jochum, without whom there is a non-zero chance this thesis would be in black and white. Thank you for giving me the opportunity to sail out on the scientific quest this has been, your supervision and for teaching me the value of academic storytelling. My office mate, Mads B. Poulsen, has been an integral part of my work, and I would not have been at this point without his good spirit and kindness, our recurring whiteboard discussions, scientific as well as existential, or his frequent discussions with himself. Roman Nuterman deserves much credit for all his technical assistance. Sorry for being a nuisance and filling up the cluster repeatedly. I am grateful to David Battisti and his group for having me for two valuable months at University of Washington, in the fantastic city of Seattle. I would also like to thank Marcus Dengler for inviting me to join the R/V Meteor on the M120 cruise, which provided me with useful understanding of observational oceanography, and Dorthe Dahl-Jensen and the EGRIP community for making it possible for me to spend a summer on the Greenland ice sheet. Both field experiences will be with me forever. Thanks to Carsten Eden and his group, particularly Friederike, Philipp and Manita, for the discussions in Hamburg and in the beautiful surroundings of the wonderful island of Bornö. I would also like to thank the Ice2Ice community for inviting me to meetings, bootcamps and the city of Bergen, and for the great friendships I found there. Of course, all current and past members of Team Ocean at NBI deserves my appreciation, particularly Helen Pillar and Jonas Blüthgen for their crucial help, especially during my first year, and Joel B. Pedro for bridging the gap between my simulations and the real world. The Rockefeller Institute, spanning Center for Ice and Climate and the Climate and Geophysics section, has been a great setting for work, and I am grateful to all colleagues and students, in particularly the lunch team Christian, Marius and Nicholas. My family and friends have been there for me for the entire duration of this adventure, and have played important roles in always keeping parts of my mind in the real world. Also, I am indebted to the StackExchange community.

Finally, the past few years would have been significantly different without Anna Arendse Thorsen, the strongest person I know and my biggest inspiration. Your endless support throughout particularly the past few months has been invaluable.

Søren Borg Nielsen  
Copenhagen, January 2019



# Contents

<b>1</b>	<b>Introduction</b>	<b>1</b>
<b>I</b>	<b>Theory and Background</b>	<b>5</b>
<b>2</b>	<b>Scientific Background</b>	<b>7</b>
2.1	The Last Glacial . . . . .	8
2.2	Internal Waves . . . . .	12
2.2.1	Internal Wave Theory . . . . .	12
2.2.2	Observations of Internal Waves . . . . .	13
2.2.3	Implications for the Ocean . . . . .	16
2.2.4	Modelling Vertical Mixing . . . . .	17
2.3	IDEMIX . . . . .	20
2.3.1	Parameter Choice . . . . .	25
2.3.2	Discussion . . . . .	27
2.4	Marine Carbon Cycle . . . . .	29
2.4.1	Surface Ocean Chemistry and Gas Transfer . . . . .	29
2.4.2	Changes in Ocean DIC . . . . .	31
2.4.3	Modelling the Marine Carbon Cycle . . . . .	35
<b>3</b>	<b>Methods</b>	<b>37</b>
3.1	CESM . . . . .	37
3.2	Implementation of IDEMIX . . . . .	40
3.3	Overview of Model Runs . . . . .	41
<b>II</b>	<b>Scientific Results</b>	<b>43</b>
<b>4</b>	<b>An energetically consistent vertical mixing parameterization in CCSM4</b>	<b>45</b>
4.1	Introduction . . . . .	47
4.2	Methods . . . . .	49
4.2.1	Vertical mixing in ocean models . . . . .	49
4.2.2	IDEMIX . . . . .	50
4.2.3	Model and Implementation . . . . .	52

4.3	Results . . . . .	55
4.3.1	Coupled simulations . . . . .	55
4.3.2	Forced experiments . . . . .	62
4.4	Summary and Discussion . . . . .	64
<b>5</b>	<b>Mixing and Marine Biogeochemistry</b>	<b>69</b>
<b>6</b>	<b>Two-timescale carbon cycle response to an AMOC collapse</b>	<b>75</b>
6.1	Introduction . . . . .	77
6.2	Methods . . . . .	79
6.2.1	Vertical mixing . . . . .	79
6.2.2	Model setup . . . . .	80
6.3	Results . . . . .	81
6.3.1	Land-atmosphere fluxes . . . . .	85
6.3.2	Ocean-atmosphere fluxes . . . . .	86
6.4	Discussion . . . . .	91
6.5	Summary and conclusions . . . . .	95
<b>III</b>	<b>Outlook and Discussion</b>	<b>97</b>
<b>7</b>	<b>Outlook</b>	<b>99</b>
7.1	Insolation and Mixing . . . . .	100
7.1.1	Stratification and Mixing . . . . .	102
7.1.2	Carbon Cycle . . . . .	105
7.2	Energy Sources . . . . .	107
7.3	Sea Ice Export . . . . .	111
<b>8</b>	<b>Summary and Conclusion</b>	<b>113</b>
	<b>Bibliography</b>	<b>117</b>
	<b>Appendix</b>	<b>136</b>
A	List of acronyms . . . . .	137
B	List of figures . . . . .	138
C	List of tables . . . . .	139





# Chapter 1

## Introduction

In addition to the value of knowledge itself, understanding climate is of great socio-economic importance to mankind. With reliable decadal and centennial predictions of climate humans can mitigate and adapt in due time to variations in regional temperature, precipitation and sea level rise (or fall). In order to predict climate change we rely on detailed physical, biological, chemical and mathematical understanding of climate so that scientists can confidently build advanced numerical models, the foundation of climate prediction. In building such advanced models, the scientist, using her understanding of climate, must decide what physics and equations are necessary to solve in order to simulate climate satisfactorily. Because of limited computational resources, a key decision concerns what the smallest spatial scale that must be explicitly resolved in the model is in order to account for all geophysical or biogeochemical process important to the climate system. The answer to this question is most likely a spatial resolution that will never be possible to attain for a global climate model. In the ocean, small scale turbulence, despite a characteristic length scale down to a few centimeters, plays a critical role in maintaining the ocean stratification ([Munk, 1966](#)).

As a result, climate modelers are forced to parameterize the effect of unresolved processes that are important to the resolved large-scale climate. Most physical parameterizations introduce a suite of variables and parameters. Some are well-known, some are not. The sum of all parameterizations make up much of the variability between climate models. This leads to a large amount of the work of the climate modeling community to be focused on improving the parameterizations of the models and estimating from theory or observations what the parameters in each parameterization should be.

While much work is devoted to improving model representation of pre-industrial and contemporary climate, improving the way scientists parameterize sub-grid processes also has potential for unlocking physics that was previously absent in the model.

The present work strives investigate the potential feedbacks arising from parameterizing internal wave breaking in an energetically consistent framework. Such feedbacks are presently either damped or completely missing in most ocean models due to parameterizations including relatively high background diffusivities that are fixed in space and time. This choice also leads climate models to break one of the basic foundations of all physics: energy conservation (*Eden et al., 2014*). Hence, implementing new parameterizations of internal wave breaking in climate models is important because it has potential to improve the physical representation of internal wave breaking and mixing, and thus allows scientists to investigate the importance of feedback mechanisms that were not previously in the model. The cost comes in the shape of potentially increased computation time and numerical noise in the model.

One particular component of the climate system that is still subject to great uncertainties regarding climate predictions is the carbon cycle. Given continued anthropogenic emissions of carbon, it is important to know how large a fraction of the excess carbon in the atmosphere ends up in the ocean, and how it affects the marine ecosystem and climate as a whole (*Hoffman et al., 2014*). Answering these questions requires a detailed understanding of the carbon cycle in the past. In particular, to trust the predictions of future climate, we must be able to simulate the past, which has proven difficult. In particular, the roughly 100 ppmv difference in atmospheric pCO<sub>2</sub> between glacial and interglacials remain unanswered (*Kohfeld and Ridgwell, 2009*). So far, fully coupled general circulation models have failed to reproduce these excursions in pCO<sub>2</sub>, which in part is explained by the heavy numerical cost of running these models for millennia which is required for glacial timescales. Furthermore, we must ask ourselves whether all processes that are important in the global carbon cycle are included in the models.

Vertical mixing affects the heat storage and overturning of the ocean (*Bryan, 1987*), thus affecting ocean solubility and nutrient cycling (e.g. *Marinov and Gnanadesikan, 2011*). Focus is therefore on the role of vertical mixing on the carbon cycle. Previous studies suggest that the ocean stratification and circulation was different during the last glacial compared to today (e.g. *Jansen, 2016*). Furthermore, the suppressed sea level increased energy input to internal waves through barotropic

tides, which would have increased vertical mixing by breaking of internal waves (*Wilmes and Green, 2014*). Therefore, it is crucial to understand to what extent these changes might have influenced the carbon cycle in the past, in order to identify how they will affect the climate in the future.

The goal of this thesis is to illuminate these questions. How does vertical mixing respond to climate change when it is allowed to vary in space and time, and how does it affect the global carbon cycle? This is done by implementing a new parameterization of vertical mixing in a general circulation model and assessing the response of the carbon cycle to perturbations of the climate system.

### Outline

The thesis contains three parts. Part I presents the background theory and methods that are used throughout the thesis and consists of Chapter 2 and 3. Chapter 2 introduces basic theory and concepts used in Part II and III. A brief overview of the climate over the past 100,000 years is given, and internal waves in the ocean are briefly reviewed. This includes the way they are traditionally represented in ocean models, as well as introducing a recently proposed mixing parameterization (*Olbers and Eden, 2013*). Finally, some key concepts regarding the carbon cycle are presented. It is not always clear who the reader of a scientific dissertation is, apart from the assessment committee evaluating the work. Therefore, Chapter 2 dedicates some time to introduce basic concepts of oceanography, biogeosciences and climate science that are important for the rest of the thesis, aiming to make the content accessible to a broader audience with background in just one of these fields. Chapter 3 introduces the model that is used in the thesis and the implementation of the mixing parameterization in it.

Part II presents the main results of the thesis. These are presented in the form of scientific journal papers, the traditional scientific way of conveying knowledge. As a result, some overlap between part I and II will occur. The first paper, Chapter 4, presents the implementation of an energetically consistent vertical mixing parameterization in a fully coupled climate model. The key focus is surface climate, energetics and circulation. Chapter 5 briefly extends these results by presenting model results coupled to an active biogeochemistry module. The second scientific paper, Chapter 6, investigates a drastic circulation change induced by a perturbation in solar insolation and what effect this has on vertical mixing, atmospheric CO<sub>2</sub> concentrations and the marine ecosystem.

Finally, in Part III, preliminary work and supplementary comments to the scientific results are presented in Chapter 7, including model simulations using different insolation forcing and mixing parameterizations. Chapter 8 summarizes and concludes the main findings of the thesis.

# Part I

## Theory and Background



## Chapter 2

# Scientific Background

Climatic variables such as temperature and precipitation require careful measurements to correctly quantify. As a result observations of temperature only dates back to the invention of the thermometer. To quantify what the temperature (or any other climatic variable) was before the instrumentation the climate community turns to climate proxies.

Climate proxies are archives where the composition of a given material, for instance sediments or ice, is indicative of past climate. An example of a proxy is the relative abundance of a specific foraminiferal species in ocean sediments. Different species prefer different ocean conditions (warm or cold, fresh or salty), and the census count of foraminiferal fauna therefore indicates the past ocean conditions of the region in which they were deposited in sediments (e.g. [Govin et al., 2012](#)).

Throughout this thesis there will be references to different proxies as these are the foundation of understanding past climate. A common concept for many climate proxies is a process known as Rayleigh fractionation. Phase transitions, for instance the evaporation of liquid water to water vapor, favor the evaporation of lighter oxygen and hydrogen isotopes to the heavier. The ratio of light to heavy isotopes depends on the conditions under which the transition occurs, particularly temperature ([Dansgaard, 1964](#)). Thus, the ratio of water stable isotopes in precipitation indicates the temperatures at which the evaporation and condensation took place. The isotopic ratio is often expressed in  $\delta$ -notation:

$$\delta = (R_X/R_S - 1) \cdot 1000\text{‰}, \quad (2.1)$$

where  $R_X$  denotes the sample ratio of heavy to light isotopes and  $R_S$  denotes a ref-

erence standard ratio. Fractionation occurs in several processes: evaporation and condensation of water, photosynthesis, formation of calcite and so on. If treated carefully, many deposits, sediments or ice layers, may be interpreted as a function of the local or regional climate at the time of deposition. However, it is important to keep in mind that fractionation is an integral process, and that the isotopic signal of e.g. snow on top of Greenland is a function of the temperature and isotopic signal of the water at the time of evaporation, the cooling process from evaporation to deposition, and temperature at time of condensation. Thus, converting a proxy record into a temperature record in terms of absolute temperature is problematic, and often the climate community is left with qualitative data that suggest e.g. either warming or cooling, without knowing the magnitude.

## 2.1 The Last Glacial

From proxy records it is possible to extract climate data from the past, extending back thousands or millions of years, depending on the record. The  $\delta^{18}\text{O}$  record from the Greenland Ice Core Project (GRIP, [Dansgaard et al., 1993](#)) is plotted in Figure 2.1. While the period from 0 to about 12000 years before the Common Era (BCE), the interglacial known as the Holocene, is characterized by a very stable climate over Greenland, the last glacial, from about 12000 to 119000 BCE<sup>1</sup>, shows large and often rapid variability, indicating dramatic shifts in the local climate. The rapid excursions to higher  $\delta^{18}\text{O}$  values are known as Dansgaard-Oeschger events (DO events).  $\delta^{15}\text{N}$  measurements suggest that these represent rapid warming of 5-15°C ([Huber et al., 2006](#); [Kindler et al., 2014](#)), while  $\delta^{18}\text{O}$  and  $\delta\text{D}$  (deuterium,  $^2\text{H}$ ) suggest that some warming events took place over few years ([Steffensen et al., 2008](#)). Several DO events follow a similar pattern: the rapid warming is typically followed by gradual cooling for a period of time until a rapid cooling ends the cycle (e.g. [Dokken et al., 2013](#)). Cold periods are referred to as Greenland stadials, whereas the warmer periods are called Greenland interstadials. For this thesis, we simply refer to these as stadials and interstadials. Within the last glacial, about 25 DO events are observed in the Greenland ice core records ([Rasmussen et al., 2014](#)).

The DO events are climatic features that have impact way beyond the regional climate over Greenland. Proxy records from all over the world capture rapid

---

<sup>1</sup>timings based on [Rasmussen et al. \(2014\)](#)

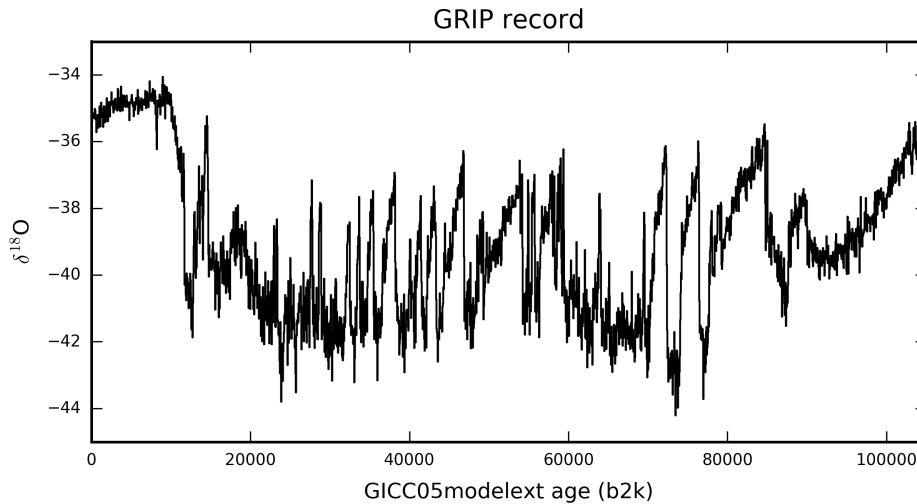


**Figure 2.1:** The GRIP  $\delta^{18}\text{O}$  record for the Holocene and the last glacial (*Dansgaard et al., 1993; Rasmussen et al., 2014; Seierstad et al., 2014*).

changes occurring at the same timescale as DO events. Lake sediments from Europe indicate rapid changes in vegetation (*Allen et al., 1999*), speleothems reveal drastic changes in precipitation over China (*Wang et al., 2001*) as well as South America (*Wang et al., 2006; Kanner et al., 2012*), indicative of meridional shifts in the location of the Intertropical Convergence Zone (ITCZ). Marine sediments in the North Atlantic point towards reduced, and at times even halted, deep Atlantic circulation (*Böhm et al., 2015; Henry et al., 2016*), and the North Atlantic experienced drastic changes in sea ice cover (*Dokken et al., 2013*).

The drastic climatic shifts are not as pronounced on the southern hemisphere counterpart to the Greenland ice sheet, the Antarctic ice sheet. There, modest Antarctic warming of few degrees occurred out of phase with the Greenland warming events (*EPICA community members, 2006; WAIS Divide Project Members, 2015; Markle et al., 2017*). Antarctic warming terminated in so-called Antarctic isotope Maxima (AIM) events, after which  $\delta^{18}\text{O}$  and  $\delta\text{D}$  decreased, corresponding to a cooling. Atmospheric concentrations of carbon dioxide ( $\text{pCO}_2$ ), measured from the air bubbles trapped in ice cores, increased in times of warming over Antarctica (*Ahn and Brook, 2008*), most pronounced during longer stadials (*Ahn and Brook, 2014*). Increasing  $\text{pCO}_2$  was found to lag the warming of Antarctica (*Bereiter et al., 2012*), suggesting that the warming is not caused by the release of greenhouse gases. However, the exact chronology of DO events remains to be disentangled.

Related to some, but not all, DO events are large grains of rock deposited in marine sediments far from the shore, indicative of iceberg discharge from polar ice caps. Distinct layers of ice-rafted debris (IRD) have been identified in the Atlantic seabed, known as Heinrich events (*Bond et al., 1992*). Heinrich events follow the longest stadials, the same that are associated with release of CO<sub>2</sub> to the atmosphere (*Ahn and Brook, 2014*) and weakest deep North Atlantic circulation (*Henry et al., 2016*).

The mere knowledge of DO events has naturally resulted in numerous hypotheses on what mechanisms are the driving force of DO events. Several "triggers" have been proposed: internal ocean or sea ice variability (*Li et al., 2005; Dokken et al., 2013; Peltier and Vettoretti, 2014*), large volcanic eruptions (*Baldini et al., 2015*), freshwater forcing of the North Atlantic (*Ganopolski and Rahmstorf, 2001*), buildup and instabilities in Greenland ice shelves (*Petersen et al., 2013*) or stochastic forcing from the atmosphere (*Kleppin et al., 2015*) are among the candidates. Using simple or complex models, each mechanism can be tested and evaluated regarding the skill at which it replicates the observed proxy records.

One feature that needs to be simulated is the apparent anti-symmetry between the hemispheres seen as the meridional shifts in precipitation (*Wang et al., 2006; Kanner et al., 2012*) and the warming of the Antarctic ice sheet during Greenland stadials (*WAIS Divide Project Members, 2015*). A popular concept invoked to explain the hemispheric anti-symmetry is the so-called "bipolar seesaw" (*Broecker, 1998; Stocker and Johnsen, 2003; Pedro et al., 2018*). The present day ocean circulation of the Atlantic transports warm surface waters from the southern hemisphere to the northern hemisphere where the waters are eventually cooled and sink, returning as a deep flow from the north to the south, where waters are upwelled mechanically by winds or diapycnal mixing (*Toggweiler and Samuels, 1995; Munk and Wunsch, 1998; Talley, 2013*). The result is a net heat transport from the southern hemisphere to the northern through the Atlantic Ocean (*Ganachaud and Wunsch, 2000*). Perturbations to this circulation have been hypothesized to lead to significant changes in heat transport (*Broecker, 1998; Stocker and Johnsen, 2003*), and numerous model studies have shown warming in the southern hemisphere as a result of reduced Atlantic Ocean northward heat transport (e.g. *Schmittner et al., 2003; Brown and Galbraith, 2016; Pedro et al., 2018*).

In general, a weakening of the AMOC explains a large suite of the climatic features of stadials observed in proxy records: the bipolar seesaw, expansion of North Atlantic sea ice and the reduced deep Atlantic circulation. Southward shifts in

equatorial precipitation has also been shown to be explained by AMOC reductions, resulting from an atmospheric compensation in the heat transport (e.g. *Broccoli et al., 2006*).

One feature that remains to be explicitly simulated is the rise in atmospheric  $p\text{CO}_2$  during stadials. One reason is that most attention has been directed towards explaining the glacial/interglacial differences in  $p\text{CO}_2$  of up to 100 ppmv (parts per million, *Sigman and Boyle, 2000*), rather than the more modest stadial/interstadial changes of maximum 20 ppmv (*Ahn and Brook, 2008*). Yet, some of the same mechanisms have been invoked and discussed. Due to the apparent phasing of Antarctic temperatures and  $p\text{CO}_2$  (*Ahn and Brook, 2008*), many theories focus their attention on the Southern Ocean. A popular explanation is an increased upwelling of deep, carbon rich waters and outgassing of carbon (*Anderson et al., 2009*). This hypothesis is based on the observation of increased opal fluxes to sediments in the Southern Ocean, best explained by increased productivity due to increased upwelling of nutrients and carbon.

The hypothesis is further supported by evidence of increased ventilation of deep waters measured as a decrease in ventilation age from radiocarbon measurements (*Gottschalk et al., 2016*) as well as increased oxygenation from authigenic uranium measurements (*Jaccard et al., 2016*). Changes in sea ice cover (*Stephens and Keeling, 2000*) or wind stress (*Toggweiler et al., 2006*) could explain the increased upwelling and outgassing.

Model studies have investigated the biogeochemical climate response to fresh-water forcing in the North Atlantic. However, results have been contradictory. While some suggest the ocean to act as a sink for carbon during an AMOC collapse (e.g. *Menviel et al., 2008*), others have found the ocean to be a source of atmospheric carbon (*Schmittner and Galbraith, 2008*). Many previous model setups employ simple models for the atmosphere, which has consequences for both the tropical rainfall patterns and the salinity balance of the global ocean (*Menviel et al., 2014; Schmittner and Lund, 2015*). We wish to investigate the ocean response to an AMOC collapse induced by insolation changes, given that the vertical mixing is fully allowed to vary due to changes in ocean stratification, while also employing an atmospheric model of increased complexity and fully coupled to the ocean model. To continue, brief introductions to internal waves and the carbon cycle are needed.

## 2.2 Internal Waves

This section aims to briefly introduce internal waves in the ocean. Focus is on the theoretical framework, observations and how they are parameterized in general circulation models. The topic of internal waves is huge, and a complete review would easily span hundreds of pages. For more thorough discussions the reader is referred to reviews or textbooks (e.g. [Munk, 1981](#); [Gill, 1982](#); [Pedlosky, 2003](#)).

### 2.2.1 Internal Wave Theory

#### Mathematical Description

For many subjects in oceanography it is illuminating to begin with the equations of motion for a rotating fluid. Internal waves are no exception. For waves we are interested in solutions to the time dependent momentum equation:

$$\rho \left( \frac{\partial \vec{u}}{\partial t} + \vec{u} \cdot \nabla \vec{u} + 2\vec{\Omega} \times \vec{u} \right) = -\nabla p + \mu \nabla^2 \vec{u} + \nu \nabla (\nabla \cdot \vec{u}) + \rho \vec{g}. \quad (2.2)$$

Here,  $\rho$  is the fluid density,  $\vec{u} = (u, v, w)$  is the three-dimensional velocity vector,  $\nabla = (\partial/\partial x, \partial/\partial y, \partial/\partial z)$  is the three-dimensional differential operator,  $\Omega$  is the angular velocity of the non-inertial reference system,  $p$  is the pressure,  $\mu$  and  $\nu$  the viscous parameters and  $\vec{g} = (0, 0, -g)$  is the gravitational acceleration vector.

For an adiabatic interior, Eq. 2.2 can be simplified through linearization under hydrostatic and Boussinesq approximations. Assuming frictionless flow, incompressibility ( $\nabla \cdot \vec{u} = 0$ ) and constant stratification and defining  $\rho = \rho_0 + \rho'$ ,  $\rho' \ll \rho_0$ , Eq. 2.2 can be manipulated in order to obtain an equation for the vertical displacement of a fluid (see e.g. [Pedlosky, 2003](#))

$$\frac{\partial^2}{\partial t^2} (\nabla^2 w) + f^2 \frac{\partial^2 w}{\partial z^2} + N^2 \nabla_h^2 w = 0, \quad (2.3)$$

where  $N$  is the Brunt-Väisälä frequency given by

$$N^2 = -g \rho_0^{-1} \frac{\partial \rho_0}{\partial z}, \quad (2.4)$$

$f = 2 \sin \theta$  is the coriolis frequency at latitude  $\theta$  and  $\nabla_h$  is the horizontal differential operator. The solution to Eq. 2.3 is a plane wave of the form

$$w = w_0 e^{i(kx + ly + mz - \omega t)}, \quad (2.5)$$

with the wavenumber vector  $\vec{K} = (k, l, m)$  and amplitude  $w_0$ , and the dispersion relation yields a frequency given by

$$\omega^2 = \frac{f^2 m^2 + N^2 (k^2 + l^2)}{k^2 + l^2 + m^2}, \quad (2.6)$$

or

$$\omega^2 = f^2 \sin^2 \varphi + N^2 \cos^2 \varphi, \quad (2.7)$$

where  $\varphi$  is the angle between the wave vector and the horizontal plane,  $(x, y)$ . As a consequence, internal waves are bounded by the local inertial frequency,  $f$ , and stratification. The frequency is determined by the angle it makes with the horizontal, and the group velocity is directed orthogonally to the wave vector.

### 2.2.2 Observations of Internal Waves

Observing the internal wave field of the ocean requires dropping, towing and deploying instruments in the water column to measure tracers (primarily temperature, salinity and oxygen concentrations) and velocities below the surface ocean. For understanding the internal waves and small scale turbulence of the ocean, measurements of tracers and velocities require long campaigns to resolve the relevant timescales, and three-dimensional arrays of instruments are needed to resolve the spatial scales.

As seen from Eq. 2.7, internal waves span a continuum of frequencies, bounded by the local inertial and buoyancy frequency. At the same time, frequencies are independent of the magnitude of the wave vector, and thus internal waves allow for a continuum of wavelengths as well, bounded by the shape and geometry of the ocean basin. By combining observational power spectra of observations at the time, *Garrett and Munk (1972)* proposed an empirical power spectrum for the wavenumber-frequency space, today referred to as the GM spectrum<sup>2</sup>. While empirically derived, and assuming that the observed motions are dominated by horizontally isotropic and vertically symmetric waves, the GM model (later modified more than once, *Garrett and Munk, 1975; Munk, 1981*) showed success in describing the observed wavefield in different locations. Several models of internal wave energy have therefore since assumed the internal wave field to be represented by the GM spectrum in frequency-wavenumber space, although work is still needed

---

<sup>2</sup>GM will throughout the thesis refer to *Garrett and Munk* and should not be confused with the *Gent and McWilliams (1990)* parameterization of mesoscale eddies.

to fully explain the shape of the GM spectrum. One fundamental question is what determines the propagation and interaction of internal waves, from generation to dissipation.

### Generation and Dissipation

At equilibrium, the total energy of the internal wave field is balanced such that the energy input from sources is equal to the sinks of internal wave energy. From generation to dissipation, waves propagate through physical space and are subject to resonant triad interactions, fluxing energy across wavenumbers (see e.g. [Olbers, 1983](#)). Thus, the generation of internal waves determines the overall structure of the internal wave field, and variations in the generating or dissipating mechanisms have implications for the ocean circulation.

One key feature of internal wave generation is the interaction between topography and currents, where the ocean floor through wave drag on the flow generates internal waves. Tidal flow in particular, generating internal waves of tidal frequencies, has received much attention since [Bell \(1975\)](#) used linear theory to derive an estimate of the global energy flux from tides,  $E_F$ , calculated as ([Jayne and St. Laurent, 2001](#)):

$$E_F \simeq \frac{1}{2} \rho_0 k h^2 N u^2, \quad (2.8)$$

where  $u$  is the speed of the tidal current,  $N$  is the Brunt-Väisälä frequency at the seabed, and the topography is characterized by wavenumber  $k$  and amplitude  $h$ .

Estimates of the total tidal dissipation yields values around a total of 3.5 terawatts (TW, 1 TW =  $10^{12}$ W), of which the deep ocean dissipation, which enters the internal wave field, is roughly 1 TW ([Egbert and Ray, 2000](#); [Jayne and St. Laurent, 2001](#); [Nycander, 2005](#); [Wilmes and Green, 2014](#)). The greatest uncertainties in these estimates are the bottom stratification and roughness.

Given the large input of energy from tides to internal waves, paleotides might have played an important role in modifying global dissipation rates through internal wave breaking. Due to the suppressed sea level during the Last Glacial Maximum, deep ocean generation of internal tides was substantially larger than the pre-industrial ([Egbert et al., 2004](#); [Wilmes and Green, 2014](#)), with possible implications for the global circulation ([Schmittner et al., 2015](#)).

Geostrophic currents interact with the ocean floor in a similar fashion as tides by generating "lee waves" ([Nikurashin and Ferrari, 2011](#); [Melet et al., 2014](#)). Lee wave generation is ultimately driven by wind forcing of the ocean circulation.

Global estimates of wind work on the ocean are of similar magnitude as the tides, i.e. 1 TW ([Wunsch, 1998](#)). Of this energy, [Nikurashin and Ferrari \(2011\)](#) found 0.2 TW to be dissipated by generating internal waves, predominantly in the Southern Ocean. Resonant near-inertial waves in the surface ocean are also formed through boundary layer motions forced by wind work on the surface ocean. The magnitude of wave energy forcing is uncertain. [Alford \(2003\)](#) found almost 0.5 TW of near-inertial wave generation. However, a large part of this energy has been observed to dissipate in the surface ocean, with only a fraction radiating into the interior as internal waves ([Crawford and Large, 1996](#)).

At the end of the life cycle of an internal wave, the energy of the wave is transformed into heat (through friction) and potential energy, as dense waters are mixed upwards in the water column. [Osborn \(1980\)](#) provided a closure to the turbulent kinetic energy equation through an approximate balance between the turbulent flux of buoyancy  $\overline{b'w'}$ , dissipation and shear production of turbulent kinetic energy (in tensor notation):

$$\overline{u'_i u'_j} \frac{\partial \overline{u}_i}{\partial x_j} = -\epsilon + \overline{b'w'} \quad (2.9)$$

where  $\epsilon$  denotes dissipation. [Osborn \(1980\)](#) defined the eddy coefficient,  $\kappa$ , such that  $\overline{b'w'} = \kappa N^2$ . The ratio of buoyancy flux to shear production is the flux Richardson number,  $R_f$ , yielding an upper bound on the diapycnal diffusivity:

$$\kappa \leq \frac{R_f}{1 - R_f} \frac{\epsilon}{N^2} = \Gamma \frac{\epsilon}{N^2}, \quad (2.10)$$

relating the dissipation of turbulent kinetic energy to the eddy diffusivity with  $\Gamma$  being the "mixing efficiency". This relationship allows for measurements of diffusivities directly in the ocean from measurements of the stratification and the dissipation, typically done with microstructure measurements. Other ways to infer the diffusivity comes from fine structure estimates, obtained from e.g. CTD and ADCP data. Within the last few decades, several data sets have been produced to map out the spatial and temporal structure of the ocean's turbulent nature. For a recent update, see [MacKinnon et al. \(2017\)](#).

### 2.2.3 Implications for the Ocean

The importance of understanding the mechanisms of mixing dates back to the early nineteenth century, with the formulation of "Sandström's theorem", stating that a fluid that is heated at the same or lower pressure than it is cooled, will not be able to do any work (dating back to the experiments described in [Sandström, 1908](#)). As the ocean is exactly such fluid (heated in the tropics and cooled at high latitudes) it is evident that the overturning circulation of the ocean is driven mechanically ([Wunsch and Ferrari, 2004](#)).

[Munk \(1966\)](#) found that observed tracer profiles in the interior Pacific could be fitted to an exponential function, constituting a balance between uniform upwelling at vertical velocity  $w$ , and downward transport of tracers, e.g. temperature,  $T$ , through turbulent diffusion:

$$\kappa \frac{d^2 T}{dz^2} = w \frac{dT}{dz}. \quad (2.11)$$

By combining fits of temperature and salinity with fits of radiocarbon ( $^{14}\text{C}$ , which has a radioactive decay term), [Munk \(1966\)](#) arrived at an estimate of the global vertical diffusivity at  $\kappa \approx 1 \text{ cm}^2\text{s}^{-1}$ , which has since become a canonical value for ocean diffusivities. It represents the required diffusivity to maintain the observed deep ocean stratification given uniform upwelling. In a stratified fluid, turbulent diffusion raises the potential energy by mixing two layers of different densities, raising the lowest, densest water and thus the center of mass of the fluid in the Earth's gravitational field ([Arneborg, 2002](#)). [Munk](#) suggested exactly the shear instabilities caused by internal waves provide the energy required for maintaining the observed stratification.

Following the ideas of [Munk \(1966\)](#), numerous attempts were made to measure the actual diffusivity, somewhat surprisingly found to have a characteristic value an order of magnitude smaller than the canonical Munk value, but with enhanced values over topography ([Polzin et al., 1997](#); [Ledwell et al., 1998](#)). While [Munk and Wunsch \(1998\)](#) stated that this discrepancy relates to the fact that the diffusivity of [Munk \(1966\)](#) should be viewed as a global or basin-averaged value, another cause for discrepancy is the assumption of uniform upwelling. Ocean upwelling is not uniform, with a large fraction of abyssal waters upwelling mechanically through Ekman divergence over the Southern Ocean, exerting a strong control of global overturning and stratification ([Toggweiler and Samuels, 1995](#); [Gnanadesikan, 1999](#)). Thus, the global overturning is driven by at least two components, and the relative strength between the two largely controls the overall strength of

the overturning (see *Kuhlbrodt et al., 2007*, for a nice review).

### 2.2.4 Modelling Vertical Mixing

While theory was expanded, and experiments were performed to understand the mechanics of mixing, the importance of vertical mixing in global ocean models was also assessed. In an early general circulation model, (GCM) *Bryan (1987)* investigated the ocean sensitivity to the vertical diffusivity and found that the watermass transport of the meridional overturning circulation was proportional to  $\kappa^{1/3}$ , an early revelation of the importance of knowing the correct value of vertical diffusivities. Despite this knowledge, many ocean models in the late 20th century employed fixed, global diffusivities, partly due to the simplicity, and partly due to the unknown spatial and temporal structure of the vertical diffusivity. Evidence for spatially and possibly temporally varying diffusivities was overwhelming by the end of the century, and model studies suggested that the circulation and thermocline structure was strongly affected by the existence of localized strong mixing regions (e.g. *Samelson, 1998*).

Based on observations in the Brazil Basin, a tidal mixing parameterization was proposed by *St. Laurent et al. (2002)*. This semi-empirical parameterization states that a fraction,  $q$ , of the energy converted from barotropic to internal tides is dissipated locally. The energy flux was based on a parameterization of internal wave drag of *Jayne and St. Laurent (2001)*, who showed that adding such term to the sink of barotropic tidal energy increased the total dissipation of the barotropic tide in the deep ocean from less than 1% to about 30%, corresponding to 1 TW (very close to the satellite based estimate of *Egbert and Ray, 2000*). The proposed parameterization by *St. Laurent et al. (2002)* is:

$$\kappa = \kappa_b + \frac{\Gamma q E_F(x, y) F(z)}{\rho N^2}. \quad (2.12)$$

The fraction,  $q$ , of the local conversion of energy from barotropic to internal tides,  $E_F(x, y)$ , is assumed to dissipate locally following an imposed exponential function in the vertical

$$F(z) = \frac{e^{-(H+z)/\zeta}}{\zeta(1 - e^{-H/\zeta})}, \quad (2.13)$$

where  $\zeta = 500\text{m}$  is a scale height. The rest of the energy is assumed to propagate and dissipate away from the generation site, contributing to the fixed background

diffusivity,  $\kappa_b$ . The *St. Laurent et al.* (2002) parameterization is closed by assuming that diffusivities can be inferred through the *Osborn* (1980) model in Eq. 2.10 using a fixed mixing efficiency,  $\Gamma$ . The diffusivities arising from the tidal mixing parameterization were in good agreement with the measurement campaigns in the Brazil Basin (*St. Laurent et al.*, 2002), and it has since been the standard parameterization for tidally induced mixing in many ocean models. The implementation of the parameterization has improved GCMs through greatly reduced tracer biases, (*Simmons et al.*, 2004) and greatly increases the abyssal cell of the overturning circulation compared to previous tidal mixing parameterizations (*Jayne*, 2009).

### Shortcomings

Despite the simplicity and success of the *St. Laurent et al.* (2002) mixing scheme, there are at least five issues with the parameterization.

First is the use of a constant background diffusivity. While the background diffusivity can be tuned to match observations of mixing (*Jochum*, 2009), it presents an infinite source of energy for mixing because diffusivities away from the bottom are independent of stratification. The issue with background diffusivities is particularly problematic for transient simulations and simulations of past or future climate where little is known of the spatial structure of diffusivities. Using a uniform background diffusivity, or maps tuned to observations, require an assumption that far-field mixing is largely independent of stratification and internal wave generation. Increased deep tidal dissipation during the last glacial maximum (LGM) has recently been demonstrated to have significant impact on the AMOC (*Schmittner et al.*, 2015; *Jansen*, 2016). It is therefore desirable to fully replace artificial mixing coefficients that are energetically inconsistent, as they might obscure the true physical response of the ocean circulation to changes in surface or deep forcing of internal waves.

A second issue arises in the factor  $q$ , the fraction of energy converted to internal waves that dissipate locally. While local estimates of  $q$  are sparse and difficult to obtain, (*Klymak et al.*, 2006; *Waterhouse et al.*, 2014), there is little evidence supporting the notion of a fixed value of  $q$  in space and time (*Lefaube et al.*, 2015; *MacKinnon et al.*, 2017). Thus, to fully capture the ocean mixing, using the existing tidal mixing parameterization requires a parameterization of  $q$ .

This argument also applies to the vertical distribution function,  $F(z)$ , which is an exponential decay function using a fixed scale height, set to  $\zeta = 500\text{m}$

(*St. Laurent et al.*, 2001). While empirically based, the choice represents an ad hoc assumption of how internal wave energy is dissipated locally. The constant choice of a fixed scale height in time and space, and the assumption that dissipation follows an exponential decay away from the bottom, remains dubious (*Lefaive et al.*, 2015; *Kunze*, 2017). A recent study found a crucial dependence of model behavior to the vertical distribution of dissipation (*Peltier and Vettoretti*, 2014). When using the *St. Laurent et al.* (2002) parameterization in model simulation using glacial boundary conditions they showed that the simulated climate over the North Atlantic went from oscillatory to stable. While more research is needed to understand the reason for and impact of this result, it illustrates how important a simple assumption to a parameterization can be.

A further shortcoming of the semi-empirical mixing parameterization is the concept of mixing efficiencies,  $\Gamma$ . Most models employ constant mixing efficiencies of  $\Gamma = 0.2$  in the model parameterizations of vertical mixing, although spatial heterogeneity has been observed, with values ranging mostly between 0.1-0.3 (*Gregg et al.*, 2018). Despite the small variations, the value of  $\Gamma$ , and its ability to vary depending on the ocean flow, could lead to important feedbacks in the ocean circulation (*de Lavergne et al.*, 2016).

Finally, the *St. Laurent et al.* (2002) parameterization is only valid for tidal mixing. Any other source of internal wave energy (near-inertial waves, lee waves, eddies) requires separate treatment and parameterization (*Nikurashin and Ferrari*, 2011; *Jochum et al.*, 2013). Furthermore, the specification of tidal energy flux (or any topographically induced energy flux) requires a map of the energy flux given the bathymetry, sea level and bottom stratification. As a result, for simulations of paleoclimate run for several thousand years, knowledge is needed of how the energy fluxes both at the surface and the bottom of the ocean varies (e.g. *Wilmes and Green*, 2014).

While these shortcomings have been listed, it is also important to note that recent advances in modeling has had increased attention towards several of the above listed shortcomings. As a result, recent formulations for the vertical distribution of dissipation have been proposed and implemented in GCMs, demonstrating an important impact on stratification as well as overturning rates (*Polzin*, 2009; *Melet et al.*, 2013). Similarly, parameterizations of mixing efficiencies have been proposed and tested. Some of these remain ad hoc (*Melet et al.*, 2013), others find more physical basis (*de Lavergne et al.*, 2016). Furthermore, parameterizations similar to that of *St. Laurent et al.* (2002) have been developed for NIWs (*Jochum et al.*,

2013) as well as lee waves (*Nikurashin and Ferrari, 2011; Melet et al., 2014*). However, introducing more parameterizations do not remove the fact that a constant background diffusivity remains present in many ocean models, which is energetically inconsistent, and therefore it is interesting to investigate completely different parameterizations for diapycnal mixing and their impact on ocean circulation and climate.

## 2.3 IDEMIX

An alternative to treating the mixing from breaking internal waves separated into waves originating from different forcing mechanisms (tides, lee waves and near-inertial waves), is estimating vertical diffusivities by solving the internal wave energy balance in physical and wavenumber space. However, tracking the propagation of energy in both physical and wavenumber space is a 6-dimensional problem which requires significant computational power to overcome, in particular in the case of global ocean models (see e.g. *Müller and Briscoe, 1999; Müller and Natararov, 2003*).

The 6-dimensional problem can be simplified by integrating the internal wave energy over all wavenumbers. Such simplification reduces the dimensionality to the familiar 3 spatial dimensions. This is the basic concept of the model IDEMIX (Internal wave Dissipation, Energy and MIXing *Olbers and Eden, 2013*). This section describes the derivation of the first version, introduced in *Olbers and Eden (2013)* and used throughout this thesis. The derivation is explained in some detail here, as IDEMIX forms a fundamental part of the remaining chapters. For more in-depth discussions we refer to *Olbers and Eden (2013)*.

The starting point is the internal wave energy spectrum  $\mathcal{E}(\vec{x}, \vec{k}, t)$ . For waves propagating through a slowly varying background field, Wentzel-Kramers-Brillouin (WKB) theory states that wave action,  $\mathcal{A} = \mathcal{E}/\omega$ , is conserved, and the radiative transfer for the wave action spectrum can thus be formulated:

$$\frac{\partial \mathcal{A}}{\partial t} + \vec{\nabla} \cdot \left( \vec{\nabla}_{\vec{k}}(\omega) \mathcal{A} \right) + \vec{\nabla}_{\vec{k}} \cdot \left( -\vec{\nabla}(\omega) \mathcal{A} \right) = \mathcal{S}, \quad (2.14)$$

where  $\vec{\nabla}_{\vec{k}}(\omega)$  is the group velocity and  $-\vec{\nabla}(\omega)$  is the wave refraction. In this notation,  $\vec{\nabla}_{\vec{k}} = (\partial/\partial k, \partial/\partial l, \partial/\partial m)$  and  $\vec{\nabla} = (\partial/\partial x, \partial/\partial y, \partial/\partial z)$ . The frequency,  $\omega$ , is a function

$$\omega = \Omega(\vec{x}, \vec{k}, t). \quad (2.15)$$

The right hand side of Eq. 2.14 is the sum of source terms of wave action. *Olbers and Eden (2013)* split this into three distinct terms:

$$\mathcal{S} = \mathcal{S}_{\text{gen}} + \mathcal{S}_{\text{ww}} + \mathcal{S}_{\text{diss}} \quad (2.16)$$

denoting generation from external forcing, wave-wave interactions and dissipation, respectively.

In order to proceed with the simplification of the 6-dimensional problem, Eq. 2.14 is multiplied with the frequency,  $\omega$ , giving

$$\omega \frac{\partial \mathcal{A}}{\partial t} + \omega \vec{\nabla} \cdot \left( \vec{\nabla}_{\vec{k}}(\omega) \mathcal{A} \right) + \omega \vec{\nabla}_{\vec{k}} \cdot \left( -\vec{\nabla}(\omega) \mathcal{A} \right) = \omega \mathcal{S}, \quad (2.17)$$

or in terms of the energy spectrum

$$\frac{\partial \mathcal{E}}{\partial t} + \nabla \cdot \left( \nabla_{\vec{k}}(\omega) \mathcal{E} \right) - \nabla_{\vec{k}} \cdot \left( \nabla(\omega) \mathcal{E} \right) = \omega \mathcal{S}, \quad (2.18)$$

where the term  $\mathcal{E}/\omega \partial \omega / \partial t$  has been ignored. Defining the total internal wave energy

$$E = \int \int \int d^2 k dm \mathcal{E}(\vec{k}, \vec{x}, t), \quad (2.19)$$

the integral over Eq. 2.18 is separated into the integral over upward propagating waves (negative vertical wavenumber  $m$ )

$$E^+ = \int_{-\infty}^0 dm \int d^2 k \mathcal{E}(\vec{k}, \vec{x}, t), \quad (2.20)$$

and downward propagating waves (positive  $m$ ):

$$E^- = \int_0^{\infty} dm \int d^2 k \mathcal{E}(\vec{k}, \vec{x}, t). \quad (2.21)$$

The total energy is

$$E = E^+ + E^-. \quad (2.22)$$

Similarly, the energy difference between upward and downward propagating waves,  $\Delta E$ , can be expressed as an asymmetric energy equation:

$$\Delta E = E^+ - E^-. \quad (2.23)$$

Due to energy conservation, the refractive terms cancel out in Eq. 2.22, but remain

in the asymmetric equation (Eq. 2.23). The integration of horizontal derivatives in the second term in Eq. 2.18 can be ignored if one assumes lateral homogeneity. If not, these terms represent the lateral propagation of energy in the case of lateral anisotropy. *Olbers and Eden (2013)* parameterize the horizontal fluxes of energy arising from horizontal anisotropy by expanding the energy spectrum in a Fourier series and truncating at first order, which gives rise to two horizontally propagating energy compartments (see their Appendix A). Thus, the integral over all wavenumbers yields the equation for total wave energy:

$$\frac{\partial E}{\partial t} + \frac{\partial}{\partial z} (J^+ + J^-) + \frac{\partial}{\partial x} (v_c E_c) + \frac{\partial}{\partial y} (v_s E_s) = \int_{-\infty}^{\infty} dm \int d^2 k \omega \mathcal{S}_{\text{diss}} = -\epsilon_{IW}, \quad (2.24)$$

where the integral over  $\mathcal{S}_{\text{ww}}$  cancels out as it conserves energy.  $E_c$  and  $E_s$  are the energy compartments related to the anisotropy of the energy density, propagating at mean velocities  $v_c$  and  $v_s$ , respectively. The vertical fluxes of energy,  $J^+$  and  $J^-$ , are given as

$$J^+ = \int_{-\infty}^0 dm \int d^2 k c \mathcal{E} \quad (2.25)$$

$$J^- = - \int_0^{\infty} dm \int d^2 k c \mathcal{E}, \quad (2.26)$$

where  $c$  is the vertical group velocity given by  $\partial\omega/\partial m$  using the dispersion relation Eq. 2.7.

Assuming vertical symmetry in the horizontal anisotropy terms, the equation for vertical asymmetry becomes

$$\frac{\partial \Delta E}{\partial t} + \frac{\partial}{\partial z} (J^+ - J^-) = \int_{-\infty}^0 dm \int d^2 k \omega (\mathcal{S}_{\text{ww}} + \mathcal{S}_{\text{diss}}) - \int_0^{\infty} dm \int d^2 k \omega (\mathcal{S}_{\text{ww}} + \mathcal{S}_{\text{diss}}). \quad (2.27)$$

By assuming that the dissipation is vertically symmetric, the integrals over  $\mathcal{S}_{\text{diss}}$  can be ignored in Eq. 2.27. From Eq. 2.22 and 2.23

$$E^+ = \frac{1}{2} (E + \Delta E) \quad (2.28)$$

and

$$E^- = \frac{1}{2} (E - \Delta E). \quad (2.29)$$

By parameterizing the fluxes in Eq. 2.26 such that

$$J^+ = c_0^+ E^+ \quad (2.30)$$

and

$$J^- = -c_0^- E^- \quad (2.31)$$

and assuming that  $c_0^+ \simeq c_0^- = c_0$  one finds that

$$J^+ + J^- = c_0 \Delta E \quad (2.32)$$

$$J^+ - J^- = c_0 E. \quad (2.33)$$

From the definition of  $c_0^+$  it follows that

$$c_0^+ = \frac{1}{E^+} \int_{-\infty}^0 dm \int d^2 k c \mathcal{E}, \quad (2.34)$$

and similarly for  $c_0^-$ .

In order to solve the effect of the integral over  $\mathcal{S}_{\text{ww}}$  on the right hand side of Eq. 2.27, it is now assumed that this term works as to relax the internal wave energy to a state of no vertical asymmetry, given a relaxation time,  $\tau_v$ . That is,

$$\frac{\partial \Delta E}{\partial t} + \frac{\partial}{\partial z} (J^+ - J^-) = \frac{\partial \Delta E}{\partial t} + \frac{\partial}{\partial z} c_0 E = -\Delta E / \tau_v. \quad (2.35)$$

In the diffusive limit, (timescales longer than  $\tau_v$ ), the equation reduces to

$$\frac{\partial}{\partial z} c_0 E = -\Delta E / \tau_v. \quad (2.36)$$

A similar relaxation is assumed for horizontal anisotropies but with a different timescale,  $\tau_h$ . Inserting these parameterizations in Eq. 2.24, and making the assumption that  $v_c \simeq v_s = 2v_0$  [Olbers and Eden \(2013\)](#) arrived at

$$\frac{\partial E}{\partial t} - \frac{\partial}{\partial z} \left( c_0 \tau_v \frac{\partial (c_0 E)}{\partial z} \right) + \nabla_h \cdot (v_0 \tau_h \nabla_h (v_0 E)) = -\epsilon_{IW}. \quad (2.37)$$

The value for  $c_0$  is found through eq. 2.34 by assuming a GM spectrum in the shape ([Cairns and Williams, 1976](#)):

$$\mathcal{E} = E(z) A(k, \omega) B(\omega) \quad (2.38)$$

and results in the simple approximation for  $c_0$ :

$$c_0 = c_\star \gamma \mathcal{G}(N/|f|), \quad (2.39)$$

where  $\gamma = 1.57$  comes from the integral over the wavenumber part of  $A(k, \omega)$  (*Cairns and Williams, 1976*), and  $\mathcal{G}(x)$  is an approximation to the integral over  $\omega$  (see appendix A of *Olbers and Eden, 2013*):

$$\mathcal{G}(x) \simeq \frac{9}{10} x^{-2/3} (1 - e^{-x/4.3}) \frac{2/\pi}{1 - (2/\pi) \arcsin x^{-1}} \quad (2.40)$$

and  $c_\star$  is a function of the modal bandwidth,  $j_\star$ , and the stratification:

$$c_\star = \frac{1}{j_\star \pi} \int_{-h}^0 N dz. \quad (2.41)$$

The horizontal velocity,  $v_0$ , is found in a similar fashion where

$$v_0 = c_\star \gamma \mathcal{H}(N/|f|), \quad (2.42)$$

where

$$\mathcal{H}(x) = \frac{2/\pi}{1 - (2/\pi) \arcsin x^{-1}} \frac{x - 1}{x + 1}. \quad (2.43)$$

The closure for the dissipation of energy (the right hand side of Eq. 2.37) used in *Olbers and Eden (2013)* is the analytically calculated transfer across a vertical wavenumber cutoff derived by *McComas and Müller (1981a)* for the different mechanisms elastic scattering, induced diffusion and parametric subharmonic instabilities (PSI). *McComas and Müller (1981a,b)* found induced diffusion and PSI to dominate the energy transfer at high vertical wavenumber to be approximated by

$$\epsilon_{IW} \propto \mu \frac{|f| m_\star^2}{N^2} E^2. \quad (2.44)$$

Here,  $m_\star = N/c_\star$  is the bandwidth of the GM spectrum in vertical wavenumber space.

An issue with the parameterization in Eq. 2.44 is that dissipation vanishes rapidly as  $|f| \rightarrow 0$ . To accommodate this, *Olbers and Eden (2013)* used results from *Heyney et al. (1986)* who found that dissipation scales with a factor of  $\operatorname{arccosh}(N/|f|)$ , which acts to moderate the decrease in dissipation approaching Equator. *Olbers and Eden (2013)* combine the two estimates into the parameteri-

zation

$$\epsilon_{IW} = \mu |f| \frac{\operatorname{arccosh}(N/|f|) m_*^2 E^2}{\operatorname{arccosh}(N_0/f_0) N^2} = \mu_0 f_e \frac{m_*^2 E^2}{N^2}, \quad (2.45)$$

where  $\mu_0 = \mu \operatorname{arccosh}(N_0/f_0) \simeq \mu/3$  assuming  $N_0/f_0 \simeq 10$ . The effective coriolis parameter,  $f_e$ , is given as  $f_e = |f| \operatorname{arccosh}(N/|f|)$ . The choice of vertical profile for the dissipation rates are important for the ocean circulation, ventilation and thermocline structure in general circulation models (*Melet et al., 2016*). The choice of dissipation profile in IDEMIX contrasts that presented in the parameterization by *St. Laurent et al. (2002)* (Eq. 2.12), which assumes an exponential decay function of dissipation independent of  $N^2$ .

Coupling IDEMIX to the prognostic equations in an ocean model occurs through the dissipation term,  $\epsilon_{IW}$ . *Olbers and Eden (2013)* use the *Osborn (1980)* model (Eq. 2.10) assuming that  $\epsilon_{IW}$  corresponds to the shear production term. Assuming a linear relationship between buoyancy production and turbulent dissipation, that is,  $b'w' = \kappa N^2 = \delta \epsilon$  results in an equation for the vertical diffusivity:

$$\kappa = \frac{\delta}{1 + \delta} \frac{\epsilon_{IW}}{N^2}. \quad (2.46)$$

### 2.3.1 Parameter Choice

The derivation presented above requires closure of a set of parameters. These are  $\mu$ ,  $j_*$ ,  $\tau_v$  and  $\tau_h$ .

Throughout the present work, the parameter choice suggested by *Olbers and Eden (2013)* is used. That means a use of  $\mu = 4$ ,  $j_* = 10$ ,  $\tau_v = 1$  day,  $\tau_h = 10$  days.

Choosing  $\mu = 4$  likely results in an overestimation of dissipation (e.g. *Gregg, 1989; Polzin et al., 1995*). From *McComas and Müller (1981a,b)* this corresponds to roughly double the energy transported across the high wavenumber cut-off from ID and PSI. Nevertheless, for this thesis this choice suffices, as it is within observational uncertainties (*Pollmann et al., 2017*). The modal bandwidth of the GM spectrum,  $j_*$ , has been estimated to range from anywhere between 1-20 (*Polzin and Lvov, 2011*). The choice of *Olbers and Eden (2013)* is in the center of this range.  $\tau_v = 1$  day is based on the assumption that waves only reflect few times at surface and bottom before homogenization is obtained. The value of  $\tau_h$  is based on the estimate of  $\tau_v$  and the assumption that the horizontal group speed is one order of magnitude larger than the vertical group speed, yielding  $\tau_h = 10$  days (*Olbers and Eden, 2013*).

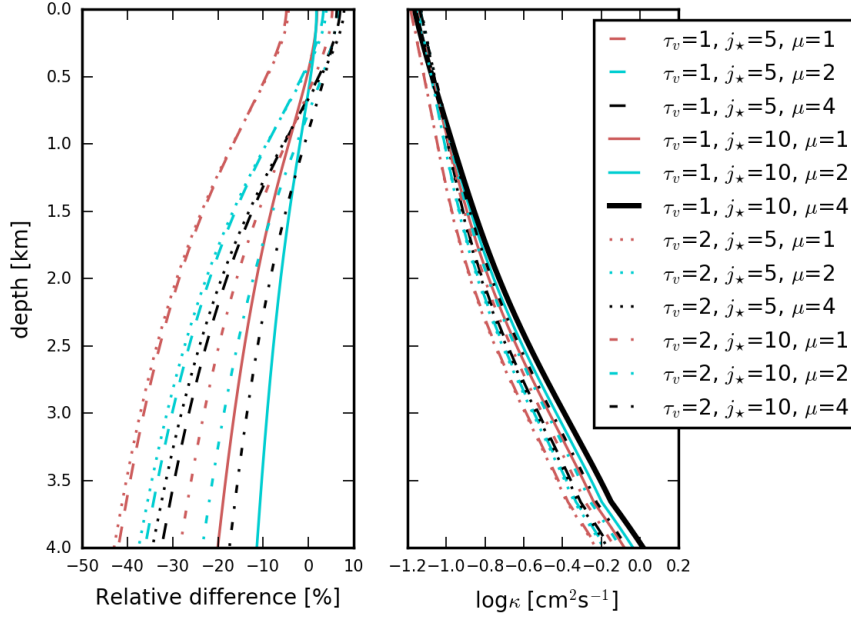


**Figure 2.2:** Left: Relative difference to the parameter choice of *Olbers and Eden (2013)* using different values of  $\mu$ ,  $j_*$ ,  $\tau_v$  and  $\tau_h$ . Right: Vertical profile of the diffusivity obtained using the different parameter values. The choice of *Olbers and Eden (2013)*, which is employed throughout the work presented here, is highlighted as the thick black curve.

*Pollmann et al. (2017)* compare an implementation of IDEMIX in an ocean model with fine-structure estimates from ARGO floats and found an optimal choice of parameters somewhat different than used here, namely  $j_* = 5$ ,  $\tau_v = 2$  days and  $\mu = 1$ . However, they also argued that due to uncertainties in the fine-structure estimates, any choice of parameters within the realistic span of parameter space compares well with fine-structure data.

Here, a simple test of the importance of the choice of parameters is performed using a column model of IDEMIX, as in *Olbers and Eden (2013)* using a fixed stratification  $N = N_0 \exp(z/b)$  with  $N_0 = 0.005 \text{ s}^{-1}$  and  $b = 1300\text{m}$  with no surface forcing and bottom forcing  $F_{bot} = 1\text{cm}^3\text{s}^{-3}$ . A series of parameter perturbations are run. The profiles of  $\kappa$  are seen in the right panel of Fig. 2.2, the relative difference to the parameter choice used here are shown in the left panel.

As can be seen in Fig. 2.2, the relative difference in vertical diffusivity obtained from the parameter sweep in the column model reaches a maximum less than a factor of two in regions of weak stratification. The structure of the diffusivity profile (right panel) is qualitatively comparable for all parameter sets. Greatest sensitivities are seen in  $j_*$  and  $\mu$ . This is not unexpected, since dissipation depends

linearly on  $\mu$ , and  $j_*$  in quadrature. On the other hand, doubling  $\tau_v$  changes the diffusivity profile only marginally (compare e.g. dotted and dashed lines of same color). While a factor of 2 is fairly small compared to the uncertainty in fine-structure estimates, the parameter uncertainty yields a difference in diffusivity comparable to a doubling of the stratification (as discussed later in Chapter 6). Thus, future work should continue the line of *Pollmann et al. (2017)* in order to estimate the best parameter choice for IDEMIX in climate models, and what impact it has on solutions of the global ocean circulation.

In general, the choice of parameters of *Olbers and Eden (2013)* that is used here likely sets an upper bound on the diffusivity profile. It should be noted that it is not evident that any of the parameters should in fact be constants, but should be parameterized as well.

### 2.3.2 Discussion

In the end, replacing one mixing parameterization with another will not necessarily improve the model. Rather, replacing one mixing scheme with another removes one set of assumptions and introduces a new. Making a final decision as to which parameterization is preferable over the other requires several studies. Evaluation can then be based on how the different parameterizations perform in simulating contemporary climate, how reasonable the underlying assumptions are, which parameterization is the most computationally efficient, and if one parameterization allows feedbacks that are important to the climate system. As a result, when implementing IDEMIX in a global climate model one could focus on several aspects. Parameters can be tuned to fit the best climate variables of pre-industrial climate such as SST, precipitation, thermocline structure, climate variability or any other variable. The end result could be a similar study as that of *Pollmann et al. (2017)*, but instead of tuning model parameters to observed mixing rates, they are tuned for optimization of simulations of contemporary climate.

Contrary to such study, the work presented in this thesis has focused on unlocking potential physics that are masked in climate models employing mixing schemes that depend on a relatively large constant background mixing coefficient. While some preliminary simulations were carried out using different parameter choices, the qualitative differences between simulations were minor and will not be discussed further. A full exploration of the parameter space and its impact ocean circulation is beyond the scope of this thesis. Thus, focus will be on perturbing the

climate system with drastic changes that potentially change the stratification, and conversely the vertical mixing, and from this identify if climate system feedbacks occur that have implications for climate change, past or future.

## 2.4 Marine Carbon Cycle

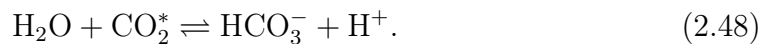
CO<sub>2</sub> is a greenhouse gas that absorbs Earth's outgoing infrared radiation and emits it back to the surface of the planet, thus increasing the global surface temperature. The ocean plays a key role in the global carbon cycle, not only because the oceans covers the majority of Earth's surface area, but because it stores roughly 60 times the amount of carbon stored in the atmosphere (*Broecker, 1982*). Therefore, the observed changes in atmospheric pCO<sub>2</sub> on glacial timescales observed in ice cores is in part caused by changes in the ocean chemistry (*Sigman and Boyle, 2000; Kohfeld and Ridgwell, 2009*). Some space shall therefore be dedicated to briefly review key concepts of ocean biogeochemistry that are important for the remaining chapters. The carbon cycle, including the marine biogeochemistry, is an extensive topic that cannot be covered in few pages. For a more thorough introduction and discussion the reader is referred to textbooks such as *Sarmiento and Gruber (2006); Williams and Follows (2011)*.

### 2.4.1 Surface Ocean Chemistry and Gas Transfer

Carbon dioxide, CO<sub>2</sub><sup>gas</sup>, dissolves in water in aqueous form, CO<sub>2</sub><sup>aq</sup>, which in turn reacts with water to form carbonic acid, H<sub>2</sub>CO<sub>3</sub><sup>aq</sup>. In most textbooks, e.g. *Williams and Follows (2011)*, and for the rest of this chapter, CO<sub>2</sub><sup>aq</sup> and H<sub>2</sub>CO<sub>3</sub><sup>aq</sup> is combined into a single, hypothetical, species, dissolved CO<sub>2</sub>, which is often written as CO<sub>2</sub><sup>\*,aq</sup>. The chemical reaction can then be written as



where the double arrow indicates that the reaction occurs in both directions. For the remainder of reactions the phase of the reactant will be omitted, as all are aqueous, with the exception for H<sub>2</sub>O, which is liquid. CO<sub>2</sub><sup>\*</sup> reacts with water to form bicarbonate (see *Dickson et al., 2007*):



Bicarbonate in turn forms carbonate:



The concentration of dissolved  $\text{CO}_2$ , bicarbonate and carbonate ions, is commonly added and referred to as dissolved inorganic carbon (DIC):

$$\text{DIC} = [\text{CO}_2^*] + [\text{HCO}_3^-] + [\text{CO}_3^{2-}]. \quad (2.50)$$

The reaction 2.48 can be used to identify the rate of change in  $[\text{CO}_2^*]$ :

$$\frac{d[\text{CO}_2^*]}{dt} = -K_{\text{Forward}}[\text{CO}_2^*] + K_{\text{Backward}}[\text{HCO}_3^-][\text{H}^+], \quad (2.51)$$

where  $K_{\text{Forward}}$  and  $K_{\text{Backward}}$  are the reaction rates from left to right and right to left in 2.48, respectively. At equilibrium, where the l.h.s. is zero, the equilibrium coefficient,  $K_1$ , can be defined as

$$K_1 = \frac{[\text{HCO}_3^-][\text{H}^+]}{[\text{CO}_2^*]} \Leftrightarrow [\text{HCO}_3^-] = K_1 \frac{[\text{CO}_2^*]}{[\text{H}^+]}. \quad (2.52)$$

Similarly for reaction 2.49,

$$K_2 = \frac{[\text{CO}_3^{2-}][\text{H}^+]}{[\text{HCO}_3^-]} \Leftrightarrow [\text{CO}_3^{2-}] = K_1 K_2 \frac{[\text{CO}_2^*]}{[\text{H}^+]^2}. \quad (2.53)$$

From these relations, surface ocean concentrations of dissolved  $\text{CO}_2$  can be described solely in terms of the concentrations of DIC and  $\text{H}^+$  by inserting Eqs. 2.52 and 2.53 in Eq. 2.50:

$$[\text{CO}_2^*] = \text{DIC} \left( 1 + \frac{K_1}{[\text{H}^+]} + \frac{K_1 K_2}{[\text{H}^+]^2} \right)^{-1}. \quad (2.54)$$

Knowing the  $[\text{CO}_2^*]$  for the surface waters is needed to estimate the transfer of gas, the flux,  $J$ , across the air-sea interface:

$$J = k_g ([\text{CO}_2^*] - [\text{CO}_2^{\text{sat}}]), \quad (2.55)$$

where  $k_g$  is the gas transfer coefficient and  $[\text{CO}_2^{\text{sat}}]$  is the concentration in the atmosphere that the ocean would obtain if it were in equilibrium with the atmosphere. It is through the surface ocean only that the ocean and atmosphere exchanges  $\text{CO}_2$ , and thus it is the properties of the surface ocean that determine if the ocean outgasses or uptakes carbon. Eq. 2.55 shows that there are three parameters that dictate the ocean outgassing or uptake: The concentrations of  $\text{CO}_2^*$ ,  $\text{CO}_2^{\text{sat}}$  and

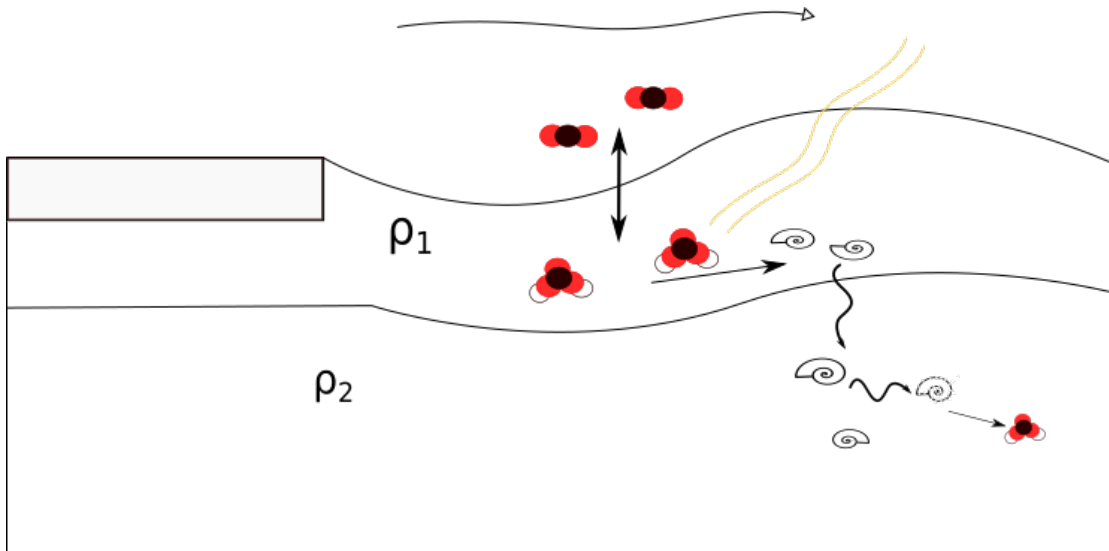


**Figure 2.3:** A simplified schematic of surface carbon chemistry processes.  $\text{CO}_2$  is exchanged with the atmosphere as a function of  $\text{CO}_2$  concentrations in ocean and atmosphere, wind stress and sea ice cover. Organic matter and carbonate shells are formed in the surface ocean. A fraction of these particles sink to the deep ocean and are dissolved, increasing deep ocean DIC.

the gas transfer coefficient. The first is, as seen in Eq. 2.54, a function of the DIC concentration. The gas transfer coefficient is a function of sea ice cover, wind stress and temperature (see Fig. 2.3). The surface ocean experiences high lateral heterogeneity in DIC concentrations (*Takahashi et al., 2009*). The ocean releases carbon in upwelling regions such as the Southern Ocean and the tropics, where old, carbon rich waters are ventilated, whereas surface waters experiencing cooling and biological production, such as western boundary currents, uptake carbon from the atmosphere.

### 2.4.2 Changes in Ocean DIC

Once a water parcel has left the surface mixed layer, the DIC it holds is shielded from the atmosphere until the parcel again is brought to the surface, through adiabatic or diabatic pathways. The DIC concentration of a water parcel below the euphotic layer is continuously increased as small particles of organic matter and  $\text{CaCO}_3$  sink into the parcel and are respired (Fig. 2.3). Carbon is removed from the deep ocean through sedimentation, and in the euphotic zone through formation of organic matter and  $\text{CaCO}_3$ . As a consequence, the ocean DIC storage can be changed both at the surface and in the deep, and depending on the process that increases or decreases the carbon content of the ocean, the carbon storage can

be separated into different pumps (*Volk and Hoffert, 1985*). Four carbon pumps are generally considered: the solubility pump, identifying that colder waters can hold more DIC, the organic (soft tissue) pump, related to the formation of organic matter through photosynthesis in the surface waters and the dissolution of organic matter in the deep ocean through respiration, the carbonate (hard tissue) pump, describing the formation of  $\text{CaCO}_3$  in the surface and dissolution at depth, and finally the disequilibrium pump, which quantifies the impact of finite gas transfer at the surface, modifying how much carbon is dissolved or released from the water parcel before it is transported from the surface ocean to the interior.

The ocean's ability to store more or less carbon is often quantified by looking at the changes in carbon inventory separated into the different pumps. From a model perspective, the choice of quantification depends on available model variables. If a model does not explicitly trace preformed nutrients, DIC and alkalinity, estimates using so called back-calculations must be made. While it is increasingly popular to directly trace preformed variables, these are not implemented in the model used throughout this study, and therefore the carbon pumps are quantified using back-calculations, despite their shortcomings (see e.g. *Ito et al., 2004*; *Ito and Follows, 2005*; *Lauderdale et al., 2013*; *Bernadello et al., 2014*). The following sections describe the quantification used throughout this thesis.

### Organic Pump

Recent studies have found that the organic pump is most accurately described in terms of the ratio of remineralized to preformed nutrients, such as phosphate ( $\text{PO}_4^{3-}$ , *Ito and Follows, 2005*; *Marinov et al., 2008*). Thus, the efficiency of the organic pump depends on the level of nutrient utilization,  $\mathcal{P}^*$ :

$$\mathcal{P}^* = \frac{\text{PO}_4^{3-,\text{rem}}}{\text{PO}_4^{3-}} = \frac{\text{PO}_4^{3-,\text{rem}}}{\text{PO}_4^{3-,\text{rem}} + \text{PO}_4^{3-,\text{pre}}}, \quad (2.56)$$

where  $\text{PO}_4^{3-,\text{rem}}$  and  $\text{PO}_4^{3-,\text{pre}}$  denote remineralized and preformed phosphate, respectively, and the sum of the two yields the total phosphate.  $\text{PO}_4^{3-,\text{pre}}$  is the concentration of dissolved phosphate of the water parcel at the time it was transported to the interior ocean.  $\text{PO}_4^{3-,\text{rem}}$  is the concentration of phosphate added to the water parcel through respiration of organic matter. If all the phosphate in the ocean is remineralized, it means that all nutrients were utilized at the time of subduction to the interior, and  $\mathcal{P}^*$  equals 1. If all nutrients were dissolved at the

time of subduction,  $\mathcal{P}^*$  equals 0 and there is a complete shutdown of biological activity.

The notion of tracing preformed nutrients is not common in all models and as such, the fraction of remineralized nutrients need to be quantified in terms of other model variables. By assuming a constant stoichiometric ratio for phosphor and oxygen,  $r_{\text{O:P}} = -170$  (that is, it takes 170 moles of oxygen to respire 1 mole of phosphate), the oxygen utilization can be used locally to estimate the fraction of remineralized nutrients (*Ito and Follows, 2005*):

$$\text{PO}_4^{3-,\text{rem}} = \frac{\text{O}_2 - \text{O}_2^{\text{sat}}(T, S)}{r_{\text{O:P}}} = -\frac{\text{AOU}}{r_{\text{O:P}}}, \quad (2.57)$$

where  $\text{AOU}$  is the apparent oxygen utilization, the difference between the saturated  $\text{O}_2$  concentration at the time of subduction, a function of temperature and salinity, and the  $\text{O}_2$  concentration. A caveat with Eq. 2.57 is that it assumes saturated oxygen concentrations at the time of subduction, an assumption that overestimates the oxygen level of subducting water parcels at high latitudes (*Ito et al., 2004*).

The respired carbon that is added to the water parcel,  $C_{\text{soft}}$ , can be calculated from the remineralized nutrients

$$C_{\text{soft}} = r_{\text{C:P}} \text{PO}_4^{3-,\text{rem}}, \quad (2.58)$$

where  $r_{\text{C:P}} = 117$  (*Anderson and Sarmiento, 1994*).

Because nutrient utilization is generally larger in the North Atlantic than the Southern Ocean, the idea has been proposed that the strength of the organic pump is largely determined by the fractional relationship between deep waters ventilated in the North Atlantic and the Southern Ocean (*Toggweiler et al., 2003a; Marinov et al., 2008; Schmittner and Galbraith, 2008*).

### Carbonate Pump

Formation or dissolution of calcite and aragonite removes or adds  $\text{Ca}^{2+}$  and  $\text{CO}_3^{2-}$  to the ocean water:



Removal of  $\text{Ca}^{2+}$  reduces ocean alkalinity,  $\text{Alk}$ , a measure of ocean charge balance, by a ratio of 2:1 to DIC. Thus, the carbonate pump can be quantified in terms of

the change in alkalinity:

$$C_{\text{carb}} = \frac{1}{2} (\text{Alk}_{\text{rem}} - r_{\text{N:O}} \text{AOU}), \quad (2.60)$$

where  $\text{Alk}_{\text{rem}}$  is the remineralized alkalinity from dissolution of  $\text{CaCO}_3$  and the second term on the rhs is the increase in alkalinity from dissolution of organic matter. The remineralized alkalinity is the difference between total alkalinity and preformed alkalinity. If the latter is not explicitly traced in the model, it has to be estimated. *Gruber et al. (1996)* used a linear regression model with  $S$  and the conservative tracer  $PO = \text{O}_2 - r_{\text{O}_2:\text{P}}$  (*Broecker, 1974*):

$$\text{Alk}_{\text{pre}} = (367.5 + 54.9 \text{psu}^{-1} S + 0.074 \text{kg} \mu\text{mol}^{-1} PO) \mu\text{eq kg}^{-1}. \quad (2.61)$$

Eq. 2.61 is an approximation and underestimates the preformed alkalinity in high alkalinity waters (*Gruber et al., 1996*). Eq. 2.61 can be input in Eq. 2.60 to yield a solution for the carbonate pump given alkalinity, nutrients, salinity and oxygen:

$$C_{\text{carb}} = \frac{1}{2} (\text{Alk} - \text{Alk}_{\text{pre}} - r_{\text{N:O}} \text{AOU}). \quad (2.62)$$

### Solubility and Disequilibrium Pump

Solubility of carbon dioxide in sea water is a function of temperature and salinity (*Weiss, 1974*). It decreases with temperature, and thus a colder ocean can hold more carbon. Reduced surface temperatures during glacial compared to interglacial climates could account for 20-30 ppmv (*Kohfeld and Ridgwell, 2009*), highlighting the potential importance of the solubility pump in altering ocean chemistry on millennial and glacial timescales. Due to the direct relationship between the ocean heat storage and the vertical mixing in ocean models, increasing the vertical mixing in a model potentially reduces the carbon content by reducing the solubility (in the absence of other mechanisms modifying the marine biogeochemistry, e.g. *Ito and Follows, 2003*; *Marinov and Gnanadesikan, 2011*).

The strength of the solubility pump is often calculated from the saturation concentration of carbon dioxide in the surface water, but given the finite gas transfer between atmosphere and ocean, surface water parcels need to reside for long periods before reaching equilibrium with the overlying atmosphere. This causes a disequilibrium effect with large potential of regulating the efficiency of the solubility pump (*Toggweiler et al., 2003b*). The 'disequilibrium pump' could both

increase and decrease the strength of the solubility pump, depending on the over- or undersaturation of carbon dioxide in a given water parcel. For supersaturated waters, the disequilibrium pump can be viewed as a strengthening of the organic and carbonate pumps (*Ito and Follows, 2013*). Other studies view the disequilibrium as a separate mechanism by which the ocean stores carbon, which results in a negative correlation between the organic and disequilibrium pumps (*Eggleston and Galbraith, 2018*). The disequilibrium pump has strongest impact on regions where surface waters have low residence time, and in regions of large sea ice cover where ocean-atmosphere interactions are inhibited (*Ödalen et al., 2018; Ferreira et al., 2018*).

Because the model used in this thesis does not track the effect of disequilibrium, the solubility and disequilibrium will in the rest of this work be treated together, referred to as "preformed carbon",  $C_{\text{pre}}$ , and will be calculated as the difference between total DIC concentrations and the sum of organic and carbonate pumps.

### 2.4.3 Modelling the Marine Carbon Cycle

The carbon cycle, through its connection to biogeochemical processes as well as feedbacks on the climate system, is difficult to account for fully in a global model. As a result, some of the large uncertainties in climate prediction lies in the response of particularly the marine ecosystem. While early attempts at simulating the carbon cycle were made using simple box models dominated by the physical and biological carbon storage (such as the canonical 3-box models by *Knox and McElroy, 1984; Sarmiento and Toggweiler, 1984; Siegenthaler and Wenk, 1984*), advances have been made over the past decades, from multi-box models (*Toggweiler, 1999*) to three-dimensional models of the marine biogeochemistry. A modern approach is models with four interacting variables: nutrients, phytoplankton, zooplankton and detritus, also referred to as NPZD models (*Fasham et al., 1990; Moore et al., 2004; Schmittner, 2005*). Such upper ocean marine ecosystem models are then coupled to the ocean circulation which transports nutrients and tracers around the ocean (*Moore et al., 2004*). Growth, loss and grazing of a number of classes of phytoplankton functional types are simulated, depending on their biogeochemical roles (*Le Quéré et al., 2005*). This allows for inclusion of different nutrients that are of variable importance to different species, such as Fe and Si. Growth is limited by nutrient and light availability as well as ocean temperature. By separating phytoplankton into groups, each group can be simulated with fixed or variable C:N:P as

well as C:Fe ratios. Thus, each group responds in different ways to alterations in nutrient or light availability. Through sinking particles carbon and nutrients can be exported from the euphotic zone and remineralize at depth, raising the deep ocean to upper ocean concentration in nutrients and DIC.

Hence, coupling the marine carbon cycle to the atmosphere through a prognostic equations of atmospheric  $p\text{CO}_2$  and carbon fluxes, the marine carbon cycle can feedback on the global climate through the radiative forcing of  $\text{CO}_2$ . This can lead to valuable knowledge of the coupled Earth system.

# Chapter 3

## Methods

### 3.1 CESM

The tool used throughout this thesis is the coarse resolution Community Earth System Model 1.2 (CESM, [Hurrell \*et al.\*, 2013](#)). Three configurations are used: A coupled ocean-sea ice model forced with atmospheric surface boundary conditions, a coupled atmosphere-ocean-land-sea ice (the same configuration as the Community Climate System Model, CCSM4) and finally a fully coupled atmosphere-ocean-land-sea ice coupled to a biogeochemistry/ecosystem/circulation model ([Moore \*et al.\*, 2004](#)) and prognostic equations for atmospheric CO<sub>2</sub> concentration and carbon fluxes.

Focus throughout this thesis is on the ocean component, the Parallel Ocean Program 2 ([Danabasoglu \*et al.\*, 2012](#)). The model is built on a dipolar nominal 3° staggered B-grid. Scalar variables are defined at the center of each grid and horizontal velocities at the corner with a displaced North Pole located on Greenland (see [Yeager \*et al.\*, 2006](#)). Vertical velocities are calculated at the vertical interfaces between scalar cells. There are 60 vertical layers with a vertical resolution varying from 10 m at the surface to 250 m in the deepest cell. Momentum and tracer discretization follows a second order centered advection scheme and time stepping follows a modified leapfrog scheme (for more technical details, see [Smith \*et al.\*, 2010](#)).

Advection of tracers from mesoscale eddies is parameterized using a down-gradient thickness diffusivity ([Gent and McWilliams, 1990](#); [Gent \*et al.\*, 1995](#)) with a stratification dependent diffusivity ([Ferreira \*et al.\*, 2005](#); [Danabasoglu and Marshall, 2007](#)). The same diffusivity is applied for stirring along isopycnals ([Redi,](#)

1982). Near the surface boundary, isopycnal diffusivities are modified to lie parallel to the ocean surface (*Ferrari et al., 2008; Danabasoglu et al., 2008*).

Vertical mixing is parameterized for the interior using the K-Profile Parameterization (KPP, *Large et al., 1994*). Below the boundary layer, diffusivities are calculated as a sum of diffusivities from shear instabilities, double diffusion and internal wave breaking. In the released version of POP2, internal wave breaking is parameterized in the standard formulation following *St. Laurent et al. (2002)* (Eq. 2.12).

The atmosphere component is the spectral  $3.75^\circ \times 3.75^\circ$  horizontal resolution (T31) version of the Community Atmosphere Model 4 (CAM4, *Gent et al., 2011; Shields et al., 2012; Neale et al., 2013*). The model has 26 hybrid vertical layers and contains some parameter modifications to other resolutions of CCSM4, including a turbulent mountain stress parameterization (see *Shields et al., 2012; Yeager et al., 2006*).

A dynamic-thermodynamic sea ice model, the Los Alamos Sea Ice Model (CICE) version 4 (*Hunke and Lipscomb, 2008; Jahn et al., 2012*), is coupled to POP2. It employs the same horizontal grid structure and solves the sea ice thickness distribution for each grid cell with a non-zero sea ice fraction.

Terrestrial ecosystems are represented by the Community Land Model which includes a snow cover and albedo parameterization as well as an active Carbon-Nitrogen biogeochemical model (*Lawrence et al., 2011*). Leaf and stem area indices and vegetation heights are determined prognostically, and gross primary production is calculated from leaf photosynthetic rate and corrected for nitrogen limitation. Vegetation is prescribed by three phenological types with fixed spatial distributions.

POP2 can be coupled to a marine biogeochemistry model, a combination of an upper ocean ecosystem model coupled to ocean biogeochemistry module (*Moore et al., 2004*). The marine ecosystem model is an NPZD model with three phytoplankton functional types: small phytoplankton, diatoms and diazotrophs, as well as zooplankton and (*Moore et al., 2004; Lindsay et al., 2014*). Calcifiers (Coccolithophores) are solved implicitly as a fraction of small phytoplankton. Phytoplankton growth depends on temperatures, light and nutrient availability. Nutrients include P, N, Fe and Si, where C:N:P ratios are fixed for each phytoplankton functional type and surface dust and iron fluxes are prescribed from climatology. Sinking particulate organic matter is calculated for two classes, the mineral ballast and the "soft" organic matter. The burial of  $\text{CaCO}_3$  is prescribed from the lyso-

cline depth, and remineralization and burial of soft organic matter follows [Dunne et al. \(2007\)](#).

Ocean-atmosphere fluxes of CO<sub>2</sub> are calculated through

$$J_{ocn} = k_w (1 - a_i) \Delta p\text{CO}_2, \quad (3.1)$$

where  $a_i$  is the fractional sea ice cover of each grid cell and  $\Delta p\text{CO}_2$  is the difference in partial pressure of CO<sub>2</sub> between ocean and atmosphere.  $k_w$  is the gas transfer coefficient calculated as ([Wanninkhof, 1992](#)):

$$k_w = 0.31 \text{cm hr}^{-1} \cdot U_{wind}^2 \sqrt{\frac{660}{Sc}} \quad (3.2)$$

where  $U_{wind}$  is the surface wind speed and  $Sc$  is the Schmidt-number, a function of temperature. The ocean pCO<sub>2</sub> is calculated from Eq. 2.54 with temperature and salinity-dependent equilibrium constants ([Weiss, 1974](#)).

### Known biases

There is a number of biases in the coarse resolution that are important to the following studies. Some errors are common to many coupled models, such as a double ITCZ, errors in the Gulf Stream separation as well as equatorial upwelling warm biases. Other biases are characteristic to the coarse resolution CESM, the most striking of which is the weak (but stable) AMOC, which is weaker by almost 10 Sv compared to the standard resolution CCSM4 ([Shields et al., 2012](#)). Winter sea ice cover in the northern hemisphere is excessive, in both the Labrador and Nordic Seas as well as the North Pacific. The enhanced sea ice cover is related to the poor representation of boundary currents along the Norwegian coast ([Jochum et al., 2008](#); [Shields et al., 2012](#)). The increased sea ice cover affects carbon fluxes and may also be responsible for part of the reduced AMOC strength through freshening of the North Atlantic.

Another important bias in the coarse resolution CCSM4 is the mean zonal wind stress over the Southern Ocean. While the maximum wind stress compares well with observations, a northward shift by several degrees is present in the model. As a result, Southern Ocean upwelling occurs at a displaced latitude ([Shields et al., 2012](#)).

With respect to simulating the Earth System, biogeochemistry is affected by the dynamical biases in the models. As such, upwelling, precipitation and temperature

biases also affect the global nutrient and carbon cycling. An important error in the biogeochemistry is too low surface mean and seasonal variations in chlorophyll as well as seasonal variations in primary production (*Doney et al., 2009*).

## 3.2 Implementation of IDEMIX

IDEMIX is implemented in the interior mixing routine of KPP as a substitute for the *St. Laurent et al. (2002)* scheme, which is implemented with constant latitudinal dependent background diffusivities (*Jochum, 2009; Jochum and Potemra, 2008*). The module is initialized by loading the tidal forcing field of *Jayne (2009)* (a modified version of the *Jayne and St. Laurent, 2001*, estimate). At each time-step, the tidal forcing is injected in the bottom grid cell in all columns of the ocean. The equations for the parameters  $c_0, v_0$  and  $f_e$  (Eq. 2.39, 2.42 and 2.45, respectively) are first solved using the ocean stratification and local inertial frequency. The vertical diffusive part of the internal wave energy balance, Eq. 2.37, is then calculated implicitly using a tri-diagonal solver. Horizontal fluxes arising from lateral inhomogeneities in the internal wave field are then calculated and added to the solution. The simulated dissipation rate is then input in the *Osborn (1980)* model using  $\delta = 0.2$ , in order to arrive at the vertical diffusivity.

Diffusivities are capped at a minimum and maximum threshold. For all simulations discussed here, the minimum threshold is taken as  $10^{-7} \text{ m}^2\text{s}^{-1}$ , which is 1-2 orders of magnitude smaller than  $\kappa_b$  in *St. Laurent et al. (2002)*, and the maximum is the standard  $10^{-2} \text{ m}^2\text{s}^{-1}$  used in KPP. We note that there is no capping on the dissipation rates, ensuring that at equilibrium the same amount of energy that enters IDEMIX through the tidal forcing is dissipated. The vertical viscosity is calculated from the vertical diffusivity using a Prandtl number of 10 with a separate minimum threshold for viscosity.

As the standard KPP calculates the mixing of internal waves throughout the water column, the same approach is used here. However, internal waves are not present in unstratified parts of the ocean such as deep water formation regions or the surface mixed layer. In order to accommodate this, stratification is capped at a minimum value of  $10^{-12} \text{ g cm}^{-4}$  in the IDEMIX equations, which in principle fixes the energy and dissipation in low stratification regions. This implementation in general leads to small diffusivities in weakly stratified regions where internal waves are not present, except for some regions of the uppermost surface ocean. Preliminary simulations, however, show that these diffusivities have minor impact on the

global climate and ocean circulation and can therefore be ignored. One improvement that could be implemented to overcome such issue is to parameterize mixing efficiencies as functions of stratification, such that in weakly stratified regions energy dissipated without generating any mixing (*Melet et al., 2013; de Lavergne et al., 2016*). This is left for future studies.

### 3.3 Overview of Model Runs

Throughout this work a total of 23 simulations of varying lengths and configurations will be discussed. Because Chapters 4 and 6 are written as separate studies, one published, another in review, some overlapping in naming will occur with respect to what is the "control" run of the given study. We therefore here provide a total overview of all model runs for each chapter in Table 3.1. Chapter 4 discusses the implementation of IDEMIX in the coarse resolution CCSM4 without biogeochemistry, and simulations using IDEMIX are compared to simulations using the standard *St. Laurent et al. (2002)* parameterization.

In Chapter 5 the marine biogeochemistry is briefly reviewed with the two parameterizations for pre-industrial orbital configuration.

Chapter 6 presents two simulations using IDEMIX in which the AMOC collapses and the carbon cycle response in the model is analyzed.

Finally, Chapter 7 discusses some aspects of changing the orbital configurations with regards to stratification, mixing and export production as well as forcing the IDEMIX parameterization with more internal wave energy from either tides or mesoscale eddies.

**Table 3.1:** Full overview of all model simulations analyzed and discussed throughout the thesis

CHAPTER 4				
Case	Mixing	Length	Insolation (CE)	Comments
CONT	<i>St. Laurent et al. (2002)</i>	500	1850	-
IDE	<i>Olbers and Eden (2013)</i>	500	1850	-
IEDDY	<i>Olbers and Eden (2013)</i>	500	1850	Tidal + EKE forcing
CONTF	<i>St. Laurent et al. (2002)</i>	500	1850	Ocean/ice only
CONT00	<i>St. Laurent et al. (2002)</i>	200	1850	Branch
CONT15	<i>St. Laurent et al. (2002)</i>	200	1850	Branch
IDEF	<i>Olbers and Eden (2013)</i>	500	1850	Ocean/ice only
IDEF00	<i>Olbers and Eden (2013)</i>	500	1850	Branch
IDEF15	<i>Olbers and Eden (2013)</i>	500	1850	Branch
CHAPTER 5				
CONT	<i>Olbers and Eden (2013)</i>	2000	1850	-
STLA	<i>St. Laurent et al. (2002)</i>	2000	1850	-
CHAPTER 6				
CONT	<i>Olbers and Eden (2013)</i>	2000	1850	-
THEN	<i>Olbers and Eden (2013)</i>	1000	-113,000	Branch
CHAPTER 7				
STLA	<i>St. Laurent et al. (2002)</i>	1000	1850	-
70KA_ST	<i>St. Laurent et al. (2002)</i>	1000	-70,000	-
103KA_ST	<i>St. Laurent et al. (2002)</i>	1000	-103,000	-
113KA_ST	<i>St. Laurent et al. (2002)</i>	1000	-113,000	-
CONT	<i>Olbers and Eden (2013)</i>	1000	1850	-
70KA_ID	<i>Olbers and Eden (2013)</i>	1000	-70,000	-
103KA_ID	<i>Olbers and Eden (2013)</i>	1000	-103,000	-
113KA_ID	<i>Olbers and Eden (2013)</i>	1000	-113,000	-
TIDE	<i>Olbers and Eden (2013)</i>	1000	1850	2x tidal forcing
IEDDY	<i>Olbers and Eden (2013)</i>	1000	1850	Tidal + EKE forcing

## Part II

# Scientific Results



## Chapter 4

# An energetically consistent vertical mixing parameterization in CCSM4

The following chapter presents the implementation of IDEMIX in CCSM4 and describes the qualitative and quantitative differences between two coupled simulations and six forced simulations. The text has been published in Ocean Modelling as

Nielsen, S.B., Jochum, M., Eden, C. and Nuterman, R.:

*An energetically consistent vertical mixing parameterization in CCSM4*

Ocean Modelling **127** (2018), 45-64,

doi: 10.1016/j.ocemod.2018.03.002

Figures 4.2 and 4.5 have been modified to fit the style of the rest of the thesis, and Eq. 4.7 has been re-written in terms of  $N^2$  rather than buoyancy.

## Abstract

An energetically consistent stratification-dependent vertical mixing parameterization is implemented in the Community Climate System Model 4 and forced with energy conversion from the barotropic tides to internal waves. The structures of the resulting dissipation and diffusivity fields are compared to observations, and the fidelity of the resulting temperature fields is assessed. Compared to existing biases in the control simulation, differences in surface fields are small, showing that the surface climate state is relatively robust to the choice of mixing parameterization. The thermocline structure, however, depends greatly on the details of the vertical mixing parameterizations, where the new energetically consistent parameterization results in low thermocline diffusivities and a sharper and shallower thermocline. It is also investigated if the ocean state is more sensitive to a change in forcing if the energetically consistent scheme is used compared to a tidal mixing parameterization with fixed background diffusivity. In particular we find that the Atlantic Meridional Overturning Circulation is more sensitive to changes in the Southern Ocean wind stress with the former. However, in line with previous results, changes to Southern Ocean upwelling are still largely compensated by changes to the diabatic upwelling in the Indo-Pacific basin.

## 4.1 Introduction

Mechanical energy is needed to return the deep waters that are formed at high latitudes to the surface (see e.g. [Sandström, 1908](#)). It has been hypothesized that this mechanical energy is provided by the breaking of internal waves to small scale turbulence ([Munk, 1966](#); [Munk and Wunsch, 1998](#)). This hypothesis has been supported by numerical studies ([Bryan, 1987](#); [Marotzke, 1997](#)). Yet, despite its importance, small scale turbulence in the ocean interior is still represented through diffusivity, fixed in time and space. More recently, this so called background diffusivity will be amplified near the bottom to mimic tidally induced mixing (e.g. [Bryan and Lewis, 1979](#); [St. Laurent et al., 2002](#)). However, for large parts of the ocean, away from the boundary layers, the vertical diffusivity is dominated by the background diffusivity.

The value of this background diffusivity is obtained by a combination of observations and model optimization. Using spatially-varying maps of diffusivity to match global observations rather than a constant global value has been shown to improve climate models ([Harrison and Hallberg, 2008](#); [Jochum, 2009](#)). However, while using a constant diffusivity can yield pre-industrial or present day simulations in good agreement with observations, the reliability of these parameterizations is questionable for different climate states. The model of [Osborn \(1980\)](#) suggests that vertical diffusivity,  $\kappa$ , is a function of locally dissipated energy from the internal wave field,  $\epsilon$ , and the Brunt-Väisälä frequency,  $N$ ,

$$\kappa \propto \frac{\epsilon}{N^2}. \quad (4.1)$$

Because both variables are likely to change as climate changes, we expect changes in diffusivities and therefore in ocean circulation, heat and carbon storage and uptake. Furthermore, present tidal mixing parameterizations have problems of representing observed dissipation rates due to assumptions regarding the propagation and dissipation of internal wave energy ([Waterhouse et al., 2014](#); [MacKinnon et al., 2017](#); [Kunze, 2017](#)).

The focus of this study is how climate is affected when using an energetically consistent mixing parameterization rather than using fixed background diffusivities. Studies suggest that the parameterization of interior mixing affects the simulations of pre-industrial climate (e.g. [Jayne, 2009](#); [Melet et al., 2013](#)). In particular, changes in the localization of dissipation of internal wave energy has consequences

in regions of deep water formation as well as for thermocline structure (*Melet et al., 2013, 2016*). Previous studies mainly focus on steady state properties of the ocean; here we perform a simple experiment to assess to what degree the ocean response to changed forcing is affected by the choice of parameterization.

The topic of interest for this experiment is the strength of the Atlantic Meridional Overturning Circulation (AMOC). The AMOC is a measure of the volume transport from the Southern Hemisphere to the Northern, often referred to as the "ocean conveyor belt", with sinking waters in the North Atlantic being replaced by sub-tropical surface waters through the Gulf Stream. This circulation gives rise to an Atlantic heat transport from the Southern to the Northern hemisphere. The driving mechanisms of the AMOC have been investigated and discussed throughout the last decades (see e.g. the review by *Kuhlbrodt et al., 2007*). In particular, buoyancy fluxes, diapycnal mixing rates and Southern Ocean wind stress have all been suggested to play important or even dominating roles. These also impact the strength of the Antarctic Circumpolar Current (ACC) (*Gent et al., 2001*). Several numerical studies have implicated a direct dependency of overturning to the value of diapycnal diffusivity (*Bryan, 1987; Marotzke, 1997*). Yet, many studies require mixing values larger than observed to sustain the observed rate of overturning (*Toggweiler and Samuels, 1995; Polzin et al., 1997; Ledwell et al., 1998*).

In the mid 1990's it was pointed out that Southern Ocean winds and the sill at the Drake Passage were potentially dominating global ocean upwelling, sometimes referred to as the "Drake Passage Effect" (*Toggweiler and Samuels, 1995*). Even near the limit of no vertical diffusion, the Drake Passage Effect was discovered to sustain an observed overturning (*Toggweiler and Samuels, 1998*). In a more recent study, *Munday et al. (2013)* found the overturning to be less sensitive to wind forcing as horizontal resolution increased due to the explicit generation of Southern Ocean eddies, although a sensitivity remained. Additionally, the overturning was found to be sensitive to the choice of diapycnal diffusivity regardless of model resolution. All these results were obtained by forcing an ocean model with prescribed buoyancy forcing.

In contrast to these studies *Jochum and Eden (2015)* found that in a realistic coupled climate model the AMOC is robust to changes in Southern Ocean wind stress: Changes to Southern Ocean winds and upwelling are compensated by diabatic upwelling in the Indo-Pacific basin. Their study, however, used a fixed vertical diffusivity, so that changed mixing rates due to changed ocean stratification are not present, possibly leading to an overestimation of the Indo-Pacific

compensation. Here we will revisit this idea and check if their results still hold if a fixed-energy, rather than a fixed-diffusivity parameterization is used.

The paper is structured as follows: In section 4.2 current ideas about diapycnal mixing and its parameterizations are briefly reviewed, and an energetically consistent parameterization (IDEMIX, *Olbers and Eden, 2013*) and its implementation in an ocean model are described. In Section 4.3 the results of model simulations with the standard mixing parameterization and with IDEMIX are compared in two sets: three coupled simulations (including a sensitivity study), and six forced simulations, comparing the response of the ocean to changes in the wind stress under the two different mixing schemes. In Section 4.4 the results are summarized and discussed in context to modelling, climate and future prospects.

## 4.2 Methods

### 4.2.1 Vertical mixing in ocean models

Diapycnal (from hereon simply vertical) mixing in the ocean in level coordinate ocean general circulation models is generally represented as a vertical diffusion of tracers. This process represents the conversion of small scale turbulent kinetic energy into potential energy and is important in setting the global pycnocline structure (*Munk, 1966*). It is often recognized that an average global value of  $10^{-4} \text{ m}^2\text{s}^{-1}$  is required to maintain the observed global stratification (*Munk and Wunsch, 1998*).

The energy input needed to maintain the observed ocean stratification has been estimated to be approximately 2 terawatts (TW), partitioned between winds and tides (*Munk and Wunsch, 1998; Egbert and Ray, 2000; Jayne and St. Laurent, 2001; Nycander, 2005*). Wind energy enters the ocean through the work winds do on the surface ocean, with a large fraction driving the time-mean circulation, eventually dissipating to mesoscale eddies, and some through direct generation of near-inertial waves (NIWs, see e.g. *Jochum et al., 2013*), of which only a fraction leaves the mixed-layer. Energy from mesoscale eddies is lost through numerous processes, including bottom and lateral friction and generation of lee waves over rough topography in a similar way as tidal energy loss (*Nikurashin and Ferrari, 2010*). Estimates of dissipation and diffusivity from Argo float finestructure measurements support the relationship between vertical mixing and dissipation of barotropic tides as well as geostrophic motions (*Whalen et al., 2012; Pollmann*

*et al.*, 2017).

With the recognition of the importance of tides and their signature bottom enhanced mixing, parameterizations have been developed for tidally induced mixing near the bottom. One such parameterization is the one by *St. Laurent et al.* (2002). This parameterization calculates a bottom enhanced diffusivity based on the local energy flux from tides to internal waves (taken from the model of tidal dissipation by *Jayne and St. Laurent*, 2001), by assuming that a fraction,  $q$ , of the energy that is locally converted from barotropic to internal tides is dissipated locally through a vertical distribution function which ensures bottom enhanced mixing, whereas the remaining energy radiates away and contributes to background mixing (for details, see *Simmons et al.*, 2004; *Jayne*, 2009). The mathematical expression becomes

$$\kappa = \kappa_b + \frac{q\Gamma E_{F,t}(x, y)F(z)}{\rho N^2}, \quad (4.2)$$

where  $\kappa_b$  is the background diffusivity,  $\Gamma = 0.2$  is the mixing efficiency and  $q = 1/3$  is the fraction of the energy flux from barotropic tides to internal waves,  $E_{F,t}$ , that dissipates locally, with the local dissipation being distributed vertically by an exponential decay function,  $F(z)$  and  $\rho$  being the density.

One key uncertainty is the fixed vertical decay scale,  $F(z)$ , for the dissipation of internal wave energy. This choice often does not match observations (*Kunze*, 2017), and it has been shown that the choice of a vertical dissipation profile is important for setting the ocean state (*Melet et al.*, 2013). Furthermore, the globally constant value of locally dissipated energy in Eq. 4.2,  $q$ , relies on sparse observations and there is little justification that one value is representative of the entire ocean (*Waterhouse et al.*, 2014). Recent work has now provided a theoretical background to take a step in parameterizing small scale turbulence through directly computed values for dissipated energy, as described below.

### 4.2.2 IDEMIX

A recent paper proposes the model Internal Wave Dissipation, Energy and Mixing (IDEMIX, *Olbers and Eden*, 2013), to be implemented in a global ocean model. Although extensions to the model have been developed (*Eden and Olbers*, 2014), we will here use the first version as described in *Olbers and Eden* (2013) due to the simplicity and as the main focus is how the ocean and climate responds when the vertical mixing is defined from a constant energy flux compared to a fixed

background diffusivity in space and time.

Through a set of assumptions and simplifications, IDEMIX calculates the total internal wave energy,  $E$ , as well as the dissipation of internal wave energy,  $\epsilon_{IW}$ .  $E$  is calculated by solving a single differential equation obtained from the spectral radiation balance of a weakly interacting wave field:

$$\frac{\partial E}{\partial t} - \frac{\partial}{\partial z} \left( c_0 \tau_v \frac{\partial c_0 E}{\partial z} \right) - \nabla_h \cdot v_0 \tau_h \nabla_h v_0 E = -\epsilon_{IW} + \mathcal{S}, \quad (4.3)$$

where the second and third terms on the l.h.s. are the vertical and horizontal transport of  $E$ , respectively.  $\mathcal{S}$  represents the sum of local sources of internal wave energy.

IDEMIX has been discussed in several papers already, ([Olbers and Eden, 2013](#); [Eden et al., 2014](#); [Eden and Olbers, 2014](#); [Pollmann et al., 2017](#)) and will therefore only be summarized briefly here. In order to arrive at Eq. 4.3, upward and downward propagating waves are first treated separately, and the wave energy is integrated over all wave numbers in each vertical wave number half-space. Equations for the sum of energy,  $E$ , and difference,  $\Delta E$ , of the two half-spaces are then simplified by assuming approximate symmetry in vertical wave number,  $m$ , and that nonlinear wave-wave interactions work to eliminate  $\Delta E$  through an exponential relaxation with decay scale  $\tau_v$ . The wave speed is also assumed to have the same value for the upward and downward propagating waves,  $c_0$ . The value of  $c_0$  can be found by assuming a Garrett-Munk (GM) like internal wave energy spectrum. The third term on the l.h.s. of Eq. 4.3 represents the lateral propagation of energy, with  $v_0$  a horizontal average group velocity and  $\tau_h$  a relaxation time for horizontal anisotropies (similar to  $\tau_v$ ).

The model is closed on the r.h.s. of Eq. 4.3 by setting

$$\epsilon_{IW} = \mu_0 f_e \frac{m_\star^2}{N^2} E^2, \quad (4.4)$$

which represents the energy flux at high vertical wavenumber (a combination of calculations of [McComas and Müller, 1981a](#); [Heyney et al., 1986](#)) with  $m_\star$  the bandwidth in vertical wavenumber and  $\mu_0$  a constant ([McComas and Müller, 1981a](#)). Finally,  $f_e = f \operatorname{arccosh}(N/f)$ .

The dissipation of energy is then related to a vertical diffusivity through the

*Osborn* (1980) model:

$$\kappa = \frac{\delta}{1 + \delta} \frac{\epsilon_{IW}}{N^2} = \frac{\delta}{1 + \delta} \mu_0 f_e \frac{E^2}{c_\star^2 N^2}, \quad (4.5)$$

where the relation  $m_\star = N/c_\star$  is used with  $c_\star = \frac{1}{j_\star \pi} \int_{-h}^0 N(z) dz$ , with  $j_\star$  the modal bandwidth of the GM-model.

### 4.2.3 Model and Implementation

Eq. 4.3 is implemented in the ocean component of the Community Climate System Model 4 (CCSM4, *Gent et al.*, 2011), the Parallel Ocean Program (POP2, *Danabasoglu et al.*, 2012) following the implementation of *Eden et al.* (2014) with the parameter values suggested by *Olbers and Eden* (2013):  $\mu_0 = 4/3$ ,  $\delta = 0.2$ ,  $j_\star = 10$ ,  $\tau_v = 1$  day and  $\tau_h = 10$  days. First, Eq. 4.3 is solved with a tri-diagonal solver without the lateral propagation term, which is then added explicitly to the solution afterwards. Diffusivities obtained through Eq. 4.5 are capped at a minimum of  $10^{-7} \text{ m}^2\text{s}^{-1}$  (molecular level) and a maximum of  $10^{-2} \text{ m}^2\text{s}^{-1}$ .

A total of 9 experiments are carried out using the coarse resolution version of CCSM4 (*Shields et al.*, 2012). The ocean component uses a horizontal nominal  $3^\circ$  resolution with 60 vertical layers of increasing thickness. In the surface layers are 10 m thick, ranging to several hundred meters in the deepest ocean. First, a coupled control simulation using the T31  $\times$  3 configuration, CONT, is run for 500 years using a latitudinal dependent background diffusivity ( $0.01 \text{ cm}^2\text{s}^{-1}$  at Equator,  $0.3 \text{ cm}^2\text{s}^{-1}$  at  $30^\circ\text{N/S}$  and  $0.17 \text{ cm}^2\text{s}^{-1}$  elsewhere, *Jochum*, 2009) with bottom-enhanced diffusivity calculated from Eq. 4.2. This is then compared to a similar 500 year long run where the background and tidal induced diffusivities are replaced by the IDEMIX module, referred to as IDE, forced with only the conversion of barotropic to baroclinic tides using the same forcing as CONT (*Jayne and St. Laurent*, 2001; *St. Laurent et al.*, 2002; *Jayne*, 2009). Analysis is carried out for the years 450-499.

One extra sensitivity simulation, IEDDY, includes an additional energy source from mesoscale eddies as calculated from the simple dissipation form of *Eden and Greatbatch* (2008), where mesoscale eddy energy is converted to internal wave energy by

$$\epsilon_{eddy} = 0.1 L^2 \sigma^3, \quad (4.6)$$

with  $L$  being the minimum of the first baroclinic Rossby radius of deformation and the Rhines scale, and  $\sigma = f\mathbf{u}_z/N$  is the Eady growth rate. This parameterization of eddy forcing adds energy to the internal waves everywhere in the ocean, in particular near eddying currents such as the ACC, western boundary currents and the Tropics (see e.g. figure 1d of [Eden et al., 2009](#)).

Eddy forcing of IDEMIX can be implemented in different ways ([Eden et al., 2014](#)). Here we choose the simplest form of local injection in Eq. 4.3. This may not be the ideal implementation, but the reasoning behind the simulation is to see what effect adding more energy to the parameterization has, not how the choice of injection optimizes the simulations (here we refer the reader to [Eden et al., 2014](#); [Pollmann et al., 2017](#)). The background for the sensitivity experiment comes from the fact that IDEMIX falls short of explaining observed dissipation rates without mesoscale eddy forcing ([Pollmann et al., 2017](#)). However, as CONT is only forced with tidal forcing, the main comparison experiment, IDE, is also forced with tides only. For an energetically consistent implementation the eddy forcing should be calculated from the used thickness diffusivity (in our simulations calculated according to [Danabasoglu and Marshall, 2007](#)). Other ways to implement other energy would be from estimates of lee wave energy fluxes ([Nikurashin and Ferrari, 2011](#); [Melet et al., 2014](#)). Our implementation compares with the horizontal structure of such estimates. The choice of Eq. 4.6 is based on the simplicity from the fact that it is already directly implemented in POP2 ([Eden and Greatbatch, 2008](#); [Eden et al., 2009](#)). IEDDY will be used only when discussing adding extra forcing to the

**Table 4.1:** Summary of model setups. Case explanation: OCN: ocean/sea ice. FULL: fully coupled.  $p$  is the SO wind multiplication factor

	Case	Mixing	$p$
CONT	FULL	<a href="#">St. Laurent et al. (2002)</a>	–
IDE	FULL	<a href="#">Olbers and Eden (2013)</a>	–
IEDDY	FULL	<a href="#">Olbers and Eden (2013)</a> ; <a href="#">Eden and Greatbatch (2008)</a>	–
CONTF00	OCN	<a href="#">St. Laurent et al. (2002)</a>	0.0
CONTF	OCN	<a href="#">St. Laurent et al. (2002)</a>	1.0
CONTF15	OCN	<a href="#">St. Laurent et al. (2002)</a>	1.5
IDEF00	OCN	<a href="#">Olbers and Eden (2013)</a>	0.0
IDEF	OCN	<a href="#">Olbers and Eden (2013)</a>	1.0
IDEF15	OCN	<a href="#">Olbers and Eden (2013)</a>	1.5

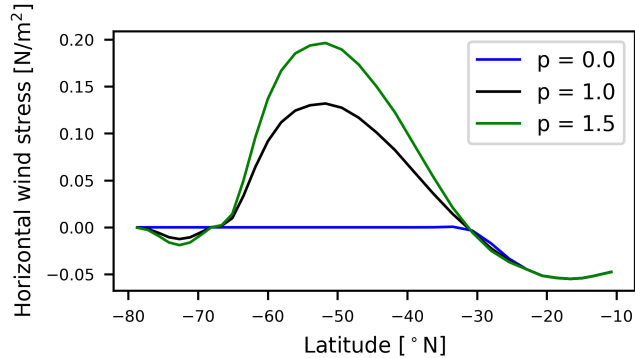


**Figure 4.1:** The horizontal wind stress over the Southern Ocean in the three experiments of each set of forced simulations.

IDEMIX parameterization. Note that the simple additional energy source by Eq. 4.6 is most likely an overestimation of the effect of eddies (as discussed in [Eden et al., 2014](#)).

In order to revisit the Indo-Pacific upwelling discussed by [Jochum and Eden \(2015\)](#), a set of three ocean/ice simulations with COREv2 Normal Year Forcing ([Large and Yeager, 2004](#)) with a sea surface salinity restoring timescale of one month are performed for both parameterizations of mixing. Each set consists of a 500 year control simulation, CONTF and IDEF. Each control simulation is accompanied by branched runs from year 300: One where winds over the Southern Ocean south of 35°S are shut off by multiplying the wind stress with a value  $p = 0$ , CONTF00 and IDEF00, and one where the Southern Ocean winds are increased by 50% by setting  $p = 1.5$ , CONTF15 and IDEF15. Between 35 and 25°S  $p$  is reduced linearly to 1. The wind profiles are depicted in Fig. 4.1. Each branch is run for 200 years. The forced simulation are analyzed for years 490-499. The model setups are summarized in table 4.1.

Reducing the background diffusivity in simulations using IDEMIX comes with the risk of making the model more prone to numerical noise, but this has been found only to pose issues in marginal seas (e.g. the Baltic and Caspian Seas, which only span few grid points and are not connected to the major basins in the coarse resolution POP2), for which reason the background diffusivities in these basins are set to the same value in IDEMIX simulations as in the control simulations.

Section 4.3 first considers the coupled simulations and response in climate, and then deals with the two sets of forced simulations.

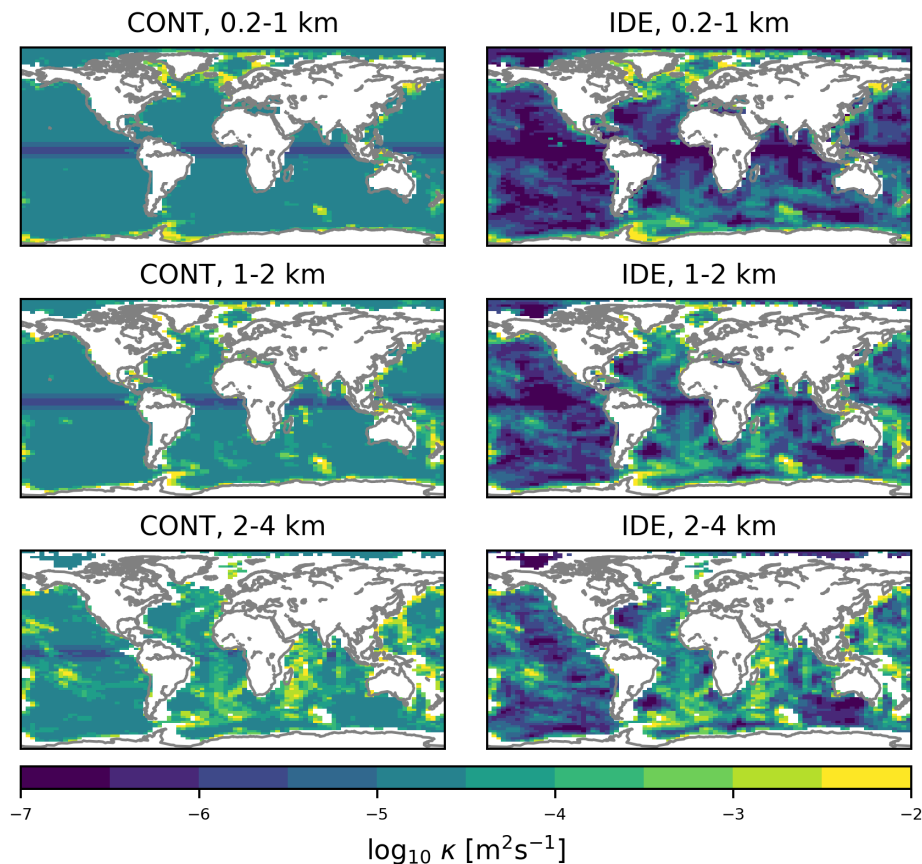


**Figure 4.2:** Global map of diffusivities for CONT (left column) and IDE (right column) averaged over 0.2-1 km depth (upper row), 1-2 km depth (middle row) and 2-4 km depth (bottom row).

## 4.3 Results

### 4.3.1 Coupled simulations

We begin by assessing the differences between the two coupled simulations, CONT and IDE, beginning with the diffusivities followed by the differences in climatology. Global maps of the diffusivities (in this case only background diffusivities and tidal mixing as calculated by Eq. 4.2 in CONT and diffusivities as calculated by Eq. 4.3 and 4.5 in IDE) are presented in Fig. 4.2, averaged over three depth intervals: 0.2-1 km, 1-2 km and 2-4 km. The upper 200 m have been excluded because mixed and boundary layer diffusivities in IDE contaminate the signal of the thermocline structure due to the low stratifications within these. The pattern of bottom enhanced diffusivity due to topography is the same for the two simulations at all depths. This is expected as both parameterizations have the same tidal energy in-

duced at the same bottom cells. The difference is in how the energy is distributed globally, as only 1/3 of the energy is dissipated locally in CONT and the rest is not considered but assumed to contribute to the background diffusivity, whereas IDE injects all the energy and distributes it through Eq. 4.3. CONT is largely characterized by the latitudinal dependent background diffusivity (*Jochum, 2009*), whereas IDE is characterized strongly by the bottom topography and displays a more heterogeneous diffusivity pattern. The diffusivities have been observed to be heterogeneous (*Whalen et al., 2012; Pollmann et al., 2017*), although the pattern here does lack much of the observed structure, likely due to only using tidal energy as forcing. In all depth intervals, IDE has large regions of reduced diffusivities compared to CONT. In the upper layer, the three major basins all have smaller diffusivities in IDE than CONT, showing a tendency for very small thermocline diffusivities. However, regions of larger diffusivities are also present, which is particularly connected to regions of weak stratification in the high latitudes and over rough topography. Between 1-2 km in the Equatorial band, the Pacific and the South Australia Basin have lower diffusivities than the imposed background level in CONT, which is also valid for the 2-4 km interval. These regions are associated with abyssal plains with very low tidal energy input to the internal waves. The diffusivities close to rough topography, on the other hand, are generally the same magnitude or somewhere even larger in IDE. This suggests that more energy is dissipated locally (or at least very close to injection) in IDE than the 1/3 used in CONT, and that the horizontal propagation of  $E$  is very weak compared to the vertical propagation term and the dissipation.

The left panel of Fig. 4.3 shows the distribution of grid points with a specific diffusivity. It is evident that where CONT has a very narrow peak around diffusivities just above  $10^{-5} \text{ m}^2\text{s}^{-1}$ , IDE has a more broad distribution of diffusivities, but also has distinct peaks at the two cut-off ends of the spectrum. Note that there is almost an order magnitude more points at the higher end of the spectrum in IDE than CONT due to the global dependency on stratification throughout the water column and not just near the bottom, which increases the diffusivity greatly in the surface layers within the mixed layer. The histogram also displays that a large number of grid points in IDE have diffusivities smaller than in CONT. From Fig. 4.2 we can infer that these points are in particular located in the Tropics and Sub-Tropics over abyssal plains and are not only confined to the deep ocean but also the upper parts of the ocean below the mixed and boundary layers.

On the right panel of Fig. 4.3 globally averaged profiles of the diffusivities are

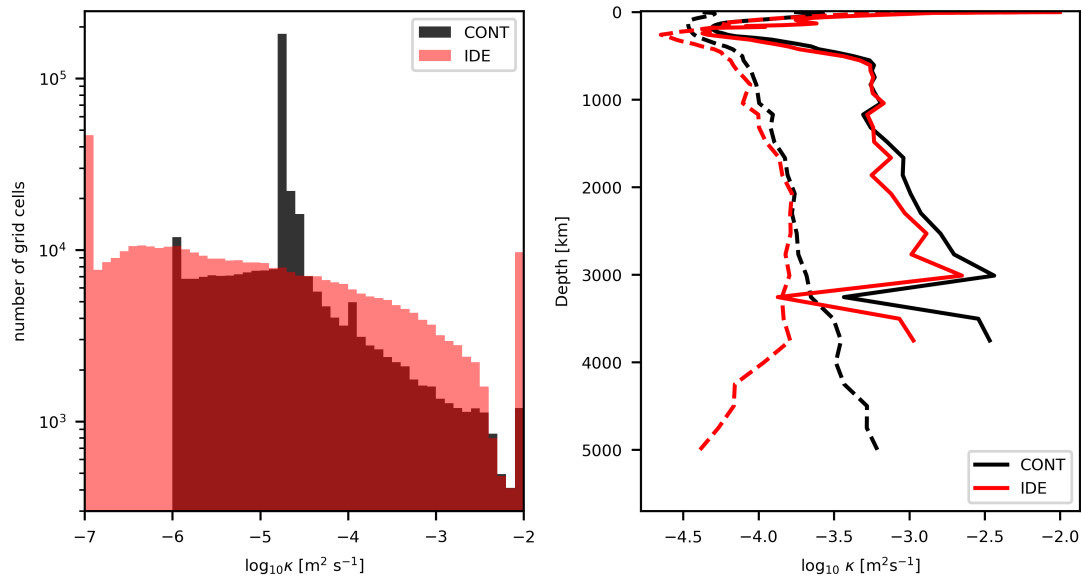


**Figure 4.3:** Left: Histogram of diffusivities in CONT (black) and IDE (pink). Red indicates the overlap of the two. Note the logarithmic vertical axis. Right: Globally averaged vertical diffusivity profile for CONT (black) and IDE (red). Solid lines indicate diffusivities over rough topography (slopes larger than 0.01) and dashed indicate smooth topography.

plotted. Solid lines indicate diffusivities over rough topography (defined here as bathymetry slopes larger than 0.01), and dashed lines indicate diffusivities over smooth topography. Only water columns with depths greater than 500 m are included. This shows that CONT has up to an order magnitude larger diffusivities than IDE in the very deep ocean over smooth topography. This is a result of the deep ocean points which have very little injection of tidal energy in the abyssal plains, causing many points to be of small magnitude in IDE (see Fig. 4.2) in the deep ocean, in contrast to the rather large background diffusivity in CONT. Between 1-4 km depth, the two models have very similar global profiles. In the upper 200 m the stratification dependency in IDE shows up in very large diffusivities.

The global power consumption to raise the potential energy due to vertical mixing is estimated as the global integral

$$\mathcal{P} = \int_V \kappa \rho N^2 dV, \quad (4.7)$$

where  $N^2 = g\rho_0^{-1}d\rho/dz$ , which yields a total of 0.26 TW for CONT of which 0.12 TW is dissipated below 500 m, and 0.30 TW for IDE of which only 0.08 TW is dissipated below a depth of 500 m.

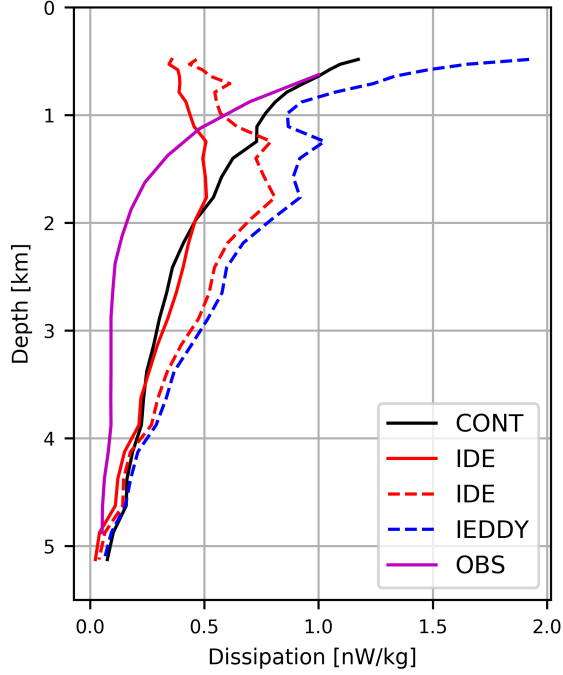


**Figure 4.4:** Globally integrated dissipation of energy for CONT (solid black), IDE (solid red) and observations (*Kunze, 2017*, , dashed magenta). The red dashed curve represents IDE evaluated using Eq. 4.4. The dashed blue line represents IEDDY where extra energy forcing is added to Eq. 4.3, evaluated using Eq. 4.4.

The vertical distribution of dissipated energy per unit volume divided by the density of water, yielding the dissipation per unit mass, is shown in Fig. 4.4 for CONT (black) and IDE (red) along with a global composite of fine-structure estimates (*Kunze, 2017*, magenta line). The dashed red curve is calculated directly from Eq. 4.4, whereas solid curves are calculated by dividing the integrand of Eq. 4.7 with the mixing efficiency. This estimate is derived as no direct estimate of dissipation is calculated in CONT. Unstably stratified grid points are omitted as assumptions for fine structure as well as parameterizations are not valid under these conditions. As can be seen, using diffusivity and stratification to derive the dissipation in IDE (solid red) underestimates the amount of dissipation calculated by Eq. 4.4 (dashed red). Both parameterizations show too much dissipation in the deep regions of the ocean and in particular at mid-depth, but dissipation in CONT is more in line with observations above 1 km, where the dissipation rate in IDE is too small and does not resemble fine-structure estimates. That both models have too much dissipation in the deep ocean suggests too much deep dissipation of tidal energy. For IDE, discrepancies with observations might be related to either a poor representation of propagation of energy or missing energy sources in the

upper ocean. To investigate the latter, the sensitivity study IEDDY has been carried out, where conversion of mesoscale eddy energy to internal wave energy is added in Eq. 4.3. The resulting dissipation profile (from Eq. 4.4) is added in Fig. 4.4 as the dashed blue line. It is seen that eddy energy forcing increases the interior dissipation rates in particular in the upper 2 km. A different choice of implementation of mesoscale eddy dissipation may alter this distribution, but this is beyond the scope of this study. It should be noted that the fine-structure estimates sample mostly the major ocean basins whereas the model estimates are global averages. Furthermore, the uncertainty is large in the deep ocean where observations are sparse (*Kunze, 2017*).

The average AMOC strength at 26°N is 14.3 Sverdrups ( $1 \text{ Sv} = 10^6 \text{ m}^3\text{s}^{-1}$ ) for CONT and 13.4 Sv for IDE. Thus, the different dissipation in IDE is accompanied by a weaker AMOC. This may be a reflection in changed mixing in waters associated with deep water formation (*Melet et al., 2016*), although the AMOC reduction is not necessarily a direct result of the mixing parameterization but could be due to feedbacks in buoyancy or wind forcing from the atmosphere. However, wintertime convection depths in the North Atlantic are shallower in IDE than CONT, suggesting the AMOC reduction to be caused by reduced production of North Atlantic Deep Water (not shown).

Changes in the surface fields are generally small. Fig. 4.5 shows the sea surface temperature (SST) difference between IDE and CONT. Note that CONT has several biases (discussed in *Shields et al., 2012*), the most prominent ones being related to the western boundary currents and the upwelling regions such as the Benguela system west of southern Africa, where the amplitude of the biases are larger in IDE than CONT. The root-mean-squared error (RMSE) for CONT is 1.67 and somewhat larger for IDE with a RMSE of 1.90 (reduced to 1.80 in IEDDY, not shown).

Superimposed on the upper panel of Fig. 4.5 is the 15% sea ice concentration lines for CONT (black) and IDE (red). The two lines almost coincide, with IDE having a slightly more northward extent of sea ice in the Southern Ocean, and a slightly more southward extent in the Bering Sea. The North Atlantic sea ice extent is comparable, but sea ice concentrations are greater within parts of the ocean in IDE, most remarkably in the Baffin Bay (not shown). The sea ice extent is already too large in CONT (*Shields et al., 2012*), but is stable within the two parameterization schemes.

The lower panel of Fig. 4.5 shows the precipitation difference between IDE and

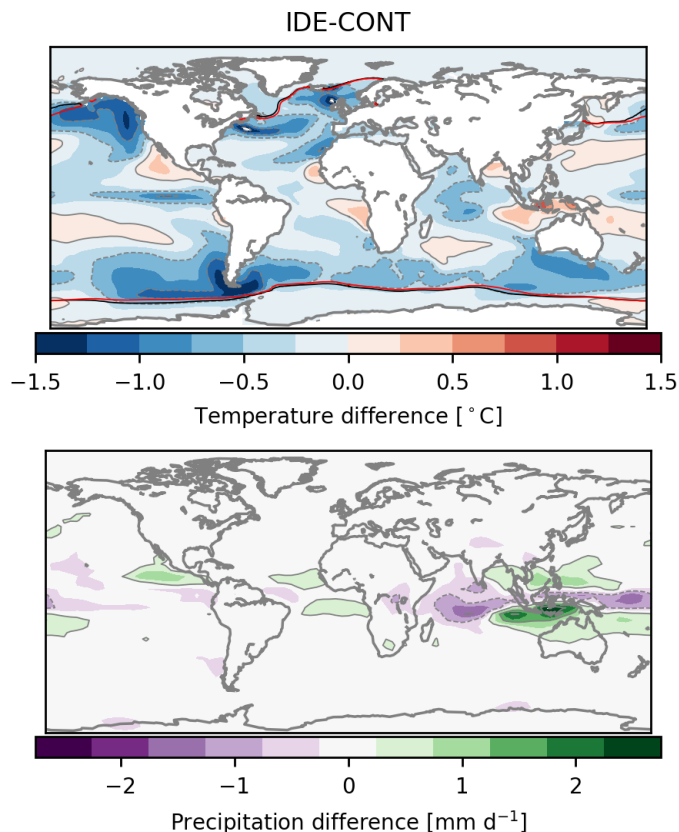


**Figure 4.5:** SST (upper) and precipitation (lower) difference between IDE and CONT.

CONT. Differences are confined to the Tropics. Two major patterns are visible. The first is an increase in precipitation in the double-ITCZ seen over the Pacific and Atlantic. These changes are rather small and related to the modest increase in SST in the upwelling regions. The biggest change occurs over the Indian Ocean and the Indonesian seas, related to a difference in SST in the same region. This precipitation pattern is related to the diffusivity in the Banda Sea region (*Jochum and Potemra, 2008*). In CONT, this region has enhanced background vertical diffusivity made to match observations of a large tidally induced mixing in the region, which causes a reduction in the SST which heavily influences precipitation. This mixing is not captured in IDE, which may either be due to a too low energy input from tides or in the way the energy propagates into the region in the IDEMIX parameterization.

Fig. 4.6 shows the meridional distribution of temperature difference between the two simulations, overlaid with contours ( $5^{\circ}\text{C}$  intervals) from CONT (dashed), IDE (solid) and World Ocean Atlas 2009 (WOA, *Locarnini et al., 2010*, dotted).

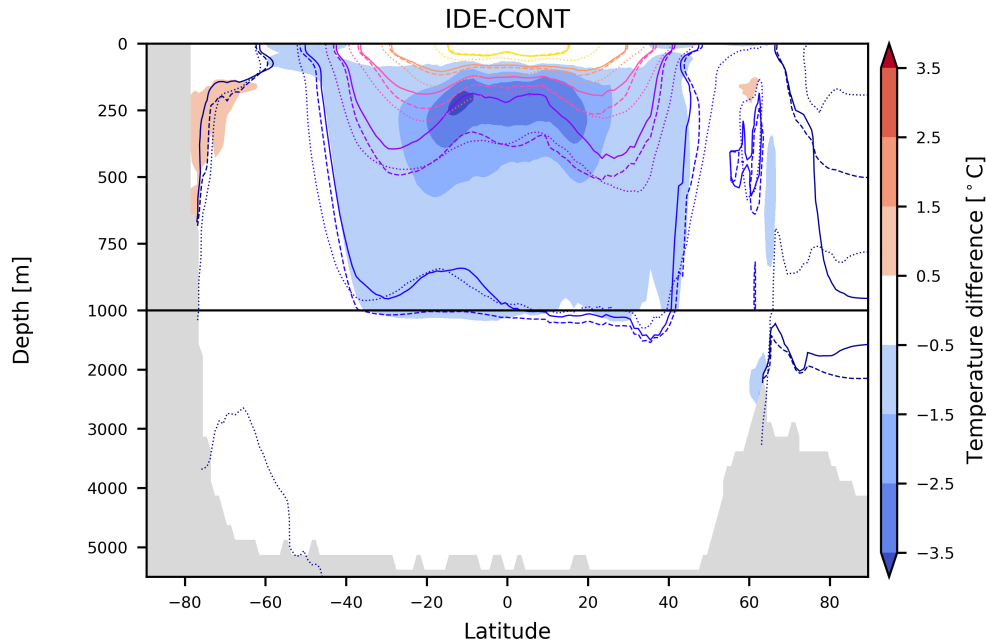


**Figure 4.6:** Difference between zonally averaged temperature in IDE and CONT. Overlying contours are zonally averaged potential temperature of CONT (dashed), IDE (full) and WOA (dotted). Contour interval is  $5^{\circ}\text{C}$ , ranging from  $0^{\circ}\text{C}$  (dark blue in polar regions) to  $25^{\circ}\text{C}$  (yellow). Note the non-linear vertical axis at 1000 m.

A large difference in the simulations is in the thermocline. IDE has a sharper and shallower thermocline which causes temperatures to be cooler between 100 and 1000 m depth. This is seen in particular in the waters between  $5^{\circ}\text{C}$  and  $15^{\circ}\text{C}$  which are shallower in IDE compared to both CONT and observations, causing the temperature stratification to be in less agreement with observations. At mid-depth, however, IDE is closer to observations seen in the close agreement with the observed  $5^{\circ}\text{C}$  isotherm. The rest of the global ocean has temperature differences with amplitude less than  $0.5^{\circ}\text{C}$ . The large differences between CONT and IDE occur in the upper km which is also the region of the largest discrepancy in dissipated energy in Fig. 4.4, and in the region of small diffusivities in the Pacific and Atlantic, causing a reduced diffusion of heat from the surface, making the deep ocean largely colder and lifting the isotherms relatively to CONT. Evidently, the amount of energy used for mixing, but also its distribution vertically and horizontally, plays a major role in setting the thermocline structure (in agreement with earlier studies such as [Bryan, 1987](#); [Samelson, 1998](#); [Melet et al., 2016](#)).

**Table 4.2:** Absolute strength in overturning circulations in the forced simulations. All units in Sv ( $1 \text{ Sv} = 10^6 \text{ m}^3 \text{ s}^{-1}$ ).

	AMOC	PMOC
CONTF00	11.7	-21.4
CONTF	15.8	-10.3
CONTF15	18.5	-7.5
IDEF00	9.5	-14.8
IDEF	13.5	-5.0
IDEF15	16.6	-4.1

### 4.3.2 Forced experiments

We now turn to the forced simulations with changed wind stress. Resulting diffusivities, SSTs and thermocline structure are similar as for the coupled simulations (not shown) and will not be discussed further, as the focus of the forcing experiments is how the ocean responds to changes in forcing.

As can be seen in Fig. 4.1, the wind stress for  $p = 1.5$  peaks at almost  $0.2 \text{ N/m}^2$  compared to  $0.13$  for  $p = 1.0$ . This change in wind stress alters the wind stress curl over the Southern Ocean and forces increased Ekman driven upwelling. For  $p = 0$ , the wind stress curl is zero and the corresponding Ekman driven upwelling is zero.

The residual meridional overturning circulations (RMOC, from hereon simply MOC), defined as the sum of the Eulerian mean and the eddy-induced overturning streamfunctions for the Atlantic (AMOC) and Indo-Pacific (PMOC, calculated as the global MOC subtracted the AMOC, minimum overturning north of  $35\text{S}$ ) averaged over the last 10 model years are listed in Table 4.2. The AMOC strength at  $26^\circ\text{N}$  is plotted in Fig. 4.7. CONTF has an AMOC strength of  $15.7 \text{ Sv}$  after 300 years and  $15.8 \text{ Sv}$  after 500 years compared to  $13.5 \text{ Sv}$  at both times in IDEF, suggesting that although not nearly equilibrated, the model is stable enough for our purposes. Also, the weaker AMOC seen in the coupled runs is also reflected in the forced runs. As with coupled runs, shallow North Atlantic boundary layer depths in IDE suggest a reduced production of North Atlantic Deep Water to be the cause of this.

As can be seen, increasing (decreasing) winds results in an initial, quick response where the AMOC increases (decreases) over the first 30 years. After this initial, transient response, a more gradual increase (decrease) follows. The initial

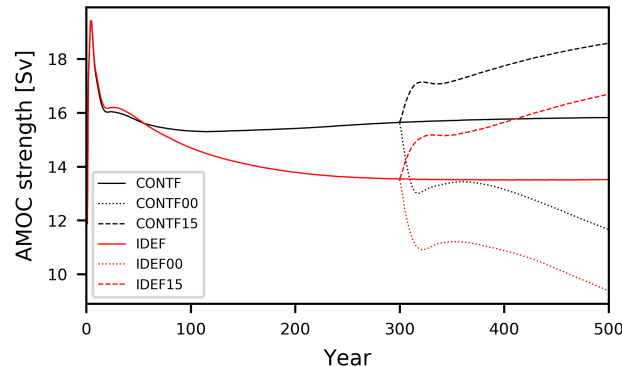


**Figure 4.7:** AMOC strength (in Sv) at  $26^{\circ}\text{N}$  in the forced simulations. Wind stress perturbations start at year 300.

relative increase in AMOC strength in CONTF15 is 9% after 30 years of perturbation and by the end in year 500 the AMOC strength has increased by 18%. For IDEF15 relative to IDEF the values are 12% and 24%, respectively. Correspondingly for  $p = 0.0$  the values of CONTF00 relative to CONTF are a 16% and 26% decrease in AMOC strength, and for IDEF00 the decrease corresponds to 18% and 31% relative to IDEF. It follows that the relative sensitivity towards changing wind stress is larger in simulations with the *Olbers and Eden (2013)* parameterization, whereas the absolute values are comparable.

The PMOC for the six experiments is plotted in Fig. 4.8 along with the average depth of the  $\sigma_{\theta} = 27.7 \text{ kg m}^{-3}$  isopycnal. The relative increase in strength of the upwelling (PMOC in Table 4.2) for IDEF00 is 194%, and the relative reduction in IDEF15 is 17%. For CONTF00 and CONTF15 these numbers are 106% and 27%, respectively. The absolute changes in PMOC in experiments with  $p = 0$  compares roughly to the strength of the AMOC in the corresponding runs.

Thus, as in *Jochum and Eden (2015)*, simulations without any wind stress over the Southern Ocean yield an enhanced upwelling in the Indo-Pacific, which at least in part compensates the missing upwelling in the Southern Ocean and sustains an AMOC at least for several centuries following the beginning of the wind stress perturbation.

The  $27.7 \text{ kg m}^{-3}$  isopycnal shoals 200-300 m in the Pacific and deepens in the Southern Ocean in both experiments with  $p = 0$ , compared to simulations with  $p = 1$ , flattening and shallowing the isopycnal. For  $p = 1.5$  the isopycnal steepens over the Southern Ocean and deepens by up to 200 m at  $40^{\circ}\text{S}$  and about 100 m north of this latitude. Thus, while the relative changes in streamfunction are

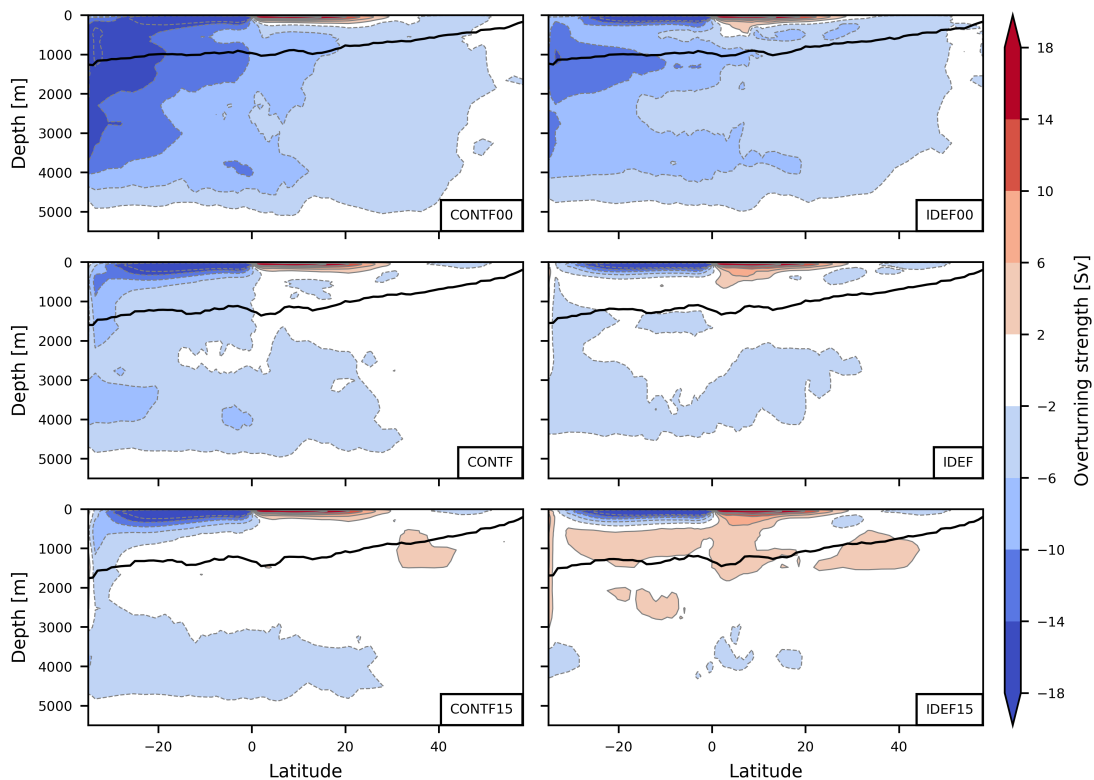


**Figure 4.8:** Indo-Pacific overturning stream function for the six forced experiments. Contour interval is 4 Sv. The black line denotes the average depth of the  $\sigma = 27.7$  isopycnal.

different with the two parameterizations, the impact of the winds on the pycnocline depth is very similar in the two cases. Thus, despite diffusivities depending on the stratification, the Indo-Pacific overturning response in IDEF simulations is, in absolute sense, comparable to the response in CONTF simulations.

## 4.4 Summary and Discussion

Three coupled ocean, atmosphere and sea ice (including a sensitivity run) and six forced ocean/sea ice simulations, have been carried out to assess the impact of the vertical mixing parameterization IDEMIX (*Olbers and Eden, 2013*) in the ocean component of CCSM4. The coupled simulations, CONT, IDE and the sensitivity study IEDDY, are run for 500 years and the forced CONTF and IDEF are run for 300 years, at which time wind stress perturbations over the Southern Ocean are performed and simulations are run for 200 years more. It has been shown that the way in which the dissipation of energy is localized globally impacts the ocean

state and related climate (in agreement with earlier studies such as [Samelson, 1998](#); [Melet et al., 2013](#)). The most prominent differences occur in setting the thermocline depth. Reduced thermocline diffusivities cause less heat to be mixed downward, causing a sharper and shallower thermocline, consistent with other studies ([Melet et al., 2016](#)). The relationship between thermocline structure and diffusivities implies that large differences in heat and carbon storage can occur over long timescales depending on the mixing parameterization, something that is left for future studies to assess.

For the coupled simulations minor changes are observed in the SSTs and precipitation fields. The representation of precipitation and SSTs in IDE is worse than in CONT. However, compared to the already existing biases in CONT, the differences between IDE and CONT are small. Also, the overall climate state is very comparable in the two runs. The SST differences in IDE are adding to already existing biases, which implies that with improved parameterizations of vertical mixing the biases might be reduced.

The Benguela upwelling system is one area in the model with an already existing bias that gets worse in IDE. The nature of the bias has been studied and is thought to be a result of several processes ([Xu et al., 2014](#); [Harlaß et al., 2015](#)). In particular, vertical mixing has been suggested to be one of the contributing mechanisms in generating temperature biases in POP2 ([Xu et al., 2014](#)). Our results support this hypothesis and suggest that either energy forcing or propagation is not adequately represented in the region. It is also possible that a more realistic description of vertical mixing enhances the SST bias because a previous compensation with other model errors is relaxed. The same holds for other model biases, highlighting the need for more careful representation of vertical mixing in climate models.

While the errors in surface fields are larger in IDE than CONT in some areas, IDEMIX is developed from physical principles, whereas the existing parameterization uses the background mixing to match diffusivities to observations, which may not hold in studies of paleoclimate or future predictions. It is furthermore interesting to note that while both simulations are missing energy sources from e.g. mesoscale eddies, the contribution from these is easily implemented as forcing terms in IDEMIX if one can calculate the energy transfer to the internal wave field, whereas the existing model requires a new parameterization for each energy source that needs to be included. Using IDEMIX, the problem is reduced to the investigation of how and where energy enters the internal wave field ([Eden et al.,](#)

2014).

The large amount of grid points with diffusivities below  $10^{-6} \text{ m}^2 \text{ s}^{-1}$  in IDE seen in Fig. 4.2 and in the left panel of Fig. 4.3 may not be realistic, but suggest that more energy forcing to the internal wave field is needed. Our sensitivity study, IEDDY, is preliminary, but indicates that adding energy sources in IDEMIX might indeed bring the simulation closer to observed estimates of dissipation rates in the thermocline and thus improve climate simulations. However, this requires careful treatment of each individual source of internal wave energy. For instance, for coarse resolution ocean models, tidal energy may be put in too deep in the water column which might in turn affect overturning strengths (*Schmittner and Egbert, 2014*). Other improvements might be found by separate treatment of low mode internal waves (*Eden and Olbers, 2014*).

Finally, the present results show that trapped waves and their dissipation in the Banda Sea is not well represented in the current parameterization of IDEMIX. It is not clear how such waves, which are unresolved in climate models, and their associated dissipation should be parameterized and implemented in IDEMIX, but as with the case of the Banda Sea, these are of climatic importance and other areas might exist where similar wave dissipation is important in setting the mixing strength.

With regards to the forced simulations, we find that the relative importance of the Southern Ocean wind stress on AMOC strength is larger in IDEF than CONTF, whereas absolute changes are similar. It is therefore likely that the difference in relative importance of winds is a result of the changed background state and its associated weaker AMOC observed in IDEF. Both parameterizations find a similar compensation in the Indo-Pacific when the wind stress is shut off over the Southern Ocean, in agreement with *Jochum and Eden (2015)*. A key difference compared to their results is that without wind stress the AMOC is declining toward a weak state, whereas they found the AMOC to be independent of the wind stress. However, the nature of forced ocean/ice experiments do not allow for atmospheric feedbacks which might modify this result (*Rahmstorf and England, 1997*).

## Acknowledgments

This study was supported by The Danish Council for Independent Research, Natural Sciences, 4002-00397. Simulations were done with support from the High

Performance Computing Centre at the University of Copenhagen. The authors would also like to thank Eric Kunze for fine structure estimates of internal wave dissipation and Nils Brüggemann and Dirk Olbers for helpful comments.



# Chapter 5

## Mixing and Marine Biogeochemistry

The simulations discussed in Chapter 4 were coupled simulations without the marine biogeochemistry module coupled to POP2. In Chapter 6, two simulations using the IDEMIX module coupled to marine biogeochemistry are discussed. It is therefore important to bridge the gap between Chapter 4 and 6 by discussing the difference in ocean biogeochemistry with the *St. Laurent et al. (2002)* scheme and IDEMIX. In this chapter, two coupled versions of the coarse resolution CESM1.2 with an active marine biogeochemistry and ecosystem module are run for 2000 years and compared averaged over the last hundred model years. The simulation using *St. Laurent et al. (2002)* is referred to as STLA, and the simulation using IDEMIX is referred to as CONT. The setup includes prognostic equations for atmospheric pCO<sub>2</sub> based on fluxes of carbon between ocean, land and atmosphere. As the simulations are similar to the ones described in the previous chapter in terms of simulated mixing rates, sea surface temperatures and precipitation (although mildly modified due to radiative feedbacks from the prognostic, atmospheric pCO<sub>2</sub>), attention in this chapter is strictly on the carbon cycle. Table 5.1 summarizes the two simulations with respect to atmospheric pCO<sub>2</sub>, AMOC strength measured at 26°N, export production, calculated as the flux of particulate organic carbon and CaCO<sub>3</sub> across 100 m depth, and global ocean ideal age,

**Table 5.1:** Overview of coupled carbon cycle runs. Export Production is calculated as the flux of particulate organic carbon and CaCO<sub>3</sub> across 100 m depth. Ideal age is the global average age of the ocean below 100 m.

Case	pCO <sub>2</sub> [ppmv]	AMOC [Sv]	Exp. P. [PgC yr <sup>-1</sup> ]	Ideal Age [yr]
STLA	291.8	15.0	8.22	799
CONT	257.6	12.4	5.69	866

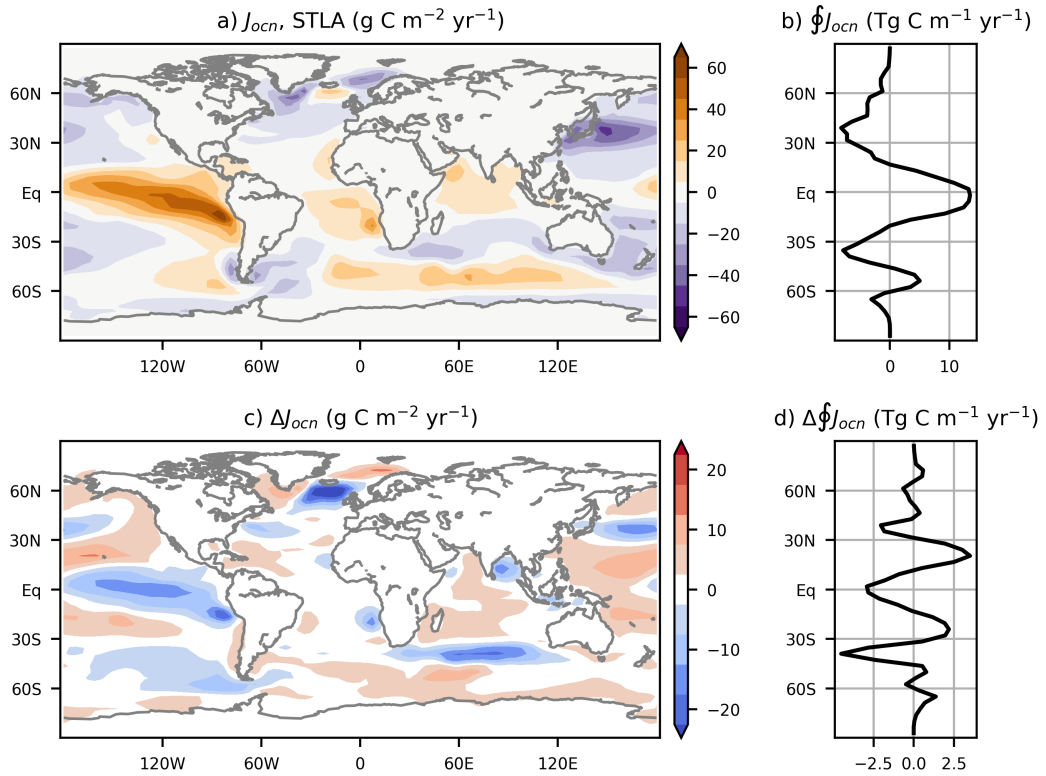


**Figure 5.1:** a: Surface carbon fluxes in STLA (positive from ocean to atmosphere). b: Zonally integrated surface fluxes in STLA. c: Surface flux difference between CONT and STLA. d: Zonally integrated surface flux anomalies.

a passive tracer in the model that is set to 0 at the surface and increases by one each model year as long as the water parcel is shielded from the surface. As in the previous chapter, AMOC strength is reduced when employing IDEMIX, a combination of the North Atlantic surface stratification and thermocline mixing rates. This leads to a reduction in ventilation age in CONT compared to STLA seen in increased ideal age in CONT.

Fig. 5.1a shows the surface fluxes of carbon in STLA,  $J_{ocn}$ . The pattern compares qualitatively well with observed fluxes (*Takahashi et al., 2009; Jochum et al., 2010*). Supersaturated waters upwell in the tropics and the Southern Ocean and release carbon to the atmosphere, and undersaturated waters in the North Atlantic and mid-latitudes remove carbon from the atmosphere (Fig. 5.1b). It is important to note that the outgassing is too large in the tropics and too small in the Southern Ocean compared to pre-industrial estimates (*Gruber et al., 2009*).

CONT simulates surface fluxes with the same spatial patterns, but with differences in the magnitude of fluxes (Fig. 5.1c,d). Most notable are the reduced

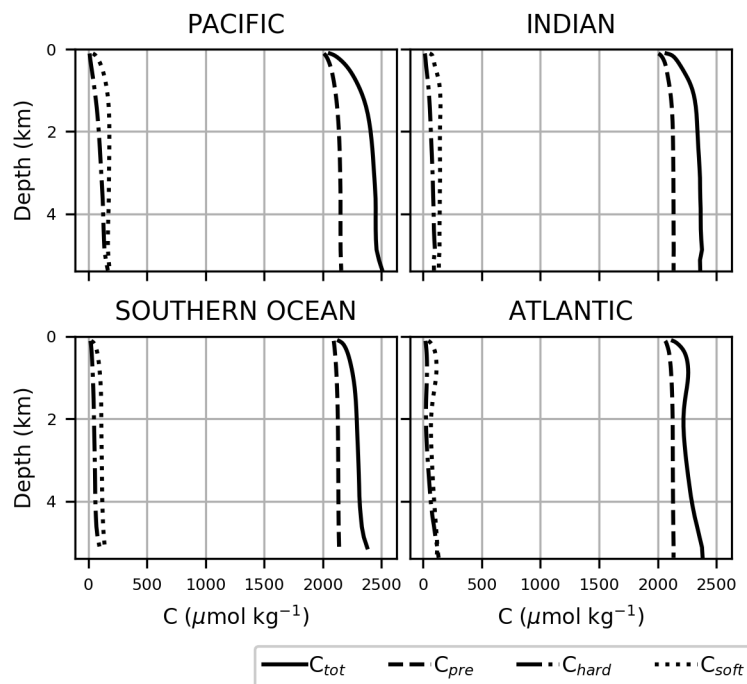


**Figure 5.2:** Average ocean column carbon concentrations in STLA separated into total DIC (solid), preformed carbon (dashed), soft-tissue carbon (dotted) and carbonate (dash-dotted) split between the four major basins.

tropical outgassing and the increased outgassing in the Atlantic and Indian sector of the Southern Ocean. The increased outgassing in the Southern Ocean is compensated by a large increase in carbon uptake in the southern Indian Ocean. The increased Southern Ocean and reduced tropical outgassing can be attributed to the reductions in diabatic mixing in the thermocline in CONT which, as discussed in the previous chapter, leads to a change in the partitioning between waters upwelling in the Southern Ocean and tropics, as well as a slightly increased wind stress over the Southern Ocean in CONT compared to STLA.

The carbon inventory is decomposed and quantified as described in Chapter 2.4, shown for the four major basins in STLA in Fig. 5.2. Most carbon is stored as preformed carbon (the solubility and disequilibrium pump combined). Carbonate and organic carbon together accounts for less than 10% of the total carbon.

The carbon concentration difference between CONT and STLA is shown in Fig. 5.3. Overall the ocean accumulates more carbon in CONT than STLA, except for the deep Pacific and Indian where DIC is lost. The overall gain in DIC can be attributed to the increased solubility arising from the cooling of the global ocean (see Fig. 4.5 and 4.6) and particularly an increase in remineralized soft

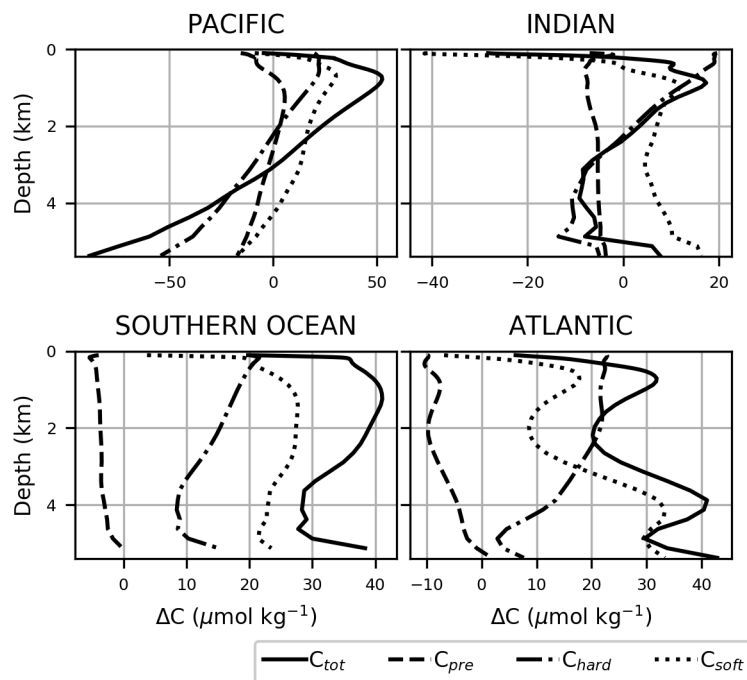


**Figure 5.3:** Average ocean column carbon concentrations difference between CONT and STLA separated into total DIC (solid), preformed carbon (dashed), soft-tissue carbon (dotted) and carbonate (dash-dotted) split between the four major basins.

and hard-tissue carbon induced by the reduced ventilation of the global ocean, indicated by the increase in global ocean age (Table 5.1). The Atlantic Ocean particularly experiences an increase in deep hard tissue and organic carbon. Despite increased solubility, preformed carbon content is reduced compared to STLA. Since the global ocean temperature is lower in CONT than STLA, this can either be attributed to a decrease in the disequilibrium part of the preformed carbon or to errors in the carbon inventory decomposition. The method of calculating the preformed carbon by subtracting soft and hard tissue carbon from total DIC leads to an underestimate of preformed carbon, since the back calculation method overestimates the strength of the soft-tissue pump (*Ito et al., 2004*). Thus, part of the increase in soft-tissue carbon can in fact be attributed to an increase in the disequilibrium in oxygen, which increases the error in the equation of  $C_{\text{soft}}$ .

The reduced ventilation of deep and intermediate waters and reduced mixing across the thermocline leads to a decrease in surface nutrient concentrations and as a result a 30% reduction in export production (calculated as the flux across 100 m of the sum of particulate organic carbon and  $\text{CaCO}_3$ , see Table 5.1). *Eggleston*

*and Galbraith (2018)* propose that changes in the soft-tissue pump strength can best be quantified by the product of the average global age of the ocean and export production. The soft-tissue pump is stronger in CONT than STLA, in contrast to the relation suggested by *Eggleston and Galbraith (2018)*. This discrepancy can partly be attributed to the overestimate of  $C_{\text{soft}}$ . Furthermore, we note that changes in export production in the simulations of *Eggleston and Galbraith (2018)* are generally small, and that ventilation poses the strongest constraint on  $C_{\text{soft}}$ .

Overall, CONT has a colder ocean but less preformed carbon. The soft and hard tissue carbon inventory are increased due to poorer ventilation of the deep waters, which increases the concentrations of remineralized carbon. As a result, atmospheric  $\text{pCO}_2$  is lower, and the terrestrial carbon inventory is smaller (not shown). The next chapter deals with a drastic perturbation of the climate system in simulations employing the IDEMIX scheme. We note that the differences described here can impact the climate response to external forces (*Menviel et al., 2008; Obata, 2007*).



## Chapter 6

# Two-timescale carbon cycle response to an AMOC collapse

The following chapter analyzes the carbon cycle response to an AMOC collapse using an oceanic vertical mixing parameterization that responds globally to changes in stratification. It is currently under review as a journal article in *Paleoceanography and Paleoclimatology* as:

Nielsen, S.B., Jochum, M., Pedro, J., Eden, C. and Nuterman, R.:  
*Two-timescale carbon cycle response to an AMOC collapse*  
In Review, *Paleoceanography and Paleoclimatology*

## Abstract

Atmospheric CO<sub>2</sub> concentrations (pCO<sub>2</sub>) varied on millennial timescales in phase with Antarctic temperature during the last glacial period. A prevailing view has been that carbon release and uptake by the Southern Ocean dominated this millennial-scale variability in pCO<sub>2</sub>. Here, using Earth System Model experiments with an improved parameterization of ocean vertical mixing, we find a major role for terrestrial and oceanic carbon releases in driving the pCO<sub>2</sub> trend. In our simulations, a change in northern hemisphere insolation weakens the Atlantic Meridional Overturning Circulation leading to increasing pCO<sub>2</sub> and Antarctic temperatures that are consistent with observations. The simulated rise in pCO<sub>2</sub> is caused in equal parts by increased CO<sub>2</sub> outgassing from the global ocean due to a reduced biological activity and changed ventilation rates, and terrestrial carbon release as a response to southward migration of the Intertropical Convergence Zone and associated drought over tropical Africa. The simulated terrestrial carbon contribution to the pCO<sub>2</sub> rise is supported by recent evidence from ice core  $\delta^{13}\text{C}$  measurements. Our results show that parallel variations in Antarctic temperature and pCO<sub>2</sub> do not necessitate that the Southern Ocean dominates carbon exchange; instead changes in carbon flux from the global ocean and land carbon reservoirs can explain the observed pCO<sub>2</sub> (and  $\delta^{13}\text{C}$ ) changes.

## 6.1 Introduction

During the last glacial Greenland temperatures experienced abrupt fluctuations between warm (interstadial) and cold (stadial) conditions as observed in ice core water stable isotopes, often referred to as Dansgaard-Oeschger (DO) events (*Dansgaard et al., 1993*). DO events appear to be part of a major, global reorganization of the climate system. Associated with the Greenland interstadials is an increase in monsoon strength in China, (*Wang et al., 2001*) and a decrease in monsoon strength in the southern South America (*Wang et al., 2006; Kanner et al., 2012*). Stadials are characterized by an opposite hemispheric monsoon response, as well as reduced strength of the Atlantic Meridional Overturning Circulation (AMOC) inferred from Pa/Th ratios (*Böhm et al., 2015; Henry et al., 2016*). Antarctica tends to warm during the Greenland stadials and cool during the Greenland interstadials (*EPICA community members, 2006; WAIS Divide Project Members, 2015*). The peaks in Antarctic warming, termed Antarctic Isotope Maximum (AIM) events, are the largest of these and are accompanied by increases in atmospheric CO<sub>2</sub> concentrations (pCO<sub>2</sub>) by up to 20 ppmv (*Ahn and Brook, 2008, 2014*).

Recent measurements of  $\delta^{13}\text{C}$  of air trapped in ice core bubbles show that  $\delta^{13}\text{C}$  decreased in phase with rising pCO<sub>2</sub> during the Marine Isotope Stage 3 (MIS3) stadials, which suggests an organic source of carbon to the atmosphere (*Bauska et al., 2018*). Organic sources of carbon could either be terrestrial release or changes in the marine biological activity.

The close relationship between Antarctic temperatures, pCO<sub>2</sub> and  $\delta^{13}\text{C}$  changes in Atlantic intermediate waters during longer stadials lead *Ahn and Brook (2008)* to suggest a Southern Ocean control on the pCO<sub>2</sub> increase. Marine sediment core records of biogenic silica, a proxy for upwelling, also suggest an increase in Southern Ocean ventilation during stadials (*Anderson et al., 2009*), which could increase Southern Ocean outgassing of CO<sub>2</sub>. Recent model studies support increased formation rate of Antarctic Bottom Water as a mechanism for increasing pCO<sub>2</sub> (AABW, *Menviel et al., 2015, 2018*).

Due to the evidence of weak Atlantic overturning during AIM events, numerical studies have analyzed the response of the carbon cycle to overturning collapses induced by freshwater forcing in the North Atlantic. Studies of vegetation responses to AMOC collapses find loss of terrestrial carbon to the atmosphere in boreal regions (*Scholze et al., 2003*) or the tropics (*Köhler et al., 2005; Obata, 2007; Bozbiyik et al., 2011*). Other studies find increased atmospheric pCO<sub>2</sub> as a

result of changed ocean dynamics from reduced strength of the biological pump (*Schmittner, 2005; Schmittner and Galbraith, 2008*).

The majority of previous studies have employed simplified model setups, either by decoupling the carbon cycle from the climate models (*Scholze et al., 2003; Köhler et al., 2005*), or by using models of intermediate complexity (*Bouttes et al., 2012; Menviel et al., 2008, 2015*). One common feature, regardless of the choice of model used, is that vertical mixing in the ocean is parameterized using a constant background diffusivity. Such parameterization does not take into account changes in the energy provided for mixing caused by breaking of internal waves, or changes in the local stratification caused by perturbations in the ocean forcing. However, drastic circulation changes induced by an AMOC collapse have been identified to cause intermediate warming of the ocean (e.g. *Brown and Galbraith, 2016; Pedro et al., 2018*). As a result, ocean stratification and mixing rates should be affected, leading to changes in heat and carbon storage as well as feedback on the circulation.

In this paper we present a fully coupled climate model with active biogeochemistry where a combination of mixing and insolation changes drives an AMOC shutdown, releasing CO<sub>2</sub> to atmosphere comparable to those associated with stadials. Our simulations consist of a 1000 year spin-up and a 1000 year long perturbation simulation using an Earth System Model. The length of the simulations reveals a two-timescale response to the collapse of the overturning circulation, a fast response causing terrestrial release of carbon, and a slow oceanic release of carbon due to a reduced biological pump. A thousand years after the perturbation, the terrestrial and oceanic release of carbon each account for roughly half the pCO<sub>2</sub> difference to the control simulation.

Our setup is different from previous studies in two important ways. First of all, the collapse of the overturning circulation in our model is forced without freshwater forcing, but is instead a result of a combination of the climate state prior to insolation perturbation and the sea ice export to the North Atlantic following the perturbation. Thus, we do not force the model with any virtual salt fluxes, but have the collapse of the overturning evolve internally, in line with recent studies suggesting that DO events can be triggered by stochastic forcing without freshwater forcing (*Peltier and Vettoretti, 2014; Kleppin et al., 2015; Brown and Galbraith, 2016; Zhang et al., 2017*). Secondly, we use a recent parameterization for vertical mixing, with which we can investigate feedbacks in the ocean system caused by large changes in the stratification (*Olbers and Eden, 2013; Nielsen et al., 2018*).

The paper is structured as follows. In section 6.2 the vertical mixing parameter-

ization is briefly presented along with model and the experimental setup. Section 6.3 present the simulated response to the change in orbital forcing in terms of ocean circulation and carbon fluxes. The results are discussed in section 6.4 and finally a summary and conclusion is given in section 6.5.

## 6.2 Methods

### 6.2.1 Vertical mixing

Breaking internal waves in the ocean convert small scale turbulent kinetic energy to potential energy. This process has in ocean models historically been represented as a constant diffusivity (e.g. [Bryan, 1987](#)). Empirical parameterizations of tidal mixing have been added to the global background diffusivities ([St. Laurent et al., 2002](#); [Simmons et al., 2004](#); [Jayne, 2009](#)), and recently more sophisticated parameterizations that account for how the energy that is put into the internal waves and eventually lost by dissipation have recently been developed ([Polzin, 2009](#); [Olbers and Eden, 2013](#); [Melet et al., 2016](#)).

The parameterization of internal wave breaking has consequences for the heat and carbon storage in the ocean ([Bryan, 1987](#)). We hypothesize that the changed stratification resulting from an AMOC collapse affects the deep mixing of the ocean which has impact on the global biogeochemistry. In order to test this we apply a recently proposed vertical mixing parameterization, IDEMIX ([Olbers and Eden, 2013](#)).

Internal wave energy,  $E$ , and dissipation rate,  $\epsilon_{IW}$ , are computed directly for each grid cell in the ocean, and by using the [Osborn \(1980\)](#) model a vertical diffusivity can be obtained. The equation for  $E$  becomes:

$$\frac{\partial E}{\partial t} - \frac{\partial}{\partial z} \left( c_0 \tau_v \frac{\partial c_0 E}{\partial z} \right) - \nabla_h \cdot v_0 \tau_h \nabla_h v_0 E = -\epsilon_{IW} + \mathcal{S}, \quad (6.1)$$

where  $c_0$  and  $v_0$  are the vertical and horizontal wave speeds, and  $\tau_v$  and  $\tau_h$  are vertical and horizontal elimination timescales of anisotropies in the wave field.  $\mathcal{S}$  represents sources of energy. In our simulations we force IDEMIX with tides only ([Jayne and St. Laurent, 2001](#)). The diffusivity is calculated from the dissipation of internal wave energy and is parameterized as

$$\kappa = \frac{\delta}{1 + \delta} \frac{\epsilon_{IW}}{N^2} = \frac{\delta}{1 + \delta} \mu_0 f_e \frac{E^2}{c_*^2 N^2} \quad (6.2)$$

where  $c_\star = N^2/m_\star^2$  with  $m_\star$  being the modal bandwidth,  $\mu_0$  a constant and  $f_e = \text{farccosh}(N/f)$  and  $\delta = 0.2$ . For further description of the parameterization, we refer to previous studies (*Olbers and Eden, 2013; Eden and Olbers, 2014; Pollmann et al., 2017*).

### 6.2.2 Model setup

We use the coarse resolution version of the Community Earth System Model ver. 1.2 (*Gent et al., 2011; Danabasoglu et al., 2012; Shields et al., 2012; Hurrell et al., 2013*). The ocean resolution varies with latitude so that zonal extent is 400 km near the Equator and 20 km at the poles, ranging from 400 km to 40 km in the meridional resolution with largest values in the North Pacific. There are 60 vertical layers with non-uniform thickness, ranging from 10 m at the surface to 500 m at the bottom. The implementation of IDEMIX in CESM follows that of *Nielsen et al. (2018)*. The ocean model is run with the *Gent and McWilliams (1990)* parameterization using a stratification dependent thickness and isopycnal diffusivity (*Danabasoglu and Marshall, 2007*).

The atmospheric model uses a T31 spectral truncation in the horizontal with 26 vertical layers. Biogeochemistry is coupled to the climate system and actively exchanges carbon between ocean, atmosphere and land. The ocean component includes diatoms, phytoplankton and diazotrophs, with phytoplankton growth controlled by temperature, light and available nutrients (N, P, Si, Fe, *Moore et al., 2004, 2013; Lindsay et al., 2014*). The land component prognostically computes leaf and stem area indices and vegetation height using a prescribed spatial distribution of plant functional types (*Lawrence et al., 2011; Lindsay et al., 2014*).

The model is spun up from climatologies and an ocean at rest for 1000 years using pre-industrial (i.e. 1850 Common Era, C.E.) orbital forcing. At model year 1000, the simulation branches in two, one control simulation using the same orbital configuration as in the spin-up, CONT, and one simulation where the orbital forcing is changed to that of 113,000 years before the Common Era (113 ka B.C.E.). We will refer to this simulation as THEN. Both simulations are run for an additional 1,000 years. Analysis is carried out for the mean of the last 100 model years, unless stated otherwise.

Within the first two centuries after changing the orbital configuration, the AMOC strength measured at 26°N collapses from 12.5 Sv (Sverdrup, 1 Sv =  $10^6 \text{ m}^3 \text{ s}^{-1}$ ) to below 5 Sv in THEN. The shutdown is a result of increased sea ice export

**Table 6.1:** Overview of model runs listing the year of orbital configuration and pCO<sub>2</sub> and AMOC strength averaged over the last hundred years of simulation.

Case	Orbital configuration	pCO <sub>2</sub> [ppmv]	AMOC [Sv]
CONT	1850 C.E.	257.6	12.5
THEN	-113 B.C.E.	266.5	4.5

from the Nordic Seas to the North Atlantic, increasing the surface stratification and inhibiting deep water formation (*Jochum et al., 2010*). By reducing the AMOC strength in this way we are free of any assumptions regarding localization and strength of an applied freshwater forcing, and the mechanism adds to the increasing number of processes that could have caused stadial conditions other than input of freshwater from ice sheets (e.g. *Peltier and Vettoretti, 2014*; *Kleppin et al., 2015*; *Zhang et al., 2017*). Whether the cause of Greenland stadials is related to direct input of freshwater or not, we note that *Brown and Galbraith (2016)* recently found that the global response of climate models to AMOC perturbation is robust to the choice of mechanism by which the AMOC is weakened.

We note that CONT has a reduction of pCO<sub>2</sub> of 30 ppmv compared to the pre-industrial value that the model is initiated with, which is 287.4 ppmv. This can be attributed to the effects of the mixing parameterization, where in particular thermocline mixing is reduced compared to standard parameterizations using a fixed background diffusivity, causing the thermocline to be sharper and shallower, cooling the ocean and increasing its solubility (*Nielsen et al., 2018*). As the ocean cools and solubility increases, this also reduces the radiative forcing of CO<sub>2</sub>, acting as a positive feedback on ocean surface temperatures.

## 6.3 Results

The surface temperature difference between the THEN and CONT,  $\Delta T$ , is shown in Figure 6.1. The reduced oceanic heat transport from the southern to the northern hemisphere results in a large scale, bipolar temperature anomaly typical for simulations with collapsed overturning circulations (*Brown and Galbraith, 2016*; *Pedro et al., 2018*). The AMOC strength measured at 26°N is reduced from 12.5 Sv in CONT to just 4.5 Sv in THEN (see Table 6.1). As a result, strong cooling takes place in most of the northern hemisphere, in particular in the North Atlantic and Arctic where reduced heat transport results in expansion of the sea ice area in addition to the weaker summer insolation.

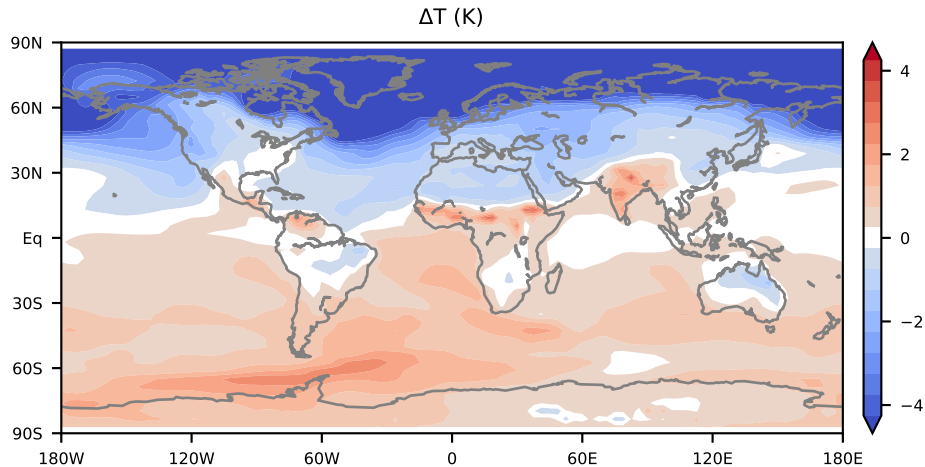


**Figure 6.1:** Surface temperature difference between THEN and CONT.

Figure 6.2a shows the zonally averaged ocean temperature difference between THEN and CONT. As discussed in [Pedro et al. \(2018\)](#), the AMOC collapse results in an intermediate warming of the ocean that spans the entire Atlantic Ocean until  $\sim 60^\circ\text{S}$  where the ACC acts as a barrier for signal propagation ([Cox, 1989](#); [Huang et al., 2000](#); [Schmittner et al., 2003](#)). The deep ocean cools in THEN, which is caused by increased deep water formation in the Ross Sea (not shown). The intermediate warming and deep ocean cooling causes an increase in the Atlantic stratification between 1 and 3 km depth with a peak increase with more than a doubling at 2 km depth and a deep ocean decrease in stratification (Figure 6.2b), as well as a small increase in deep Pacific stratification below 2 km depth (Figure 6.2c).

The temperature evolution in the simulations shows a rapid decrease in temperature over Greenland of more than 6 K in THEN within the first few centuries of branching off, shown in Figure 6.3a. This temperature drop is at the lower end of estimated Greenland coolings during transitions into stadials ([Kindler et al., 2014](#)). For Antarctica ( $90^\circ\text{S}$ - $80^\circ\text{S}$ ), temperatures initially drop, but rise a few centuries after the perturbation (Figure 6.3b). By the end of the simulation, Antarctica is  $\sim 0.5\text{K}$  warmer in THEN than CONT. The rate of warming compares with that during AIM events, but the amplitude of warming falls short of the few Kelvin estimated for the largest AIMS. Here, however, the orbital configuration changes reduce solar insolation over Antarctica, as seen in the initial cooling in THEN, opposing the later warming caused by the AMOC collapse.

Compared to CONT, atmospheric  $\text{pCO}_2$  in THEN increases rapidly within

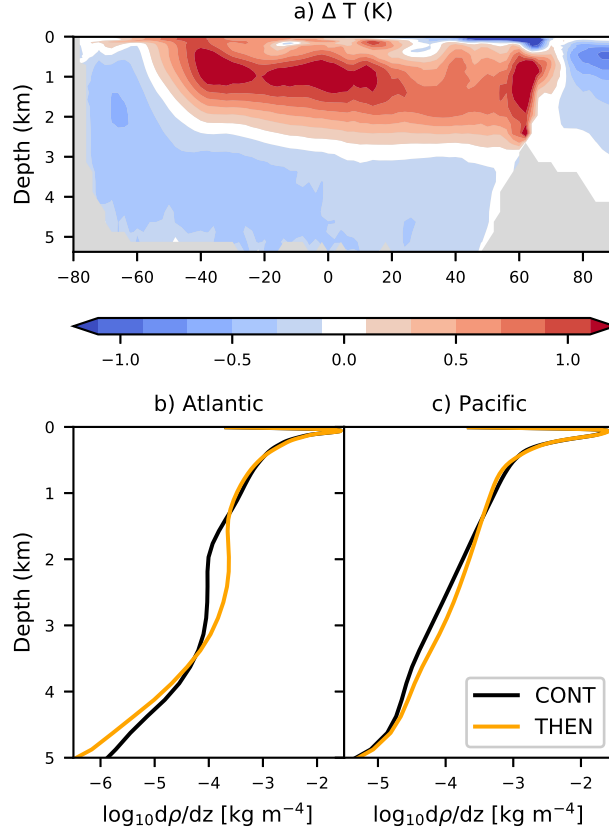


**Figure 6.2:** a: Zonally averaged ocean temperature difference between THEN and CONT. b: Ocean stratification averaged over the Atlantic basin for CONT (black) and THEN (yellow). c: Same as (b) but for the Pacific Ocean.

the first two centuries (Figure 6.3c) and then continues to rise slowly, but at a faster rate compared to CONT. By the end of the simulation, pCO<sub>2</sub> in THEN is ~9 ppmv larger than CONT (Table 6.1). This amounts to an almost 1 ppmv per century release of CO<sub>2</sub> to the atmosphere on average in THEN compared to CONT, which is comparable to observations from Antarctica over longer stadials (*Ahn and Brook, 2014*).

We separate the carbon fluxes,  $J_{tot}$ , into  $J_{ocn}$  (ocean-atmosphere fluxes) and  $J_{lnd}$  (land-atmosphere fluxes). The total change in pCO<sub>2</sub> is determined by the sum of the two,

$$\frac{dpCO_2}{dt} \propto J_{tot} = J_{ocn} + J_{lnd}. \quad (6.3)$$

As fluxes vary strongly on inter-annual, annual and seasonal timescales, we integrate Eq. 6.3 in time and compare the difference in cumulative fluxes between THEN and CONT,  $\Delta \int J dt$ . The resulting curves are presented in Figure 6.3d.

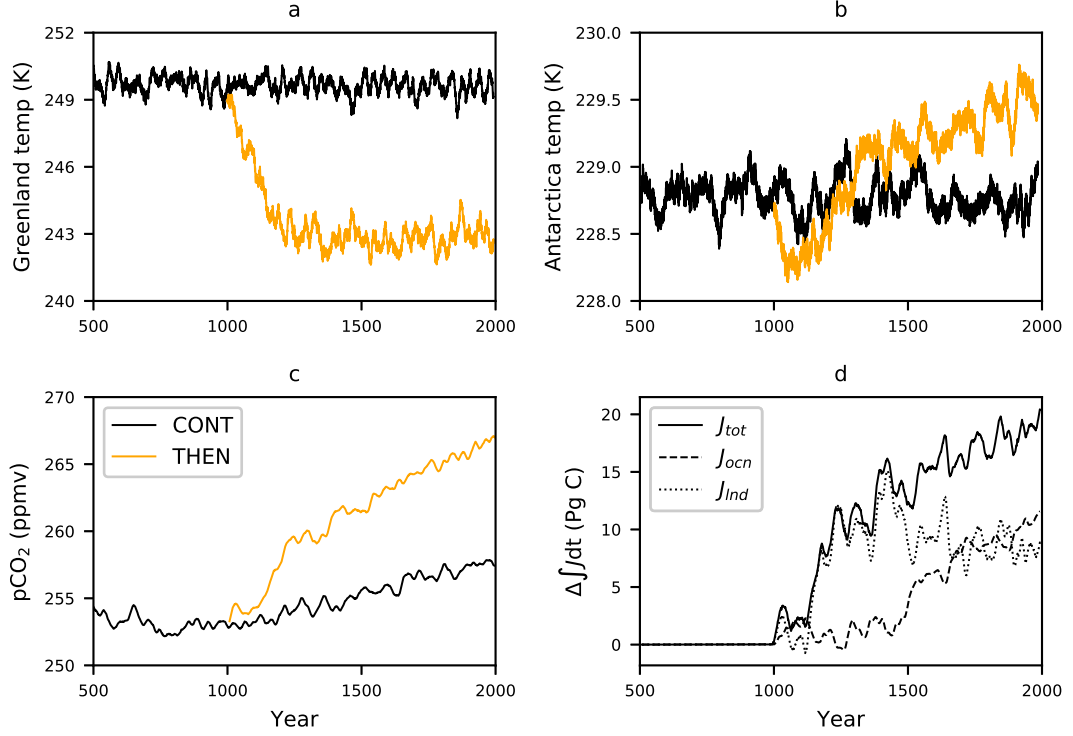


**Figure 6.3:** Time evolution (15-year running means, except for b) for CONT (black) and THEN (yellow). a: Surface air temperature averaged over Greenland ( $70^{\circ}\text{N}$ - $80^{\circ}\text{N}$ ,  $50^{\circ}\text{W}$ - $30^{\circ}\text{W}$ ). b: Surface air temperature over Antarctica ( $80^{\circ}\text{S}$ - $90^{\circ}\text{S}$ , 30-year running mean). c: Globally averaged  $\text{pCO}_2$ . d: Difference in cumulative flux of carbon to the atmosphere between THEN and CONT from the ocean (dashed), land (dotted) and total (solid).

Solid lines denote total flux to the atmosphere, dashed lines ocean fluxes and dotted lines terrestrial fluxes. Two timescales emerge to be relevant for the  $\text{pCO}_2$  differences between the two simulations: a rapid terrestrial release of carbon between 100 and 300 years of perturbation in THEN, and a slow oceanic release of carbon. The initial increase in  $\text{pCO}_2$  during the first century, roughly 1 ppmv, is caused by a terrestrial reorganization due to the insolation change. By the end of the simulation, each climate component has contributed by roughly half of the total increase in  $\text{pCO}_2$ . Where  $\Delta \int J_{\text{land}} dt$  is slowly decreasing again after 500 years, i.e. land reclaims carbon,  $\Delta \int J_{\text{ocean}} dt$  continues to rise throughout the simulation.

We now investigate the fluxes related to each component of the carbon cycle, beginning with the fast terrestrial response.

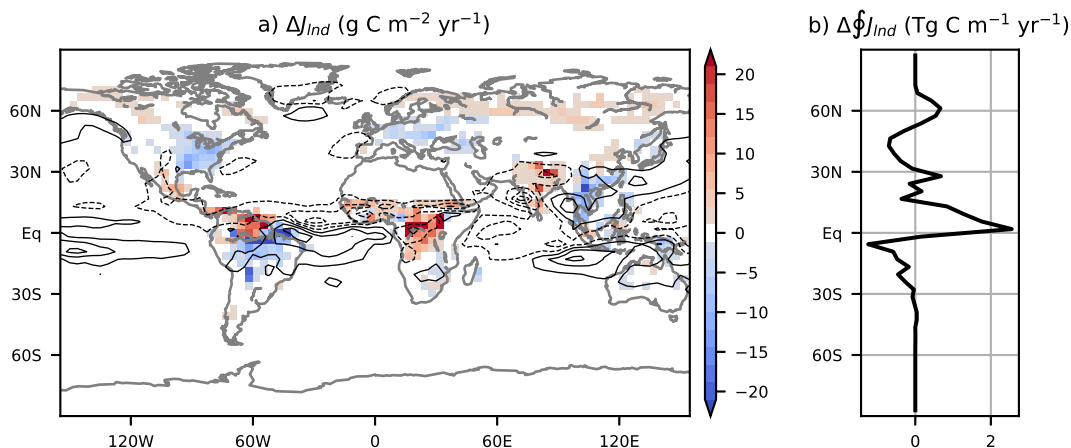


**Figure 6.4:** a: Patterns of CO<sub>2</sub> flux differences from land to atmosphere between THEN and CONT averaged over model year 1100-1300 (positive anomalies denote carbon fluxes from land to atmosphere). Overlaid are contours of precipitation difference (contour interval is  $0.5 \text{ mm d}^{-1}$ , dashed lines denote negative precipitation difference). b: Zonally integrated land-atmosphere CO<sub>2</sub> flux difference.

### 6.3.1 Land-atmosphere fluxes

The 8 Sv reduction in the AMOC strength causes a reduced Atlantic heat transport from the southern to the northern hemisphere resulting in the  $\Delta T$  patterns in Figure 6.1. This, in combination with the insolation change, shifts the latitude band of the tropical SST maximum which is linked to the position of the Intertropical Convergence Zone (ITCZ, e.g. *Broccoli et al., 2006*). Precipitation directly impacts the soil moisture, and precipitation anomalies can therefore lead to changes in the terrestrial carbon stock. As the major release of terrestrial carbon in THEN takes place between 100 and 300 years after the insolation change, we look at the  $\Delta J_{lnd}$  and precipitation anomalies averaged over this time interval. The difference in fluxes is shown in colors in Figure 6.4a. The black contours on top are precipitation anomalies. These show a decrease in tropical precipitation in the northern part of Amazon, India and tropical Africa. These regions correspond to the areas of strongest release of terrestrial carbon. The regions of largest terrestrial carbon uptake, southern Amazon and south east Asia, are associated with increases in precipitation. When the flux differences are integrated zonally (Figure 6.4b), a strong tropical release emerges. This is dominated by the drought over tropical Africa and northern South America. The carbon release of the latter, as well as of India, is partly compensated by the increased uptake in the southern Amazon and south east Asia.

**Table 6.2:** Ocean to atmosphere fluxes in runs averaged over the last hundred years of integration and estimated fluxes from *Gruber et al. (2009)* (all units Pg C yr<sup>-1</sup>)

Case	90°S-44°S	44°S-18°S	18°S-18°N	18°N-49°N	49°N-90°N	Total
CONT	0.142	-0.437	1.053	-0.496	-0.224	0.038
THEN	0.089	-0.472	1.107	-0.495	-0.180	0.049
Gruber	0.4	-0.7	0.9	-0.5	-0.1	0.0

### 6.3.2 Ocean-atmosphere fluxes

The spatial patterns and zonal integral of ocean-atmosphere fluxes in CONT at the end of simulation are shown in Figure 6.5a and b, respectively. Table 6.2 lists the zonally integrated fluxes in the two simulations as well as inverse estimates of the present day natural fluxes of carbon (*Gruber et al., 2009*). Comparing the latter to the fluxes in CONT shows that there is an overall agreement between the two, but discrepancies occur in the extra-tropical southern hemisphere, characterized by less outgassing south of 44°S and less uptake between 44°S and 18°S in CONT compared to estimates. We note that the net southern hemisphere outgassing and uptake compare well, and that the discrepancies are related to a known equatorward shift of the southern hemisphere westerlies in CONT, which affects the latitude of upwelling and outgassing (*Shields et al., 2012*). Tropical outgassing is slightly larger in CONT, and uptake equally larger in the northern high latitudes. Globally, a small net outgassing takes place in CONT.

The large reorganization of the ocean circulation associated with the AMOC collapse leads to changes in carbon fluxes between THEN and CONT,  $\Delta J_{ocn}$ , shown in Figure 6.5c,d. When comparing fluxes between the two simulations we note that if not specified, outgassing (red in Figure 6.5c) may refer to either increased outgassing or reduced uptake in THEN, and uptake (blue in Figure 6.5c) refers to reduced outgassing or increased uptake. The differences between THEN and CONT can be summarized as follows: In the northern high latitudes, ocean uptake is reduced in THEN as a result of increased sea ice cover, inhibiting air-sea fluxes of carbon. In the northern mid-latitudes, a near cancellation between flux anomalies occur between increased carbon uptake in the major current systems of the Kuroshiro and the Gulf Stream and increased outgassing in the mid-latitude Atlantic. The Tropics are characterized by small changes, leading to an overall increase in outgassing, in particular related to an overall small increase in Indian Ocean and west Pacific outgassing. The southern mid-latitudes experience an

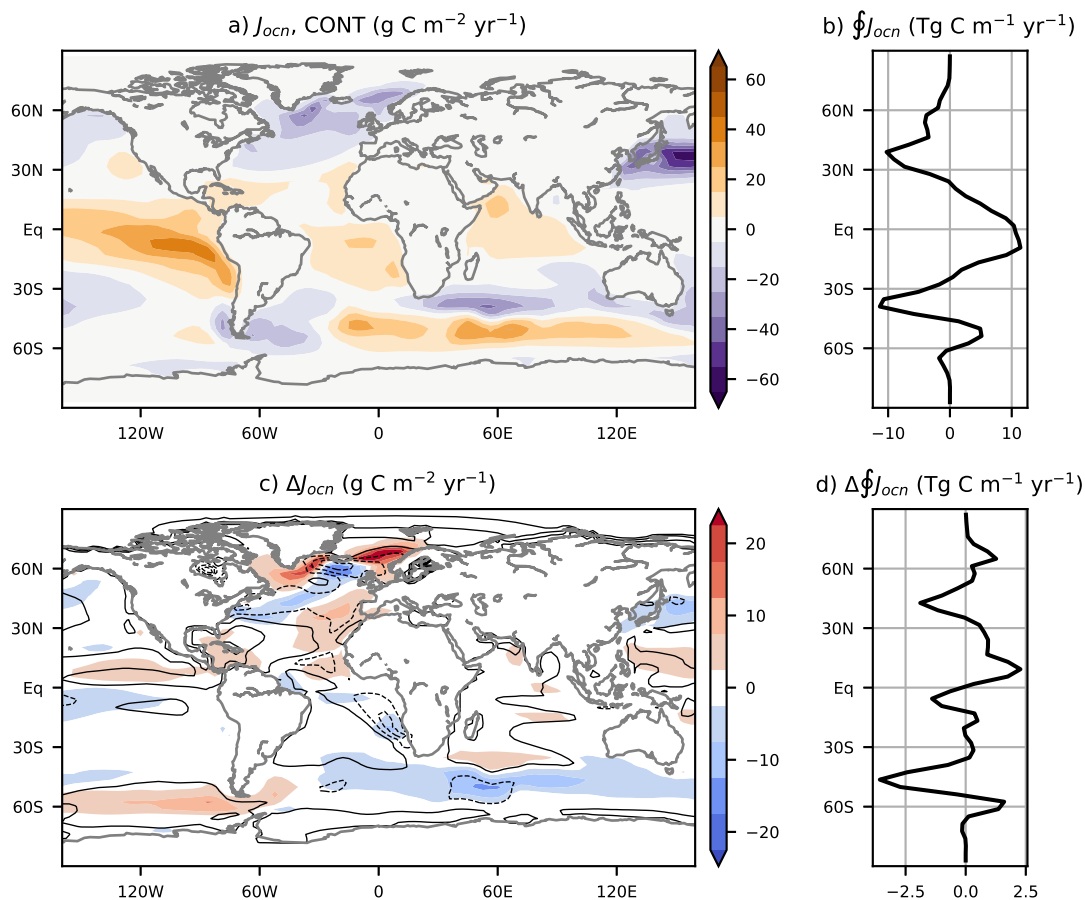


**Figure 6.5:** a: Ocean-atmosphere fluxes of CO<sub>2</sub> (positive is outgassing) in CONT. b: Zonally integrated ocean-atmosphere CO<sub>2</sub> flux for CONT. c: Difference in surface fluxes between THEN and CONT. Overlaid are contours of the DIC difference averaged over the upper 150 m, with contour interval of 20 mmol m<sup>-3</sup> (solid contours denote increases in DIC). d: Zonally integrated ocean-atmosphere CO<sub>2</sub> flux difference.

increase in ocean uptake of carbon in the southern Pacific, partly compensated by a decreased uptake of carbon in the southern Indian Ocean. Finally, the net outgassing south of 44°S is reduced by more than one third.

As seen in previous studies (e.g. [Jochum et al., 2010](#)), the changes to air-sea fluxes of carbon is a patchwork of regional responses. In order to identify the important processes and regions we integrate the flux difference between THEN and CONT over different basins over time. We define the Southern Ocean as the ocean south of the latitude of the Cape of Good Hope, and the Atlantic includes the Mediterranean and high latitude basins. Due to compensating flux differences we integrate the Indo-Pacific as one basin. The resulting net fluxes of carbon at the end of the simulations are shown in Figure 6.6. The global integral

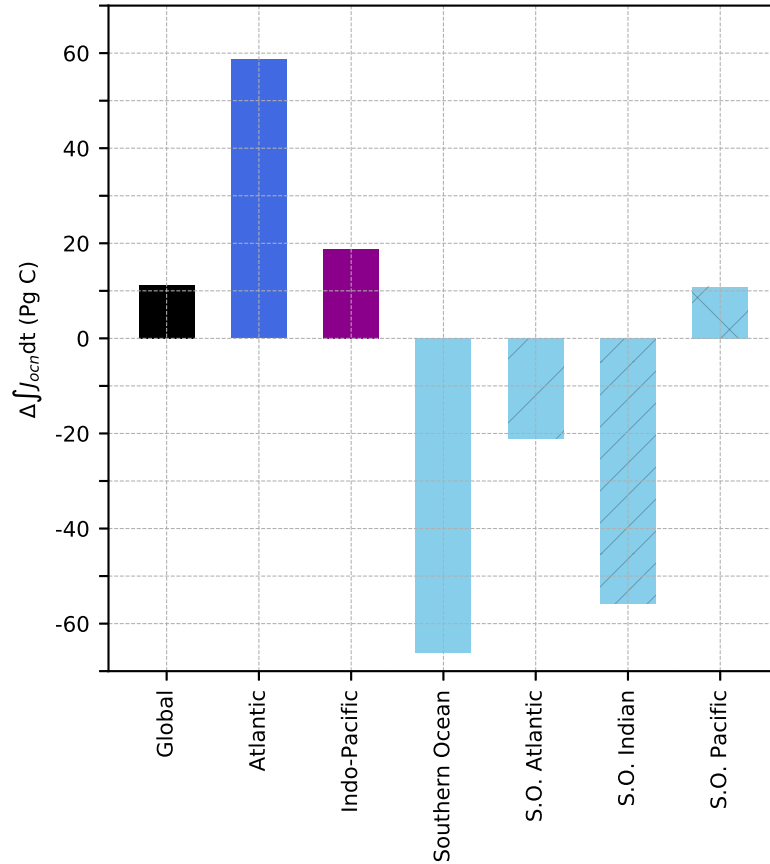


**Figure 6.6:** Difference in integrated fluxes from the ocean to the atmosphere (Pg C) separated into Global, Atlantic (including the Mediterranean and northern hemisphere high latitude basins), Indo-Pacific and Southern Ocean (defined as the ocean south of the latitude of the Cape of Good Hope). The Southern Ocean flux is the sum of the Atlantic (70°W-25°E), Indian (25°E-140°E) and Pacific (140°E-290°E) sectors (hatched light blue bars on the right).

yields a net flux of carbon from the ocean to the atmosphere in THEN of 11.3 Pg C compared to CONT. This flux is a sum of reduced uptake in the Atlantic and Indo-Pacific, largely compensated by a reduced outgassing in the Southern Ocean. As the Southern Ocean generally acts to lower atmospheric CO<sub>2</sub>, contrary to existing hypotheses (*Anderson and Carr, 2010*), we will first investigate the reduced Southern Ocean outgassing, followed by the Atlantic and Indo-Pacific outgassing.

As Figure 6.5c shows that the separate regions of the Southern Ocean reacts differently to the changed forcing, we separate the integrated flux in the Southern Ocean into the Atlantic (70°W-25°E), Indian (25°E-140°E) and Pacific (140°E-290°E) sectors, respectively (Figure 6.6). It is evident that the reduced outgassing

in THEN is dominated by the Atlantic and Indian sectors, where outgassing of carbon from upwelled waters is reduced greatly (as also seen in Figure 6.5c), whereas the Pacific sector outgasses carbon of similar magnitude as the net global response.

In order to explain the reduced outgassing in the Atlantic and Indian sector of the Southern Ocean we plot contours the difference in DIC concentrations averaged over the euphotic layer (the upper 150m) over  $\Delta J_{ocn}$  in Figure 6.5c. This shows that the upwelled waters in the Atlantic and particularly Indian sector are depleted in DIC in THEN. The origin of this DIC depletion can be further illuminated by looking at the vertical structure of DIC in the Atlantic shown in Figure 6.7a for CONT and the difference between THEN and CONT seen in Figure 6.7c. DIC accumulates in the northern deep Atlantic in THEN, while south Atlantic intermediate waters get depleted in DIC. The DIC-depleted waters are entrained in the upwelling waters of the Atlantic and Indian sector of the Southern Ocean, leading to reduced concentration of  $\text{CO}_2$  in the upwelled waters. Simultaneously,  $\text{pCO}_2$  is increasing in THEN, leading to a decreased air-sea difference and as a result reduced outgassing in the Atlantic and Indian sector of the Southern Ocean.

The loss of carbon in the upper ocean (Figure 6.7a) is a global feature. Using apparent oxygen utilization,  $AOU = \text{O}_{2\text{sat}} - \text{O}_2$ , where  $\text{O}_{2\text{sat}}$  is the saturated  $\text{O}_2$  concentration calculated from temperature and salinity, the remineralized, soft-tissue component,  $C_{\text{soft}}$ , of the total DIC is commonly estimated through the relation (see e.g. [Lauderdale et al., 2013](#); [Ödalen et al., 2018](#)):

$$C_{\text{soft}} = r_{\text{C:O}_2} AOU. \quad (6.4)$$

With a stoichiometric ratio  $r_{\text{C:O}_2} = 117/170$  ([Anderson and Sarmiento, 1994](#)) one finds that the reduced upper and intermediate water column DIC is primarily lost as soft-tissue carbon, with a loss of almost 10% in the upper 1 km (not shown). The deep Atlantic DIC accumulation is also dominated by increased soft-tissue carbon from reduced ventilation. Due to disequilibrium effects, Eq. 6.4 overestimates  $C_{\text{soft}}$  in high latitude and deep waters ([Ito et al., 2004](#)). With a total outgassing difference is only 11.3 Pg between THEN and CONT, these uncertainties blur any marine carbon inventory analysis.

The East Pacific sector of the Southern Ocean, where an increase in oceanic outgassing to the atmosphere occurs, is characterized by the largest southern hemispheric warming (Figure 6.1) related to a reduced sea ice cover. The increased air-sea interaction from the reduced sea ice cover (as proposed by [Stephens and](#)

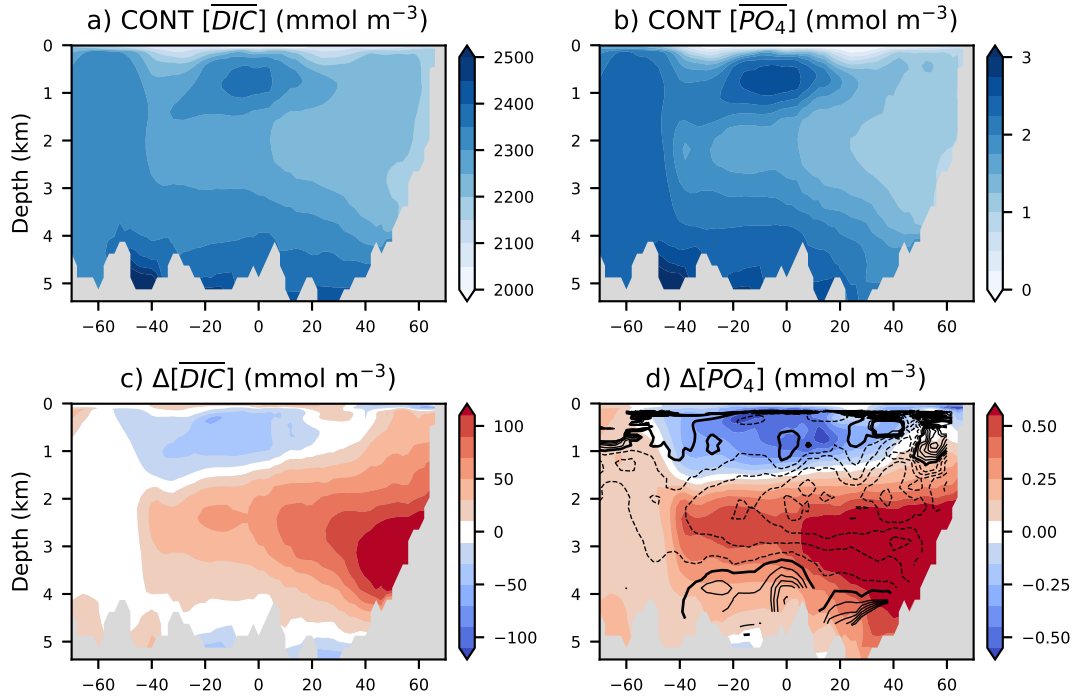


**Figure 6.7:** a: Average DIC concentration in the Atlantic and Southern Ocean Atlantic sector in CONT ( $\text{mmol m}^{-3}$ ). b: Same as (a) but for  $\text{PO}_4$  concentrations ( $\text{mmol m}^{-3}$ ). c: Difference in DIC concentrations between THEN and CONT ( $\text{mmol m}^{-3}$ ). d: Difference in  $\text{PO}_4$  concentrations between THEN and CONT ( $\text{mmol m}^{-3}$ ). Overlaid are meridionally smoothed contours of relative diffusivity in percent, contour interval 15%. Dashed contours indicate decreased diffusivities in CONT, highlighted contour is the 100% contour.

*Keeling, 2000*) in combination with increased upwelling from a strengthening of the wind stress (see also *Lee et al., 2011*) leads to a stronger outgassing in this sector of the Southern Ocean. Thus, while the Southern Ocean as a whole acts as a sink for atmospheric  $\text{CO}_2$ , the increased ventilation in the Pacific sector cannot be neglected as a source for atmospheric carbon.

The increased outgassing from the Atlantic is a factor of 5 larger than the outgassing from the Pacific sector of the Southern Ocean. While the flux of carbon to the atmosphere is in part caused by the larger sea ice cover related to the shut-down of the overturning, inhibiting air-sea fluxes of carbon, the increase in North Atlantic stratification also reduces the depth of the winter mixed layer, which replenishes surface water nutrients. This leads to a decrease in the biological activity of the Atlantic (*Schmittner, 2005*). Figure 6.7b shows the average  $\text{PO}_4$  concentration of the Atlantic and the Atlantic section of the Southern Ocean ( $60^\circ\text{W}$ - $16^\circ\text{E}$ ). Figure 6.7d show the difference between THEN and CONT. The AMOC collapse

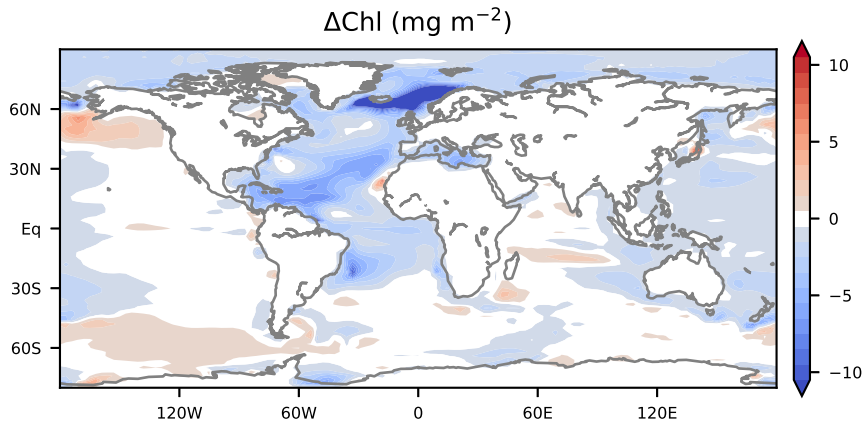


**Figure 6.8:** Difference in total chlorophyll content between THEN and CONT

leads to a depletion in nutrients in surface waters and an increase in deep ocean nutrients (Figure 6.7d). At the same time, the increased deep stratification in the Atlantic caused by intermediate warming (Fig 6.2b) causes a decrease in vertical diffusivity by more than 50% (Figure 6.7d, black contours). This reduces the rate at which nutrients are resupplied to the surface through internal wave breaking. As a result, nutrient supply is limited to coastal upwelling regions which are unaffected by the change in deep stratification. The reorganization of nutrients leads to a reduced biological activity in the Atlantic and leads to a reduction of the rate at which DIC is consumed in the surface waters. The result is a global reduction in primary production of roughly 10%, visualized in Figure 6.8 as a drop in chlorophyll content, in particular in the Atlantic, but also in the Pacific Ocean, in agreement with previous estimates of the marine ecosystem response to a collapse of the AMOC (*Schmittner, 2005*).

## 6.4 Discussion

Previous studies of the response of the carbon cycle to AMOC perturbations have generally found either a terrestrial source and oceanic sink of carbon (*Obata, 2007; Menviel et al., 2008; Bozbiyik et al., 2011*) or an oceanic source and terrestrial sink of carbon (*Schmittner and Galbraith, 2008; Bouttes et al., 2012*). A key result presented in the previous section is the two-timescale response of the Earth system to the AMOC collapse resulting in contributions of increased  $p\text{CO}_2$  by both climate components. Recent measurements from Taylor Glacier in Antarctica show that  $p\text{CO}_2$  rose rapidly within a few centuries in phase with increased methane

concentrations and a decrease in atmospheric  $\delta^{13}\text{C}$  during MIS3 stadials, indicating an organic source of carbon (*Bauska et al., 2018*). This supports the idea of a tropical, terrestrial release of carbon related to a shift in precipitation associated with the ITCZ as seen in the present simulations. We note that the insolation forcing in the present setup not only triggers an AMOC collapse, but also in itself affects the tropical SST maximum, which could amplify or dampen the tropical precipitation response to the overturning weakening.

While the rapid carbon release can account for several ppmv of the increase during stadials, it is not enough to account for all stadial  $\text{pCO}_2$  increase observed in ice cores (*Ahn and Brook, 2014*). The oceanic release takes centuries to start because outgassing is partly compensated by the rapid terrestrial release of carbon at the beginning of the perturbation. Once the terrestrial release ceases, oceanic outgassing continues and the terrestrial biosphere starts to act as a carbon sink. While the initial response resembles that of *Bozbiyik et al. (2011)* who used an older version of the same model, we note that their simulations only lasted 300 years, which we find is too short to identify the oceanic carbon flux response.

While the applied insolation forcing is abrupt, and a realistic, gradual transition could lead to a different model response, the climate and carbon cycle response of the present stimulations is still illuminating to explore as drastic perturbations to the insolation have occurred in the past (*Pausata et al., 2015*).

The present results find that after one millennium, in addition to the fast terrestrial release of carbon, the ocean accounts for an equal but more gradual release of  $\text{CO}_2$  due to a combination of reduced biological activity, particularly in the Atlantic, and deep ocean ventilation in the Pacific sector of the Southern Ocean. While there is evidence of increased Southern Ocean upwelling during stadials, (*Anderson et al., 2009*), recent ocean sediment  $\delta^{11}\text{B}$  results from the Nordic Seas support the possible release of carbon in the North Atlantic (*Ezat et al., 2017*).

A reduced biological pump caused by an AMOC collapse in response to freshwater forcing in the North Atlantic was found by *Schmittner and Galbraith (2008)* to dominate the outgassing of  $\text{CO}_2$  to the atmosphere during stadials, with a minor release from boreal vegetation. We also find large reductions in air-sea fluxes of carbon due to a reduced marine primary production. However, the present simulations differ in two important ways from the results of *Schmittner and Galbraith (2008)*.

First, the major release of terrestrial carbon in our model occurs in the tropics

rather than in the boreal regions, related to a shift in the ITCZ. The lack of a tropical response in the results of *Schmittner and Galbraith (2008)* is a direct result of the missing wind and precipitation changes in their energy-balance atmospheric model. *Schmittner and Lund (2015)* analyzed the sensitivity of the terrestrial carbon fluxes to a southward migration of the ITCZ and found a similar rapid release of terrestrial carbon to the atmosphere as seen in the present simulations. The missing boreal signal in the present results, on the other hand, may be related to the lack of dynamic vegetation in the land component. *Scholze et al. (2003)*, using a dynamic vegetation model, found a large release of carbon in the northern hemisphere in response to an AMOC collapse, in part attributed to plant functional types being replaced by less productive types. Our simulations lack such mechanisms. As a consequence, the terrestrial release of carbon in response to an AMOC collapse could be even larger than shown here. However, *Obata (2007)* noted that the magnitude of terrestrial release of carbon depends strongly on the background climate prior to AMOC collapses. The terrestrial carbon inventory during the glacial was smaller than pre-industrial values. As our simulations are carried out using a pre-industrial configuration, the terrestrial carbon stock may be smaller using glacial boundary conditions. Similarly, the ocean carbon inventory was likely larger during the last glacial (see e.g. *Sigman and Boyle, 2000*), and thus the ocean outgassing in response to an AMOC weakening could be different in magnitude under such boundary conditions. However, we note that  $p\text{CO}_2$  in CONT is lower than pre-industrial, and conversely the marine carbon inventory larger. The weak AMOC in CONT, a bias in the coarse resolution CESM (*Shields et al., 2012*), also influences carbon sequestration through both solubility and particularly biology (*Ödalen et al., 2018*).

The second difference, with respect to *Schmittner and Galbraith (2008)*, is that the biological activity of the Atlantic is reduced in our simulations not only because of the shallower winter mixed layer due to increased surface stratification, but also due to the decreased mixing resulting from the increased ocean stratification. While their model includes a tidal mixing parameterization, such dynamical feedback is damped in models with fixed background diffusivities and underlines the importance of improving understanding of forcing mechanisms of the internal wave field. In the present setup we use a fixed energy supply from the conversion of barotropic tides to internal waves and thus only find changes in mixing from changes in stratification. However, large changes occur in the surface wind stress due to the collapsing AMOC, which could alter the amount of energy entering the

internal wave field from mesoscale eddy forcing or near-inertial waves. Furthermore, changing energy sources and stratification affects the overturning circulation (e.g. [Schmittner et al., 2015](#)). While the relative importance of the decreased diffusivities on the reduced biological activity in the present simulations is likely second order compared to the reduced deep winter mixing that replenishes surface waters with nutrients, it highlights the need for careful treatment of the vertical mixing in ocean models.

We note that changes in wind patterns also impact the ocean biogeochemistry through dust and iron supply. The present model uses a fixed climatology of dust and iron fluxes, and as a result has no changes in the iron supply due to the wind stress changes resulting from the AMOC collapse.

While the AMOC collapse results in increasing temperatures in the intermediate ocean (Fig. 6.2a), an effect on  $p\text{CO}_2$  from a reduced solubility pump can be present in our simulations. However, the global surface temperature difference is only 0.1 K. While this reduces the ocean solubility, it can account for only a small part of the observed  $p\text{CO}_2$  increase (e.g. [Omta et al., 2011](#)).

Several studies suggest increased ventilation in the Southern Ocean as a mechanism for increased  $p\text{CO}_2$  during stadials ([Anderson et al., 2009](#); [Menviel et al., 2015](#)). This argument is partly based on increased opal burial, which indicates increased export production, also observed in the present simulations, most notably in the Pacific sector (Figure 6.8). Sediment and coral radiocarbon in the Southern Ocean also indicate increased ventilation during Heinrich stadial 1, coincident with an increase in atmospheric  $p\text{CO}_2$  ([Skinner et al., 2010](#); [Burke and Robinson, 2012](#)). The present simulations show increased Southern Ocean ventilation rates in agreement with these records (not shown). While the Pacific sector releases more carbon due to a decrease in sea ice cover, increased surface DIC and increased AABW formation in the Ross Sea, Southern Ocean outgassing is overall reduced due to the decrease in DIC concentrations of the upwelling waters in the Atlantic and Indian sector that entrain intermediate waters depleted in DIC.

The Pacific sector of the Southern Ocean, in agreement with previous studies, ventilates the Pacific, contributing to the net release of carbon ([Menviel et al., 2014](#)). However, we highlight that flux anomalies in the Southern Ocean are non-uniform, and that local outgassing is influenced by remote processes. In the present simulation, reduced DIC concentrations in the upwelled waters in the Atlantic and Indian sector lead to decreased outgassing. To fully understand the role of the Southern Ocean on outgassing, further understanding of the spatial heterogeneity

in carbon fluxes during the last glacial is needed.

As the outgassing from the Atlantic, Indo-Pacific and Pacific sector of the Southern Ocean is largely compensated by reduced outgassing in the Atlantic and Indian sector of Southern Ocean, the present simulations find that a combination of tropical terrestrial release of carbon, reduced oceanic primary production and increased ventilation in the Pacific sector of the Southern Ocean contribute to rising atmospheric  $p\text{CO}_2$  in response to a strong weakening of the AMOC. Since the overturning likely weakened during stadials (*Böhm et al., 2015; Henry et al., 2016*), we speculate that these mechanisms could be important for the  $p\text{CO}_2$  increase during stadials.

## 6.5 Summary and conclusions

We simulate the response of the carbon cycle in an Earth System Model due to a collapse of the overturning over one thousand years. The main results can be summarized as follows:

- A simulated collapse of the AMOC leads to a two-timescale response in the carbon cycle, consisting of a rapid terrestrial release and a slow, oceanic outgassing of carbon.
- The terrestrial release is attributed to changes in precipitation in the tropics related to shifts in the ITCZ over South America and Asia, as well as drought over Africa.
- The ocean outgassing is attributed to a combination of a shallower winter mixed layer depth in the Atlantic and reduced diapycnal mixing, both of which limit the nutrient supply to the surface waters. This, in turn, reduces biological activity and associated carbon uptake globally.
- The Southern Ocean outgassing is overall reduced as upwelling waters in the Atlantic and Indian sector of the Southern Ocean are depleted in DIC, leading to regionally reduced outgassing, whereas the Pacific sector outgasses more carbon to the atmosphere.

## Acknowledgments

This study was supported by The Danish Council for Independent Research, Natural Sciences, 4002-00397. Simulations were done with support from the Danish Centre for Climate Computing at the University of Copenhagen. JBP was supported by the European Research Council under the European Communitys Seventh Framework Programme (FP7/2007e2013)/ERC grant agreement 610055 as part of the ice2ice project.

Ocean and atmospheric model output means are available online at [https://sid.erda.dk/wsgi-bin/lis.py?share\\_id=h92uPoX96j](https://sid.erda.dk/wsgi-bin/lis.py?share_id=h92uPoX96j). Other output fields are available from the lead author upon request.

## Part III

# Outlook and Discussion



# Chapter 7

## Outlook

Chapter 6 investigated the carbon cycle response to an AMOC collapse using the IDEMIX scheme for vertical mixing. This circulation change induced an increase in global ocean stratification, particularly in the Atlantic, where stratification doubled. This resulted in up to a halving of the diapycnal diffusivity, with consequences for the nutrient supply to the euphotic zone and thus productivity and export production.

A collapse of the Atlantic overturning results in a drastic change of the water-masses in the ocean interior. As pointed out in the introduction, changes in the ocean diffusivity can arise from either changes in the energy provided for lifting dense water parcels through mixing, or from local changes in the stratification. Therefore, some of these questions can be explored further.

In this chapter, preliminary results where the mixing is altered either through stratification changes or energy forcing are presented. Focus is on the marine carbon cycle, but each single simulation of this chapter could be discussed much further.

**Table 7.1:** Overview of model runs with different orbital configurations.

Case	pCO <sub>2</sub> [ppmv]	AMOC [Sv]	$\epsilon_{IW}$ [TW]	Exp. P. [PgC yr <sup>-1</sup> ]	Age [yr]
STLA	278.2	14.4	-	8.32	526
70KA_ST	279.0	14.3	-	8.35	510
103KA_ST	285.6	14.3	-	8.36	513
113KA_ST	276.7	13.3	-	8.31	512
CONT	253.0	12.6	0.95	5.72	561
70KA_ID	254.3	11.8	0.94	5.83	542
103KA_ID	257.9	13.0	0.94	5.83	547
113KA_ID	262.1	4.5	0.94	5.08	571

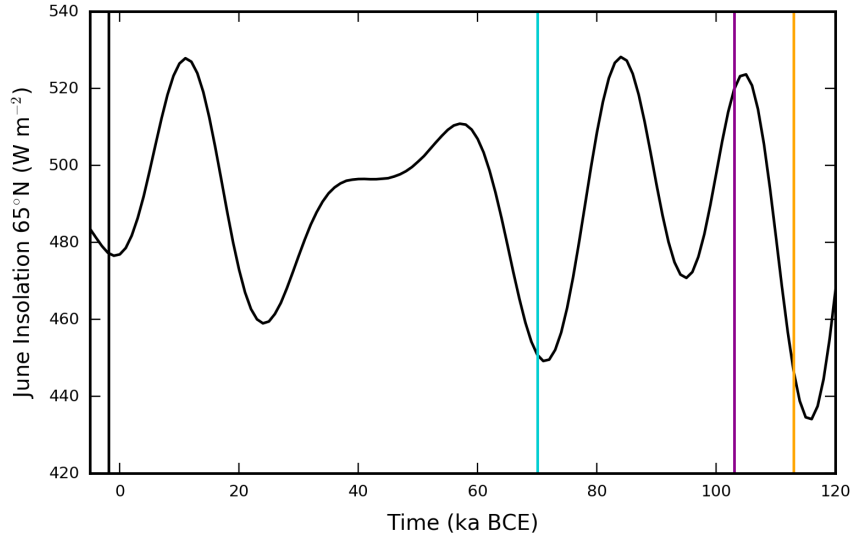


**Figure 7.1:** Numerically estimated June insolation at 65°N (*Laskar et al., 2004*). The vertical lines indicate the four chosen orbital configurations for the simulations 113KA (yellow), 103KA (magenta), 70KA (blue) and CONT (black).

Section 7.1 revolves around changes in mixing resulting from changes in insolation, as in the previous chapter. In Section 7.2 the energy available for mixing is increased in two ways, in one simulation by doubling the tidal energy input to IDEMIX, in the other the internal wave energy is forced by both tides and local dissipation of mesoscale eddy kinetic energy. Section 7.3 briefly discusses the nature of the overturning collapse discussed in the previous chapter.

## 7.1 Insolation and Mixing

The concept of the Milankovitch theory is that summer insolation at high latitude, determined by Earth’s orbit around the sun, drives ice sheet expansion or retraction. The June insolation at 65°N over the last glacial cycle calculated by *Laskar et al. (2004)* is plotted in Fig. 7.1. As in the previous chapter, the coarse resolution CESM ver. 1.2 is used to investigate changes in ocean circulation and carbon storage induced by changes in insolation. The model is run in the T31x3 configuration with active biogeochemistry (*Shields et al., 2012; Lindsay et al., 2014*). Each simulation is run for 1000 years and results are shown for the last 100 model years. An overview is given in Table 7.1. Note that these results are preliminary, and that simulations are not equilibrated after the 1000 years integration time.

The model is forced with four different insolutions: Pre-industrial (1850 CE,

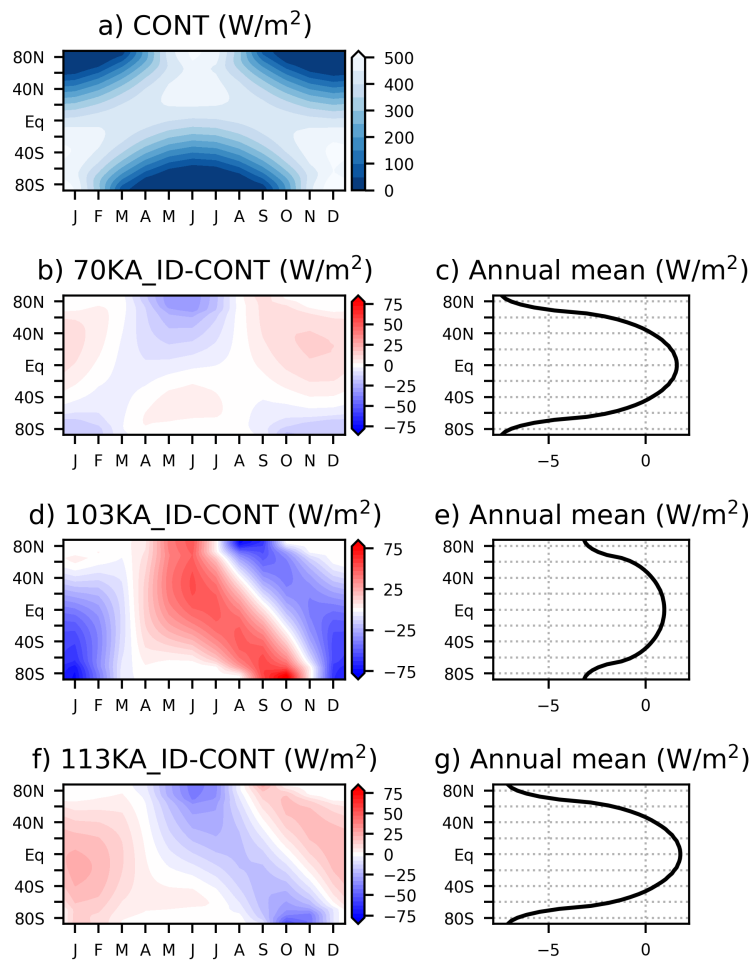


**Figure 7.2:** a: Incoming solar radiation in CONT. b: Difference in insolation between 70KA\_ID and CONT. c: Annually averaged solar insolation difference, 70KA\_ID -CONT. d and e: Same as b and c but for 103KA\_ID -CONT. f and g: Same but for 113KA\_ID -CONT.

vertical black line in Fig. 7.1), 70 ka BCE (blue), 103 ka BCE (magenta) and 113 ka BCE (yellow), and is run for each orbital configuration using both IDEMIX and the *St. Laurent et al. (2002)* parameterization. The pre-industrial simulation using IDEMIX will be referred to as CONT, whereas STLA denotes the pre-industrial simulation using *St. Laurent et al. (2002)*. The choice of 113 ka BCE is the same as the simulation THEN discussed in Chapter 6. This choice represents a glacial inception scenario, where June insolation at 65°N is low (*Jochum et al., 2010, 2012*). Due to the collapse of the overturning resulting from this choice of insolation, a 70 ka orbital configuration was chosen to force the model in a similar fashion as 113 ka of smaller magnitude, resulting in a climate state with an active AMOC for both mixing schemes. 103 ka orbital configuration was chosen for its large summer

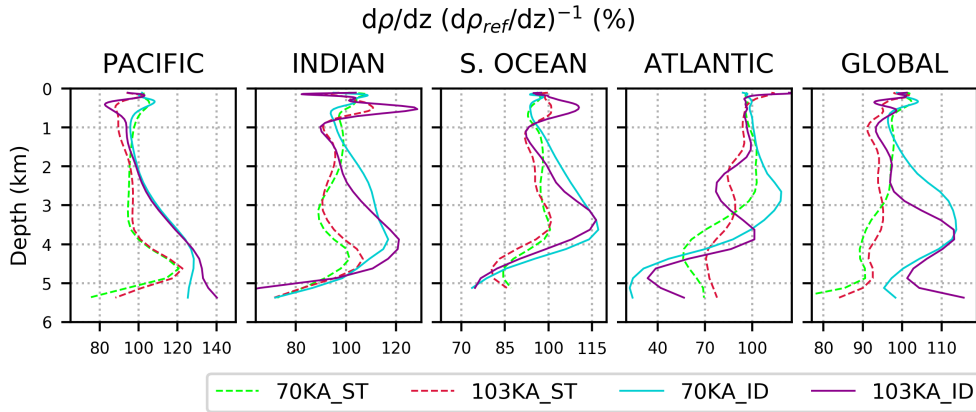


**Figure 7.3:** Stratification relative to the pre-industrial control simulation for different insulations for IDEMIX (*Olbers and Eden, 2013*, solid lines) and *St. Laurent et al. (2002)* (dashed).

insolation.

The insolation seasonal cycle of CONT is plotted in Fig. 7.2 along with the differences in insolation for the three other orbital configurations for the IDEMIX simulations (they are identical for *St. Laurent et al.*). The annual mean insolation difference at each latitude is very similar for 113KA\_ID and 70KA\_ID (Fig. 7.2c,g), but with smaller seasonal variation between 70KA\_ID and CONT than 113KA\_ID and CONT (Fig. 7.2b,f). While northern hemisphere June insolation is higher in 103KA\_ID, the annual mean insolation at high latitudes is reduced compared to CONT (Fig. 7.2d,e).

The hypothesis that is tested is that changes in insolation impact the circulation of the ocean and thereby stratification, which in turn has impact on the global carbon cycle. As this is work in progress, the primary goal of this section is to quantify the changes in ocean stratification, their impact on mixing and the carbon cycle with a focus on similarities and differences between using one vertical mixing scheme or another.

### 7.1.1 Stratification and Mixing

The applied insolation forcing impacts the heat and salt budgets of the ocean basins, including regions of deepwater formation. As a result, the ocean stratification is different on regional and global scales depending on insolation. Because of the AMOC collapse in 113KA\_ID, rendering it difficult to compare with the run using the *St. Laurent et al. (2002)* mixing scheme, we focus on the runs using 70

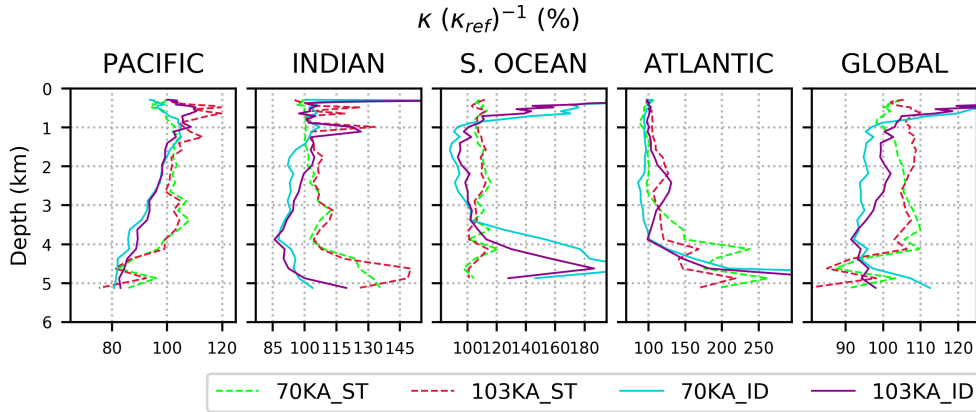


**Figure 7.4:** Same as Fig. 7.3 but for vertical diffusivity.

and 103 ka BCE orbital configurations.

Fig. 7.3 shows the stratification relative to CONT for 70KA\_ID and 103KA\_ID and relative to STLA for 70KA\_ST and 103KA\_ST. For simulations using IDEMIX, stratification changes are mostly within 20% of CONT, except for the upper ocean and the very deepest ocean, particularly the Atlantic. Stratification changes in simulations using *St. Laurent et al. (2002)* are generally weaker, with less than 10% reductions in stratification in the Pacific, Indian and Southern Ocean above 4 km depth. Globally, stratification is decreased throughout most of the water column in 70KA\_ST and 103KA\_ST, compared to increased stratification below 3 km and decreased stratification above in 70KA\_ID and 103KA\_ID. Despite the different nature of the insolation changes, the deep stratification changes are very similar for simulations with the same vertical mixing parameterization, except for the upper ocean and the Atlantic between 2 and 4 km depth. The upper ocean stratification changes are similar for simulations of same forcing rather than with the same mixing parameterization. Thus, upper ocean stratification changes consistently to insolation changes, whereas there is no direct link between the insolation and the deep ocean stratification. The deep ocean stratification depends on the rate of deep water formation at high latitudes, in particular Antarctic Bottom Water production (AABW), which is larger in both 70KA\_ID and 103KA\_ID compared to CONT, but smaller in 70KA\_ST and 103KA\_ST compared to STLA. Thus, the formation rate of AABW is impacted differently by the insolation changes depending on the choice of mixing parameterization.

AMOC strength is more variable in the simulations using IDEMIX than in simulations using *St. Laurent et al. (2002)*. This indicates that the higher background

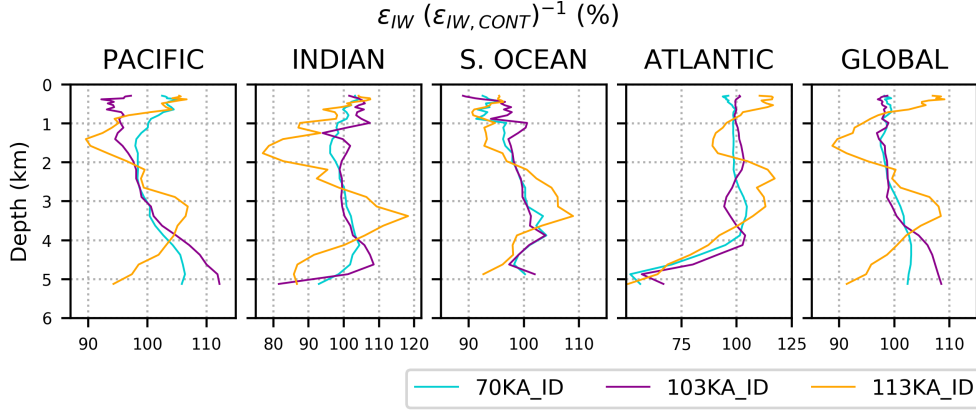


**Figure 7.5:** Relative dissipation rates compared to CONT averaged over the different ocean basins.

diffusivities reduce the sensitivity of the ocean circulation to surface forcing. Note, however, that while IDEMIX is only forced by tidal dissipation to internal waves, these runs may be over-sensitive compared to the real ocean, where estimates of dissipation are larger than the 1 TW used in the present simulations (*Wunsch and Ferrari, 2004*).

Fig. 7.4 shows the corresponding changes in vertical diffusivity arising from the changes in stratification seen in Fig. 7.3. While there is a general relationship between weaker diffusivities and regions of stronger stratifications, simulations using IDEMIX experience large upper ocean increases in diffusivities in the Southern Ocean because of increased AABW formation. Events of AABW formation, while short in time, dominate calculations of mean diffusivities as the diffusivities are increased by several orders of magnitude. It is not obvious if these diffusivities are physical or just a model artifact, as internal waves are not present without a finite stratification.

The vertical mixing in IDEMIX is also affected by changes in the vertical distribution of dissipated internal wave energy, which is in itself a function of the stratification (Eq. 2.41). The dissipation rates relative to CONT are shown in Fig. 7.5 for IDEMIX simulations.

The dissipation rates in 70KA\_ID and 103KA\_ID lie close to CONT, but with a tendency for increased dissipation rates in regions of stronger stratification and vice versa. In the case of the collapsed overturning in 113KA\_ID, a larger fraction of the dissipation of internal wave energy is shifted from the upper 2 km to the deep ocean. This is due to the increased deep stratification which leads to

**Table 7.2:** Carbon pump strengths (in Pg C) and  $\mathcal{P}^*$ . Carbon pumps are listed for pre-industrial simulations, with anomalies for the other simulations.

Case	DIC	$C_{\text{pre}}$	$C_{\text{soft}}$	$C_{\text{hard}}$	$\mathcal{P}^*$
STLA	36495	33597	1918	979	47.4%
70KA_ST	-1.3	+44.1	-42.1	-3.3	46.4 %
103KA_ST	+13.0	+77.7	-54.6	-10.1	46.1%
113KA_ST	-6.2	+25.2	-31.1	-0.3	46.6%
CONT	36690	33556	2088	1046	50.9%
70KA_ID	-0.6	+40.9	-37.4	-4.1	50.0%
103KA_ID	+11.5	+56.6	-36.7	-8.3	50.0%
113KA_ID	+15.9	+7.6	+3.8	+4.5	50.8%

an increase in dissipation rates. The *St. Laurent et al. (2002)* parameterization has a fixed dissipation profile and is thus not responsive to changes in the deep ocean and associated dissipation shifts. Using more dynamical dissipation profiles (*Polzin, 2009*) or scaling the dissipation directly with stratification (*Melet et al., 2016*) are alternative ways to accommodate some of these effects.

### 7.1.2 Carbon Cycle

While the changes in stratification and mixing in general are minor when different orbital forcing is used, it may be important to the overall carbon cycle. The carbon pump strengths are listed in table 7.2 (see Chapter 2.4). In simulations with 70 ka orbital configuration, pCO<sub>2</sub> increases by roughly 1 ppmv, driven by a combination of small terrestrial and oceanic release of carbon. As a result, total ocean DIC is virtually unchanged compared to their pre-industrial counterparts. This is achieved through a compensation between increased pre-formed carbon and decreased soft- and hard-tissue carbon, a result of the small decrease in global ocean age indicative of stronger ocean ventilation (Table 7.1). This is the case regardless of the mixing scheme, with the magnitude of variations in carbon inventory anomalies is marginally larger in simulations using the *St. Laurent et al. (2002)* scheme except for the carbonate pump.

In simulations using 103 ka BCE orbital configuration, the ocean accumulates more carbon than with pre-industrial forcing. This is caused by a release of terrestrial carbon to the atmosphere, which occurs regardless of mixing parameterization. The net difference in carbon uptake is roughly the same between 103KA\_ST and STLA and 103KA\_ID and CONT. The difference in pCO<sub>2</sub> is caused by the differences in terrestrial processes, which depend on the temperature and mois-

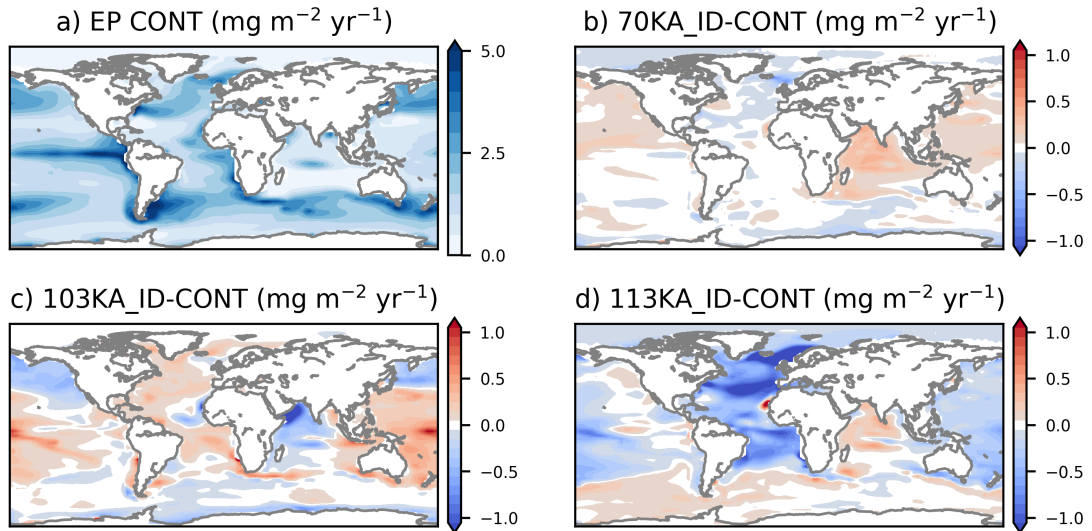


**Figure 7.6:** Export production in CONT (a), and difference between simulations and CONT for 70KA\_ID (b), 103KA\_ID (c) and 113KA\_ID (d).

ture anomalies that are different in the two simulations (See Fig. 4.5). The DIC increase is dominated by preformed carbon, partly compensated by decreases in hard- and soft-tissue carbon caused by stronger ventilation. Variations in the carbon inventory anomalies are larger in simulations using *St. Laurent et al. (2002)* than IDEMIX. This is opposite to the changes in AMOC strength, where the *St. Laurent et al. (2002)* simulations are robust.

The simulations with 113 ka orbital configuration cannot be compared due to the AMOC collapse in 113KA\_ID. However, despite a net flux of carbon from ocean to atmosphere in 113KA\_ID compared to CONT, there is a net increase in DIC. This is a result of the sedimentation parameterization for organic matter and  $\text{CaCO}_3$  which depend on the export production (*Dunne et al., 2007*). As a result, the strength of the seafloor sink of carbon varies in simulations where export production is significantly different. As a result, all pumps appear to increase in strength, although these have different regional scale. For instance, soft tissue carbon is lost in all basins except for the deep Atlantic.

An interesting feature of changing insolation is that the overall export production variations are very small, despite large regional differences, except for the case of 113KA\_ID (where export production is reduced by more than 10%), seen for IDEMIX simulations in Fig. 7.6. The increase in export production is caused by increased surface nutrient concentrations rather than light limitation reduction.

In total, except for the 113 ka forcing simulations, where circulation changes

are too drastic to be compared, the response of the ocean carbon cycle response to insolation forcing is fairly robust to the choice of mixing parameterization, despite the differences in ocean stratification and mixing changes. Instead, ventilation and nutrient utilization put stronger constraints on the carbon cycle. As the AMOC does not collapse in 113KA\_ST the importance of the mixing changes discussed in Chapter 6 cannot be quantified. The small variation in the carbon cycle response in the simulations with different mixing schemes discussed here suggest that the system as a minimum needs a large perturbation beyond insolation forcing in order to trigger a carbon cycle response.

A drawback in these preliminary results is the length of integration, as a 1000 years is too short integration time for the model to equilibrate. As a result, the transient behavior of the model impacts the results presented here. It is not unlikely that it takes longer time to reach equilibrium when the mixing is fully dependent on the stratification, and as a result, more robust results will be obtained for longer integrations. However, the results at hand suggest that the response of the carbon cycle only depends weakly on the choice of mixing scheme, as long as changes in ocean circulation are minor. Another issue is the amount of energy used for mixing in the model, in particular in cases using IDEMIX. Including more energy sources might significantly modify the model simulations, in particular if such energy sources, like dissipation of mesoscale eddies and generation of near-inertial waves, are a function of the climate itself. Thus, much work is needed to establish the full extent and importance of changes in the stratification on mixing and the carbon cycle.

## 7.2 Energy Sources

Including a mesoscale eddy source term in IDEMIX was shown in Chapter 4 to have impact on thermocline mixing and temperature. In this section, a similar experiment with the model coupled to biogeochemistry is performed and the im-

**Table 7.3:** Overview of model experiments where the internal wave energy forcing in IDEMIX is increased.

Case	pCO <sub>2</sub> [ppmv]	AMOC [Sv]	$\epsilon_{IW}$ [TW]	Exp. P. [PgC yr <sup>-1</sup> ]	Age [yr]
CONT	253.0	12.6	0.95	5.72	561
TIDE	252.7	12.5	1.70	5.77	549
IEDDY	264.9	13.4	2.13	7.07	538

pacts on the carbon cycle are discussed. This case will be referred to as IEDDY. Another test on the importance of energy of IDEMIX on the ocean carbon cycle is performed by multiplying the tidal energy source term by a factor of 2, in order to test the importance of increasing tidal dissipation. Deep tidal dissipation rates vary strongly over glacial cycles, with potential huge impact on the ocean circulation (*Wilmes and Green, 2014; Schmittner et al., 2015*). This run is referred to as TIDE. As in the previous section, simulations are run for 1000 years using the coarse resolution CESM ver. 1.2. Analysis is carried out for the last hundred simulation years. In the case of IEDDY, due to numerical instabilities, the mixing was relaxed to the background mixing of *Jochum (2009)* in grid points with 3 or more neighboring land mask points. The mesoscale eddy forcing is locally injected and follows the same implementation as described in Chapter 4.

The model simulations are summarized in Table 7.3. While the globally integrated dissipation (calculated as the integral of  $\epsilon_{IW}$  in Eq. 2.45) is almost doubled in TIDE compared to CONT, changes in AMOC strength, pCO<sub>2</sub> and export production are on the order of 1%. Contrary to that, pCO<sub>2</sub>, AMOC strength and export production increase in IEDDY compared to CONT, along with a more than doubling of dissipation rates. While the dissipation rates are 0.4 TW larger in IEDDY than TIDE, it is interesting to understand why the ocean and carbon cycle behaves radically different in the two cases. To explore this, globally averaged dissipation rates are plotted in Fig. 7.7. While dissipation rates in TIDE are increased throughout the water column compared to CONT, the increased dissipation rates are focused in the upper 1 km in IEDDY.

This localized increase in dissipation, particularly in the thermocline, makes the thermocline more diffuse in IEDDY (see Chapter 4). At the same time it strengthens the AMOC and increases nutrient transport through the thermocline into the euphotic zone, increasing the export production globally. This is seen in Fig. 7.8b and c, where surface nutrient concentrations are increased everywhere except for the Southern Ocean in IEDDY compared to CONT. In particular, surface nutrient concentrations of the Indian Ocean more than double, resulting in a large increase in export production. On the other hand, export production and surface nutrient concentrations vary little in TIDE compared to CONT, resulting in a modest 1% increase in export production, despite an almost doubling of global dissipation rates.

While export production is greatly increased, the soft tissue pump of the ocean is greatly reduced due to increased ventilation of the global ocean. This decrease in

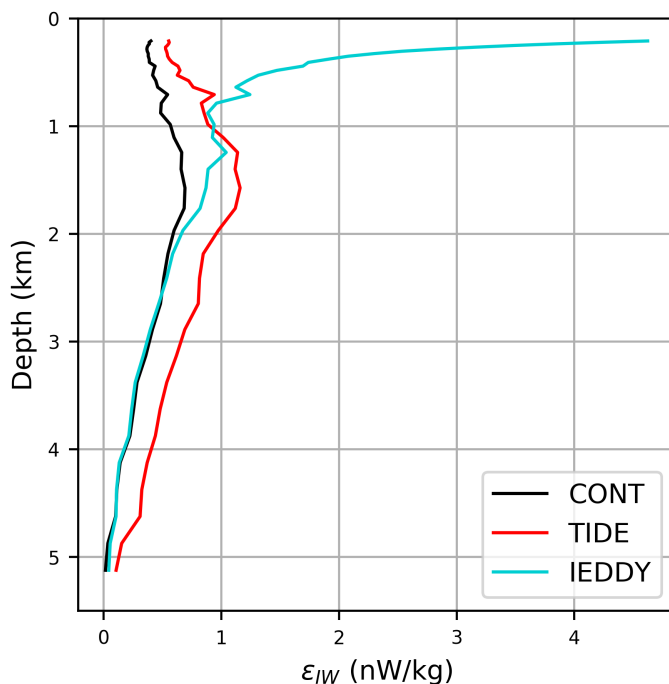


**Figure 7.7:** Globally averaged dissipation rate profiles for CONT (black), TIDE (red) and IEDDY (blue).

soft (and hard) tissue carbon is compensated by an increase in preformed carbon. As ocean temperature is warmer in IEDDY, reducing the solubility, this is caused by an increase in disequilibrium carbon inventory.

Due to the effects of mixing on surface temperatures, the terrestrial carbon inventory is increased considerably in IEDDY. Thus, the 11.9 ppmv increase in  $p\text{CO}_2$  is a result of less net ocean uptake of carbon compared to both CONT, whereas the weak decrease of 0.3 ppmv in TIDE is a result of a slightly greater ocean uptake of carbon than CONT.

While these simulations are preliminary, and while the present implementation of a mesoscale eddy source term to IDEMIX is questionable, the above results suggest that it is not necessarily the magnitude of dissipation of internal wave energy that is important with regards to the carbon cycle. Rather, the vertical (and horizontal) distribution of the dissipated energy appears to be of greater importance. In particular, these preliminary results suggest that upper ocean internal wave energy sources, such as mesoscale eddies and near-inertial waves, may play a crucial role in the marine carbon cycle and ecosystem.

This could lead to important consequences for the climate system. In an oceanographic framework it means that a change in the mesoscale eddy or near-

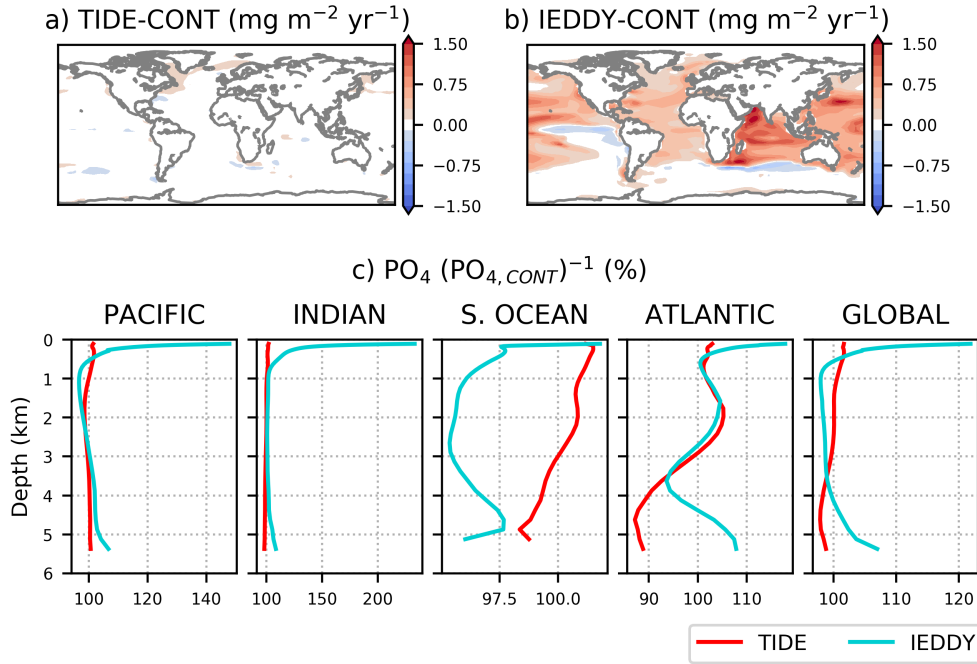


**Figure 7.8:** **a:** Export production difference between TIDE and CONT. **b:** Same as **(a)** but for IEDDY and CONT. **c:** PO<sub>4</sub><sup>3-</sup> concentrations of the major ocean basins relative to CONT for TIDE (red) and IEDDY (blue).

inertial wave forcing of the internal wave field could be more important to nutrient cycling and ocean ventilation than an increase in tidal forcing (or vice versa). This requires models of past climate to more carefully estimate energy fluxes from tides, winds and eddies as functions of the simulated model variables, rather than using fixed energy sources from e.g. pre-industrial simulations. Tidal input to internal waves was stronger during the last glacial, but the overturning and ventilation was likely weaker (*Jansen, 2016; Muglia et al., 2018*). This apparent discrepancy could be explained by a reduced wind input to internal waves, from e.g. reduced atmospheric storminess (*Li and Battisti, 2008*). It also suggests that adding or removing energy uniformly from the background diffusivities might not be an adequate representation of paleo mixing (*Schmittner et al., 2015; Jansen, 2016; Melet et al., 2016*).

With regards to internal wave theory it puts strong demands on the understanding and modeling of internal wave propagation and dissipation. It is crucial that internal wave propagation and dissipation is represented correctly in parameterizations such as IDEMIX. High resolution simulations on super computers are needed in order to compare the internal wave and dissipation fields of parameter-



as function of June insolation at  $65^{\circ}\text{N}$  for the simulations mentioned in this chapter, and Fig. 7.9b shows the export as function of June temperatures between  $65$  and  $70^{\circ}\text{N}$  and  $30$  and  $0^{\circ}\text{W}$ . Black marks are simulations using IDEMIX, magenta marks use *St. Laurent et al. (2002)*. Red and blue marks are TIDE and IEDDY, respectively.

In general (excluding case 113KA\_ID where the overturning collapses) there is relationship between summer insolation and winter sea ice export into the North Atlantic, however, there is an offset between simulations using different mixing parameterizations (and energy, red and blue squares) and the amount of sea ice export, where simulations using IDEMIX tend to have a larger winter sea ice export than simulations using *St. Laurent et al. (2002)*. Fig. 7.9b reveals that this difference is related to the overall surface temperatures. Colder summer temperatures lead to increased winter sea ice export in a near linear relationship, except for 113KA\_ID, where the sea ice edge extends far into the North Atlantic due to the overturning collapse, and sea ice velocities as a result decrease drastically, limiting the linear relationship to apply only given a narrow range of climate states.

It is tempting to speculate that, by modifying surface temperatures in the North Atlantic and Nordic Sea region, the orbital configuration might play a role in the occurrence and duration of DO cycles through its impact on sea ice export to the North Atlantic. However, as discussed in *Jochum et al. (2012)*, finer resolution simulations have a different response in the North Atlantic freshwater budget, in part caused by a reduction of liquid freshwater export through the Baffin Bay to the North Atlantic. Therefore, while the idea of an insolation control on the North Atlantic stratification and stability is intriguing, it is most likely a model artifact. More simulations of higher resolution than presented here are needed to identify any relationship between insolation and North Atlantic surface stratification.

# Chapter 8

## Summary and Conclusion

An energetically consistent, globally stratification-dependent parameterization for vertical mixing in the ocean induced by the breaking of internal waves (*Olbers and Eden, 2013*) has been implemented in a coarse resolution Earth System Model. When forced with energy from the conversion of barotropic tides over rough topography to internal waves, the model simulates a climate qualitatively similar to simulations using a standard background diffusivity with enhanced tidal mixing towards the bottom of the ocean. The climate is slightly colder when using the new parameterization, except for near the tropical upwelling regions where an existing warm bias is amplified. The major differences between simulations using the new and old parameterizations are the thermocline structure and strength of the global overturning circulation, where the Atlantic Meridional Overturning Circulation is weaker and more sensitive to changes in Southern Ocean wind stress when using the new parameterization. These changes are caused by reduced production of North Atlantic Deep Water and weak thermocline mixing rates in the new parameterization, partly explained by the internal wave field only being forced with the energy from conversion of barotropic tides over rough topography, which only accounts for roughly half the energy input to the internal wave field (*Munk and Wunsch, 1998*).

When coupling the new parameterization to a global Earth System Model with active biogeochemistry and prognostic atmospheric carbon dioxide concentration, the main differences are an increased solubility due to the reduced ocean temperature and an increased soft-tissue pump strength. This is a result of weaker ventilation and reduced surface nutrient concentrations and export production.

Using the new mixing parameterization, two simulations have been carried out

investigating the carbon cycle response to a collapse of the Atlantic Overturning Circulation induced by a change in Earth's orbital parameters, reducing summer and annual mean insolation at high latitudes. The resulting change in atmospheric carbon dioxide concentration is an increase of almost 10 ppmv over one millennium, caused by a roughly equal partitioning of terrestrial and oceanic release of carbon. The terrestrial carbon is released first within a few centuries of the insolation perturbation due to southward migration of the tropical precipitation pattern caused by the overturning collapse. The oceanic release acts on a slower timescale, releasing carbon as a result of reduced carbon uptake due to reduced primary production and increased ventilation in the Pacific sector of the Southern Ocean. The Atlantic and Indian sector of the Southern Ocean, on the other hand, release less carbon to the atmosphere. The simulated response of the model to an overturning collapse resemble many features of the climate system observed in proxy records during Heinrich stadials of the last glacial, and thus the combination of terrestrial and oceanic response is a candidate to explaining the 10-20 ppmv stadial increase in carbon dioxide concentration observed in ice cores (*Ahn and Brook, 2014*).

It has been demonstrated that oceanic vertical mixing can vary greatly in response to changes in ocean circulation if it is globally stratification-dependent, with consequences for the carbon cycle through a reduced diffusive transport of nutrients from the abyss to the upper ocean. In addition, forced simulations suggest that the Atlantic overturning is more sensitive to changes in the Southern Ocean wind stress with the new parameterization. Preliminary simulations also indicate that the overturning is more sensitive to changes in Earth's orbital configuration. As a result, feedbacks arising from perturbations of the ocean stratification can affect the marine carbon cycle through its impact on solubility and nutrient transport as well as ocean circulation and ventilation. To fully quantify these impacts, more research is needed.

The model setup is not without issues. The applied insolation change is drastic, and it is difficult to quantify the impact it has on the carbon cycle response. Furthermore, the lack of a simulation using the old mixing parameterization where the overturning collapses renders it impossible to quantify the importance of the mixing changes on the nutrient and carbon cycle. Unsuccessful attempts of modifying the standard parameterization to arrive at such simulation have been made repeatedly during the study period. In addition to these issues it has previously been shown that the background state of the climate is important to the carbon cycle response to an overturning collapse (*Menviel et al., 2008*). This raises ques-

tions to the robustness of the results, as well as how well it can be analyzed as an analogue to past abrupt climate change. This robustness could be checked by repeating the experiment on different background climate states, such as those presented in Chapter 7.1, or by applying freshwater forcing to the North Atlantic as is often done to collapse the overturning circulation.

Another drawback of the presented work analyzing the carbon cycle are the uncertainties in the estimates of the oceanic carbon pumps. Preformed alkalinity and nutrients are key variables for quantifying the strength of the organic and carbonate pumps, but are not implemented in the model used for this study. Furthermore, the lack of an explicit estimate of the solubility and disequilibrium pumps renders it difficult to pinpoint the mechanisms by which the ocean gains or loses carbon as disequilibrium obscures the calculations of organic carbon using apparent oxygen utilization (*Ito et al., 2004; Ito and Follows, 2005*).

In particular, the role of the disequilibrium pump has recently received increased interest with respect to glacial-interglacial variations in  $p\text{CO}_2$  (*Eggleston and Galbraith, 2018; Ferreira et al., 2018*). A meaningful next step is implementing the necessary tracers for a robust estimate of the strength of the different carbon pumps in fully coupled climate models so that the errors in the estimates of organic and carbonate pump strengths are removed, and the disequilibrium component can be quantified. Tools have been developed for this, and the implementation in a coupled coarse resolution Earth System Model, such as the one used throughout this thesis, should be fairly straight-forward. A challenge remains to directly track the saturated carbon due to solubility in a model where  $p\text{CO}_2$  varies, where many models today overcome this issue by using fixed atmospheric  $p\text{CO}_2$  (*Eggleston and Galbraith, 2018; Ödalen et al., 2018*). The goal of focusing on these explicit separations of the carbon pumps is to disentangle the blurring effect disequilibrium has on the strength of the solubility and organic pump, and increase our understanding of the importance of its role in millennial or glacial-interglacial timescale  $p\text{CO}_2$  fluctuations (*Toggweiler et al., 2003a,b; Ito and Follows, 2013; Eggleston and Galbraith, 2018*).

Other tools are continuously being developed that can aid the understanding of past and future changes in the carbon cycle if implemented in models such as the one used in this work. These developments include isotope modeling, which enables modelers to compare model simulations with ocean sediments and proxy records (e.g. *Schmittner and Lund, 2015; Muglia et al., 2018*), and the use of Green functions to explicitly track the origin of deep watermasses (e.g. *Kwon et al., 2011*).

With increasing computational power, these tools can be implemented and tested in fully coupled general circulation models and run for several millennia or even a full glacial cycle and hopefully contribute to our understanding of past fluctuations in the global carbon cycle.

At present, vertical mixing is shown in Chapter 7 to influence the carbon cycle greatly depending not only on the amount of energy provided for mixing, but also on where it is provided. Thus, the commonly used ad-hoc vertical dissipation profile in the *St. Laurent et al. (2002)* parameterization, being independent of stratification, is unrealistically robust to drastic changes in circulation. The vertical structure of dissipation is generally observed to scale with  $N^2$  (*Waterhouse et al., 2014*), and the way the dissipation is scaled has been shown to impact global ocean temperature and overturning rates (*Melet et al., 2016*). It has not yet been shown what the impact is on the carbon cycle, but the preliminary results in Chapter 7.2 suggest that vertical and horizontal structure of mixing is crucial to the nutrient and carbon cycle. It is therefore likely that changes in mixing resulting from changes in either stratification or internal wave forcing have impacted the global carbon cycle in the past. The large body of work on both the observational and modeling side of mixing generated by internal wave breaking and marine carbon cycle dynamics within the last decade inspire hope that these questions can and will be answered within the near future.

# Bibliography

- Ahn, J., and E. Brook (2008), Atmospheric CO<sub>2</sub> and climate on millennial time scales during the last glacial period, *Science*, *322*, 83–85, doi:[10.1126/science.1160832](https://doi.org/10.1126/science.1160832).
- Ahn, J., and E. Brook (2014), Siple dome ice reveals two modes of millennial CO<sub>2</sub> change during the last ice age, *Nature Communications*, *5*, 3723, doi:[10.1038/ncomms4723](https://doi.org/10.1038/ncomms4723).
- Alford, M. (2003), Improved global maps and 54-year history of wind-work on ocean inertial motions, *Geophys. Res. Lett.*, *30*, 1424, doi:[10.1029/2002GL016614](https://doi.org/10.1029/2002GL016614).
- Allen, J., U. Brandt, A. Brauer, H.-W. Hubberten, B. Huntley, J. Keller, M. Kraml, A. Mackensen, J. Mingram, J. Negendank, N. Nowaczyk, H. Oberhänsli, W. Watts, S. Wulf, and B. Zolitschka (1999), Rapid environmental changes in southern europe during the last glacial period, *Nature*, *400*, 740–743, doi:[10.1038/23432](https://doi.org/10.1038/23432).
- Anderson, L., and J. Sarmiento (1994), Redfield ratios of remineralization determined by nutrient data analysis, *Glob. Biogeochem. Cycles*, *8*, 65–80, doi:[10.1029/93GB03318](https://doi.org/10.1029/93GB03318).
- Anderson, R., and M.-E. Carr (2010), Uncorking the Southern Ocean’s Vintage CO<sub>2</sub>, *Science*, *328*, 1117–1118, doi:[10.1126/science.1190765](https://doi.org/10.1126/science.1190765).
- Anderson, R., S. Ali, L. Bradtmiller, S. Nielsen, M. Fleischer, and L. Anderson, B.E. and Burckle (2009), Wind-driven upwelling in the southern ocean and the deglacial rise in atmospheric CO<sub>2</sub>, *Science*, *323*, 1443–1448, doi:[10.1126/science.1167441](https://doi.org/10.1126/science.1167441).
- Arneborg, L. (2002), Mixing Efficiencies in Patchy Turbulence, *J. Phys. Ocean.*, *32*, 1496–1506, doi:[10.1175/1520-0485\(2002\)032<1496:MEIPT>2.0.CO;2](https://doi.org/10.1175/1520-0485(2002)032<1496:MEIPT>2.0.CO;2).
- Baldini, J., R. Brown, and J. McElwaine (2015), Was millennial scale climate change during the Last Glacial triggered by explosive volcanism?, *Sci. Rep.*, *5*, 17,442, doi:[10.1038/srep17442](https://doi.org/10.1038/srep17442).
- Bauska, T., E. Brook, S. Marcott, D. Baggenstos, S. Shackleton, J. Severinghaus, and V. Petrenko (2018), Controls on Millennial-Scale Atmospheric CO<sub>2</sub> Variability During the Last Glacial Period, *Geophys. Res. Lett.*, *45*, doi:[10.1029/2018GL077881](https://doi.org/10.1029/2018GL077881).

- Bell, T. (1975), Topographically generated internal waves in the open ocean, *Journal of Geophysical Research*, *80*, 320–327, doi:[10.1029/JC080i003p00320](https://doi.org/10.1029/JC080i003p00320).
- Bereiter, B., D. Lüthi, M. Siegrist, S. Schüpbach, T. Stocker, and H. Fischer (2012), Mode change of millennial CO<sub>2</sub> variability during the last glacial associated with a bipolar marine carbon seesaw, *PNAS*, *109*, 9755–9760, doi:[10.1073/pnas.1204069109](https://doi.org/10.1073/pnas.1204069109).
- Bernadello, R., I. Marinov, J. Palter, J. Sarmiento, E. Galbraith, and R. Slater (2014), Response of the Ocean Natural Carbon Storage to Projected Twenty-First-Century Climate Change, *J. CLimate*, *27*, 2033–2053, doi:[0.1175/JCLI-D-13-00343.1](https://doi.org/0.1175/JCLI-D-13-00343.1).
- Böhm, E., J. Lippold, M. Gutjahr, M. Frank, P. Blaser, B. Antz, J. Fohlmeister, N. Frank, M. Andersen, and M. Deininger (2015), Strong and deep Atlantic meridional overturning circulation during the last glacial cycle, *Nature*, *517*, 73–76, doi:[10.1038/nature14059](https://doi.org/10.1038/nature14059).
- Bond, G., H. Heinrich, W. Broecker, L. Labeyrie, J. McManus, J. Andrews, S. Huon, R. Jantschik, S. Clasen, C. Simet, K. Tedesco, M. Klas, G. Bonani, and S. Ivy (1992), Evidence for massive discharges of icebergs into the north atlantic ocean during the lat glacial period, *Nature*, *360*, 245–249, doi:[10.1038/360245a0](https://doi.org/10.1038/360245a0).
- Bouttes, N., D. M. Roche, and D. Paillard (2012), Systematic study of the impact of fresh water fluxes on the glacial carbon cycle, *Climate of the Past*, *8*(2), 589–607, doi:[10.5194/cp-8-589-2012](https://doi.org/10.5194/cp-8-589-2012).
- Bozbiyik, A., M. Steinacher, F. Joos, T. F. Stocker, and L. Menviel (2011), Fingerprints of changes in the terrestrial carbon cycle in response to large reorganizations in ocean circulation, *Climate of the Past*, *7*(1), 319–338, doi:[10.5194/cp-7-319-2011](https://doi.org/10.5194/cp-7-319-2011).
- Broccoli, A., K. Dahl, and R. Stouffer (2006), Responce of the ITCZ to northern hemisphere cooling, *Geophys. Res. Lett.*, *33*, L01,702, doi:[10.1029/2005GL024546](https://doi.org/10.1029/2005GL024546).
- Broecker, W. (1974), "NO", A conservative water-mass tracer, *Earth and Planet. Sci. Lett.*, *23*, 100–107, doi:[10.1016/0012-821X\(74\)90036-3](https://doi.org/10.1016/0012-821X(74)90036-3).
- Broecker, W. (1982), Glacial to Interglacial Changes in Ocean Chemistry, *Prog. Oceanogr.*, *11*, 161–197, doi:[10.1016/0079-6611\(82\)90007-6](https://doi.org/10.1016/0079-6611(82)90007-6).
- Broecker, W. (1998), Paleocean circulation during the last deglaciation: A bipolar seesaw?, *Paleoceanography*, *13*, 119–121, doi:[10.1029/97PA03707](https://doi.org/10.1029/97PA03707).
- Brown, N., and E. Galbraith (2016), Hosed vs. unhosed: interruptions of the Atlantic Meridional Overturning Circulation in a global coupled model, with and without fresh-water forcing, *Clim. Past.*, *12*, 1663–1679, doi:[10.5194/cp-12-1663-2016](https://doi.org/10.5194/cp-12-1663-2016).

- Bryan, F. (1987), Parameter sensitivity of primitive equation ocean general circulation models, *J. Phys. Oceanogr.*, *17*, 970–985, doi:[10.1175/1520-0485\(1987\)017<0970:PSOPEO>2.0.CO;2](https://doi.org/10.1175/1520-0485(1987)017<0970:PSOPEO>2.0.CO;2).
- Bryan, K., and L. Lewis (1979), A water mass model of the world ocean, *J. Geophys. Res.*, *84*, 2503–2517, doi:[10.1029/JC084iC05p02503](https://doi.org/10.1029/JC084iC05p02503).
- Burke, A., and L. Robinson (2012), The southern ocean’s role in carbon exchange during the last deglaciation, *Science*, *335*, 557–561, doi:[10.1126/science.1208163](https://doi.org/10.1126/science.1208163).
- Cairns, J., and G. Williams (1976), Internal Wave Observations From a Midwater Float, *2*, *J. Geophys. Res.*, *81* (12), 1943–1950, doi:[10.1029/JC081i012p01943](https://doi.org/10.1029/JC081i012p01943).
- Cox, M. (1989), An idealized model of the world ocean. part 1: The global-scale water masses, *J. Phys. Oceanogr.*, *19*, 1730, doi:[10.1175/1520-0485\(1989\)019<1730:AIMOTW>2.0.CO;2](https://doi.org/10.1175/1520-0485(1989)019<1730:AIMOTW>2.0.CO;2).
- Crawford, G., and W. Large (1996), A Numerical Investigation of Resonant Inertial Response of the Ocean to Wind Forcing, *J. Phys. Oceanogr.*, *26*, 873–891, doi:[10.1175/1520-0485\(1996\)026<0873:ANIORI>2.0.CO;2](https://doi.org/10.1175/1520-0485(1996)026<0873:ANIORI>2.0.CO;2).
- Danabasoglu, G., and J. Marshall (2007), Effects of vertical variations of thickness diffusivity in an ocean general circulation model, *Ocean Modell.*, *18*, 122–141.
- Danabasoglu, G., R. Ferrari, and J. C. McWilliams (2008), Sensitivity of an ocean general circulation model to a parameterization of near-surface eddy fluxes, *J. Climate*, *21*, 1192–1208.
- Danabasoglu, G., S. Bates, B. Briegleb, S. Jayne, M. Jochum, W. Large, S. Peacock, and S. Yeager (2012), The CCSM4 ocean component, *J. Climate*, *25*, 1361–1389, doi:[10.1175/JCLI-D-00091.1](https://doi.org/10.1175/JCLI-D-00091.1).
- Dansgaard, W. (1964), Stable isotopes in precipitation, *Tellus*, *16*, 436–468, doi:[10.1111/j.2153-3490.1964.tb00181.x](https://doi.org/10.1111/j.2153-3490.1964.tb00181.x).
- Dansgaard, W., S. Johnsen, H. Clause, D. Dahl-Jensen, N. Gundestrup, C. Hammer, C. Hvidberg, J. Steffensen, A. Sveinbjörnsdóttir, J. Jouzel, and G. Bond (1993), Evidence of general instability of past climate from a 250-kyr ice-core record, *Nature*, *364*, 218–220, doi:[10.1038/364218a0](https://doi.org/10.1038/364218a0).
- de Lavergne, C., G. Madec, J. Le Sommer, A. Nurser, and A. Naveira Garabato (2016), The impact of a variable mixing efficiency on the abyssal overturning, *J. Phys. Oceanogr.*, *46*, 663–681, doi:[10.1175/JPO-D-14-0259.1](https://doi.org/10.1175/JPO-D-14-0259.1).

- Dickson, A., C. Sabine, and J. Christian (Eds.) (2007), *Guide to Best Practices for Ocean CO<sub>2</sub> Measurements*, 191 pp., PICES Special Publication 3.
- Dokken, T., K. Nisancioglu, C. Li, D. Battisti, and C. Kissel (2013), Dansgaard-oeschger cycles: Interactions between ocean and sea ice intrinsic to the nordic seas, *Paleoceanogr.*, *28*, 491–502, doi:[10.1002/palo.20042](https://doi.org/10.1002/palo.20042).
- Doney, S., I. Lima, J. Moore, K. Lindsay, M. Behrenfeld, T. Westberry, N. Mahowald, D. Glover, and T. Takahashi (2009), Skill metrics for confronting global upper ocean ecosystem-biogeochemistry models against field and remote sensing data, *J. Mar. Sys.*, *76*, 95–112, doi:[10.1016/j.jmarsys.2008.05.015](https://doi.org/10.1016/j.jmarsys.2008.05.015).
- Dunne, J., J. Sarmiento, and A. Gnanadesikan (2007), A synthesis of global particle export from the surface ocean and cycling through the ocean interior and on the seafloor, *Glob. Biogeochem. Cycl.*, *21*, GB4006, doi:[10.1029/2006GB002907](https://doi.org/10.1029/2006GB002907).
- Eden, C., and R. Greatbatch (2008), Towards a mesoscale eddy closure, *Ocean Modell.*, *20*, 223–239, doi:[10.1016/j.ocemod.2007.09.002](https://doi.org/10.1016/j.ocemod.2007.09.002).
- Eden, C., and D. Olbers (2014), An energy compartment model for propagation, non-linear interaction, and dissipation of internal gravity waves, *J. Phys. Oceanogr.*, *44*, 2093–2106, doi:[10.1175/JPO-D-13-0224.1](https://doi.org/10.1175/JPO-D-13-0224.1).
- Eden, C., M. Jochum, and G. Danabasoglu (2009), Effects of different closures for thickness diffusivity, *Ocean Modell.*, *26*, 47–59.
- Eden, C., L. Czeschel, and D. Olbers (2014), Toward energetically consistent ocean models, *J. Phys. Oceanogr.*, *44*, 3160–3184, doi:[10.1175/JPO-D-13-0260.1](https://doi.org/10.1175/JPO-D-13-0260.1).
- Egbert, G., and R. Ray (2000), Significant dissipation of tidal energy in the deep ocean inferred from satellite altimeter data, *Nature*, *405*, 775–778, doi:[10.1038/35015531](https://doi.org/10.1038/35015531).
- Egbert, G., R. Ray, and B. Bills (2004), Numerical modeling of the global semidiurnal tide in the present day and in the last glacial maximum, *J. Geophys. Res.*, *109*, C03,003, doi:[10.1029/2003JC001973](https://doi.org/10.1029/2003JC001973).
- Eggleston, S., and E. Galbraith (2018), The devil’s in the disequilibrium: multi-component analysis of dissolved carbon and oxygen changes under a broad range of forcings in a general circulation model, *Biogeosci.*, *15*, 3761–3777, doi:[10.5194/bg-15-3761-2018](https://doi.org/10.5194/bg-15-3761-2018).
- EPICA community members (2006), One-to-one coupling of glacial climate variability in greenland and antarctica, *Nature*, *444*, 196–198, doi:[10.1038/nature05301](https://doi.org/10.1038/nature05301).

- Ezat, M., T. Rasmussen, B. Hönisch, J. Groeneveld, and P. deMenocal (2017), Episodic release of CO<sub>2</sub> from the high-latitude North Atlantic Ocean during the last 135 kyr, *Nature Communications*, *8*, 14,498, doi:[10.1038/ncomms14498](https://doi.org/10.1038/ncomms14498).
- Fasham, M., H. Ducklow, and S. McKelvie (1990), A nitrogen-based model of plankton dynamics in the oceanic mixed layer, *J. Mar. Res.*, *48*, 591–639, doi:[10.1357/002224090784984678](https://doi.org/10.1357/002224090784984678).
- Ferrari, R., J. C. McWilliams, V. M. Canuto, and M. Dubovikov (2008), Parameterization of eddy fluxes near oceanic boundaries, *J. Climate*, *21*, 2770–2789, doi:[10.1175/2007JCLI1510.1](https://doi.org/10.1175/2007JCLI1510.1).
- Ferreira, D., J. Marshall, and P. Heimbach (2005), Estimating eddy stresses by fitting dynamics to observations using a residual-mean ocean circulation model and its adjoint, *J. Phys. Oceanogr.*, *35*, 1891–1910, doi:[10.1175/JPO2785.1](https://doi.org/10.1175/JPO2785.1).
- Ferreira, D., J. Marshall, T. Ito, and D. McGee (2018), Linking Glacial-Interglacial States to Multiple Equilibria of Climate, *Geophys. Res. Lett.*, *45*, 9160–9170, doi:[10.1029/2018GL077019](https://doi.org/10.1029/2018GL077019).
- Ganachaud, A., and C. Wunsch (2000), Improved estimates of global ocean circulation, heat transport and mixing from hydrographic data, *Nature*, *408*, 453–457, doi:[10.1038/35044048](https://doi.org/10.1038/35044048).
- Ganopolski, A., and S. Rahmstorf (2001), Rapid changes of glacial climate simulated in a coupled climate model, *Nature*, *409*, 153–158, doi:[10.1038/35051500](https://doi.org/10.1038/35051500).
- Garrett, C., and W. Munk (1972), Space-time scales of internal waves, *Geophysical Fluid Dynamics*, *3*, 225–264, doi:[10.1080/03091927208236082](https://doi.org/10.1080/03091927208236082).
- Garrett, C., and W. Munk (1975), Space-time scales of internal waves: A progress report, *Journal of Geophysical Research*, *80*, 291–297, doi:[10.1029/JC080i003p00291](https://doi.org/10.1029/JC080i003p00291).
- Gent, P. R., and J. C. McWilliams (1990), Isopycnal mixing in ocean circulation models, *J. Phys. Oceanogr.*, *20*, 150–155.
- Gent, P. R., J. Willebrand, T. J. McDougall, and J. C. McWilliams (1995), Parameterizing eddy-induced tracer transports in ocean circulation models, *J. Phys. Oceanogr.*, *25*, 463–474.
- Gent, P. R., W. G. Large, and F. O. Bryan (2001), What sets the mean transport through drake passage, *J. Geophys. Res.*, *106*, 2693–2712, doi:[10.1029/2000JC900036](https://doi.org/10.1029/2000JC900036).

- Gent, P. R., G. Danabasoglu, L. J. Donner, M. M. Holland, E. C. Hunke, S. R. Jayne, D. M. Lawrence, R. B. Neale, P. J. Rasch, M. Vertenstein, P. H. Worley, Z.-L. Yang, and M. Zhang (2011), The community climate system model version 4, *J. Climate*, *24*, 4973–4991, doi:[10.1175/2011JCLI4083.1](https://doi.org/10.1175/2011JCLI4083.1).
- Gill, A. E. (1982), *Atmosphere-Ocean Dynamics*, 662 pp., Academic Press.
- Gnanadesikan, A. (1999), A Simple Predictive Model for the Structure of the Oceanic Pycnocline, *Science*, *283*, 2077–2079, doi:[10.1126/science.283.5410.2077](https://doi.org/10.1126/science.283.5410.2077).
- Gottschalk, J., L. Skinner, J. Lippold, H. Vogel, N. Frank, S. Jaccard, and C. Waelbroeck (2016), Biological and physical controls in the southern ocean on past millennial-scale atmospheric CO<sub>2</sub> changes, *Nature Comm.*, *7*, 11,539, doi:[10.1038/ncomms11539](https://doi.org/10.1038/ncomms11539).
- Govin, A., et al. (2012), Persistent influence of ice sheet melting on high northern latitude during the early last interglacial, *Clim. Past*, *8*, 483–507, doi:[10.5194/cp-8-483-2012](https://doi.org/10.5194/cp-8-483-2012).
- Gregg, M. (1989), Scaling turbulent dissipation in the thermocline, *J. Geophys. Res.*, *94*, 9686–9698, doi:[10.1029/JC094iC07p09686](https://doi.org/10.1029/JC094iC07p09686).
- Gregg, M., E. D’Asaro, J. Riley, and E. Kunze (2018), Mixing Efficiency in the Ocean, *Annu. Rev. Mar. Sci.*, *10*, 443–473, doi:[10.1146/annurev-marine-121916-063643](https://doi.org/10.1146/annurev-marine-121916-063643).
- Gruber, N., J. Sarmiento, and T. Stocker (1996), Improved method for detecting anthropogenic CO<sub>2</sub> in the oceans, *Global Biogeochem. Cycles*, *10*, 809–837, doi:[10.1029/96GB01608](https://doi.org/10.1029/96GB01608).
- Gruber, N., et al. (2009), Oceanic sources, sinks and transport of atmospheric CO<sub>2</sub>, *Global Biogeochem. Cycles*, *23*, GB1005, doi:[doi:10.1029/2008GB003349](https://doi.org/10.1029/2008GB003349).
- Harlaß, J., M. Latif, and W. Park (2015), Improving climate model simulation of tropical atlantic sea surface temperature: The importance of enhanced vertical atmosphere model resolution, *Geophys. Res. Lett.*, *42*, 2401–2408, doi:[10.1002/2015GL063310](https://doi.org/10.1002/2015GL063310).
- Harrison, M., and R. Hallberg (2008), Pacific subtropical cell response to reduced equatorial dissipation, *J. Phys. Oceanogr.*, *38*, 1894–1912, doi:[10.1175/2008JPO3708.1](https://doi.org/10.1175/2008JPO3708.1).
- Henry, L., J. McManus, W. Curry, N. Roberts, A. Piotrowski, and L. Keigwin (2016), North Atlantic ocean circulation and abrupt climate change during the last glaciation, *Science*, *353*, 470–474, doi:[10.1126/science.aaf4767](https://doi.org/10.1126/science.aaf4767).
- Heyney, F., J. Wright, and S. Flatté (1986), Energy and action flow through the internal wave field: An eikonal approach, *J. Geophys. Res.*, *91 (C7)*, 8487–8495, doi:[10.1029/JC091iC07p08487](https://doi.org/10.1029/JC091iC07p08487).

- Hoffman, F., J. Randerson, V. Arora, Q. Bao, P. Cadule, D. Ji, C. Jones, M. Kawamiya, S. Khatiwala, K. Lindsay, A. Obata, E. Shevliakova, K. Six, J. Tjiputra, E. Volodin, and T. Wu (2014), Causes and implications of persistent atmospheric dioxide biases in earth system models, *J. Geophys. Res. Biogeosci.*, *119*, 141–162, doi:[10.1002/2013JG002381](https://doi.org/10.1002/2013JG002381).
- Huang, R., M. Cane, N. Naik, and P. Goodman (2000), Global adjustment of the thermocline in response to deepwater formation, *Geophys. Res. Lett.*, *27*, 759–762, doi:[10.1029/1999GL002365](https://doi.org/10.1029/1999GL002365).
- Huber, C., M. Leuenerger, R. Spahni, J. Flückiger, J. Schwander, T. Stocker, S. Johnsen, A. Landais, and J. Jouzel (2006), Isotope calibrated Greenland temperature record over Marine Isotope Stage 3 and its relation to CH<sub>4</sub>, *Earth Planet. Sci. Lett.*, *243*, 504–519, doi:[10.1016/j.epsl.2006.01.002](https://doi.org/10.1016/j.epsl.2006.01.002).
- Hunke, E., and W. Lipscomb (2008), *CICE: The Los Alamos sea ice model documentation and software user's manual version 4.1*, 76 pp., Los Alamos National Laboratory Tech. Rep. LA-CC-06-012.
- Hurrell, J. W., et al. (2013), The community earth system model - a framework for collaborative research, *Bull. Am. Meteorol. Soc.*, *94*, 1339–1360, doi:[10.1175/BAMS-D-12-00121.1](https://doi.org/10.1175/BAMS-D-12-00121.1).
- Ito, T., and M. Follows (2003), Upper ocean control on the solubility pump of CO<sub>2</sub>, *J. Mar. Res.*, *61*, 465–489, doi:[10.1357/002224003322384898](https://doi.org/10.1357/002224003322384898).
- Ito, T., and M. Follows (2005), Preformed phosphate, soft tissue pump and atmospheric CO<sub>2</sub>, *J. Mar. Res.*, *63*, 813–839, doi:[10.1357/0022240054663231](https://doi.org/10.1357/0022240054663231).
- Ito, T., and M. Follows (2013), Air-sea disequilibrium of carbon dioxide enhances the biological carbon sequestration in the Southern Ocean, *Glob. Biogeochem. Cycl.*, *27*, 1129–1138, doi:[10.1002/2013GB004682](https://doi.org/10.1002/2013GB004682).
- Ito, T., M. Follows, and E. Boyle (2004), is AOU a good measure of respiration in the oceans?, *Geophys. Res. Lett.*, *31*, L17,305, doi:[10.1029/2004GL020900](https://doi.org/10.1029/2004GL020900).
- Jaccard, S., E. Galbraith, A. Martinez-Garcia, and R. Anderson (2016), Covariation of deep southern ocean oxygenation and atmospheric CO<sub>2</sub> through the last ice age, *Nature*, *530*, 207–210, doi:[10.1038/nature16514](https://doi.org/10.1038/nature16514).
- Jahn, A., K. Sterling, M. Holland, J. Kay, J. Maslanik, C. Bitz, D. Bailey, J. Stroeve, E. Hunke, W. Lipscomb, and D. Pollak (2012), Late-Twentieth-Century Simulation

- of Arctic Sea Ice and Ocean Properties in the CCSM4, *J. Climate*, *25*, 1431–1452, doi:[10.1175/JCLI-D-11-00201.1](https://doi.org/10.1175/JCLI-D-11-00201.1).
- Jansen, M. (2016), Glacial ocean circulation and stratification explained by reduced atmospheric temperature, *PNAS*, *114* (1), 45–50, doi:[10.1073/pnas.1610438113](https://doi.org/10.1073/pnas.1610438113).
- Jayne, S. (2009), The impact of abyssal mixing parameterizations in an ocean general circulation model, *J. Phys. Oceanogr.*, *39*, 1756–1775, doi:[10.1175/2009JPO4085.1](https://doi.org/10.1175/2009JPO4085.1).
- Jayne, S., and L. St. Laurent (2001), Parameterizing tidal dissipation over rough topography, *Geophys. Res. Lett.*, *28* (5), 811–814, doi:[10.1029/2000GL012044](https://doi.org/10.1029/2000GL012044).
- Jochum, M. (2009), Impact of latitudinal variations in vertical diffusivity on climate simulations, *J. Geophys. Res.*, *114*, C01,010, doi:[10.1029/2008JC005030](https://doi.org/10.1029/2008JC005030).
- Jochum, M., and C. Eden (2015), The connection between southern ocean winds, the atlantic meridional overturning circulation, and indo-pacific upwelling, *J. Climate*, *28*, 9250–9257, doi:[10.1175/JCLI-D-15-0263.1](https://doi.org/10.1175/JCLI-D-15-0263.1).
- Jochum, M., and J. Potemra (2008), Sensitivity of tropical rainfall to banda sea diffusivity in the community climate system model, *J. Climate*, *21*, 6445–6454, doi:[10.1175/2008JCLI2230.1](https://doi.org/10.1175/2008JCLI2230.1).
- Jochum, M., G. Danabasoglu, M. Holland, Y. Kwon, and W. Large (2008), Ocean viscosity and climate, *J. Geophys. Res.*, *25*, C06,017.
- Jochum, M., S. Peacock, K. Moore, and K. Lindsay (2010), Response of air-sea carbon fluxes and climate to orbital forcing changes in the community climate system model, *Paleoceanography*, *25*, PA3201, doi:[10.1029/2009PA001856](https://doi.org/10.1029/2009PA001856).
- Jochum, M., A. Jahn, D. Peacock, S. Bailey, J. Fatsulo, J. Kay, S. Levis, and B. Otto-Bliesner (2012), True to Milankovitch: Glacial Inception in the New Community Climate System Model, *J. Climate*, *25*, 2226–2239, doi:[10.1175/JCLI-D-11-00044.1](https://doi.org/10.1175/JCLI-D-11-00044.1).
- Jochum, M., B. Briegleb, G. Danabasoglu, W. Large, N. Norton, S. Jayne, M. Alford, and F. Bryan (2013), The impact of oceanic near-inertial waves on climate, *J. Climate*, *26*, 2833–2844, doi:[10.1175/JCLI-D-12-00181.1](https://doi.org/10.1175/JCLI-D-12-00181.1).
- Kanner, L., S. Burns, H. Cheng, and R. Edwards (2012), High-latitude forcing of the South American summer monsoon during the last glacial, *Science*, *335*, 570–573, doi:[10.1126/science.1213397](https://doi.org/10.1126/science.1213397).

- Kindler, P., M. Guillevic, M. Baumgartner, J. Schwander, A. Landais, and M. Leuenberger (2014), Temperature reconstruction from 10 to 120 kyr b2k from the NGRIP ice core, *Clim. Past*, *10*, 887–902, doi:[10.5194/cp-10-887-2014](https://doi.org/10.5194/cp-10-887-2014).
- Kleppin, H., M. Jochum, B. Otto-Bliesner, C. Shields, and S. Yeager (2015), Stochastic atmospheric forcing as a cause of greenland climate transitions, *J. Climate*, *28*, 7741–7763, doi:[10.1175/JCLI-D-14-00728.1](https://doi.org/10.1175/JCLI-D-14-00728.1).
- Klymak, J., J. Moum, J. Nash, E. Kunze, J. Girton, G. Carter, C. Lee, S. T.B., and M. Gregg (2006), An Estimate of Tidal Energy Lost to Turbulence at the Hawaiian Ridge, *J. Phys. Oceanogr.*, *36*, 1148–1164, doi:[10.1175/JPO2885.1](https://doi.org/10.1175/JPO2885.1).
- Knox, F., and M. McElroy (1984), Changes in atmospheric CO<sub>2</sub>: Influence of the marine biota at high latitude, *J. Geophys. Res.*, *89*, 4629–4637, doi:[10.1029/JD089iD03p04629](https://doi.org/10.1029/JD089iD03p04629).
- Kohfeld, K., and A. Ridgwell (2009), Glacial-interglacial variability in atmospheric CO<sub>2</sub>, in *Surface Ocean-Lower Atmosphere Processes*, edited by C. Quéré and E. Saltzman, pp. 251–286, American Geophysical Union, doi:[10.1029/2008GM000845](https://doi.org/10.1029/2008GM000845).
- Köhler, P., F. Joos, S. Gerber, and R. Knutti (2005), Simulated changes in vegetation distribution, land carbon storage, and atmospheric CO<sub>2</sub> in response to a collapse of the North Atlantic thermohaline circulation, *Climate Dynamics*, *25*(7), 689–708, doi:[10.1007/s00382-005-0058-8](https://doi.org/10.1007/s00382-005-0058-8).
- Kuhlbrodt, T., A. Griesel, M. Montoya, A. Levermann, M. Hofmann, and S. Rahmstorf (2007), On the driving processes of the atlantic meridional overturning circulation, *Rev. Geophys.*, *45*(2004RG000166), RG2001, doi:[10.1029/2004RG000166](https://doi.org/10.1029/2004RG000166).
- Kunze, E. (2017), Internal-wave-driven mixing: Global geography and budgets, *Journal of Physical Oceanography*, *47*, 1325–1345, doi:[10.1175/JPO-D-16-0141.1](https://doi.org/10.1175/JPO-D-16-0141.1).
- Kwon, E., J. Sarmiento, J. Toggweiler, and T. DeVries (2011), The control of atmospheric pCO<sub>2</sub> by ocean ventilation change: The effect of the oceanic storage of biogenic carbon, *Glob. Biogeochem. Cycl.*, *25*, GB3026, doi:[10.1029/2011GB004059](https://doi.org/10.1029/2011GB004059).
- Large, W., and S. Yeager (2004), *Diurnal to decadal global forcing for ocean and sea-ice models: the data sets and flux climatologies*, NCAR.
- Large, W. G., J. C. McWilliams, and S. C. Doney (1994), Oceanic vertical mixing: A review and a model with a nonlocal boundary layer parameterization, *Reviews of Geophysics*, *32*, 363–403, doi:[10.1029/94RG01872](https://doi.org/10.1029/94RG01872).

- Laskar, J., P. Robutel, F. Joutel, M. Gastineau, A. C. M. Correia, and B. Levrard (2004), A long-term numerical solution for the insolation quantities of the earth, *Astronomy and Astrophysics*, *428*(1), 261–285, doi:[10.1051/0004-6361:20041335](https://doi.org/10.1051/0004-6361:20041335).
- Lauderdale, J., A. Naveira Garabato, K. Oliver, M. Follows, and R. Williams (2013), Wind-driven changes in Southern Ocean residual circulation, ocean carbon reservoirs and atmospheric CO<sub>2</sub>, *Clim. Dyn.*, *41*, 2145–2164, doi:[10.1007/s00382-012-1650-3](https://doi.org/10.1007/s00382-012-1650-3).
- Lawrence, D., et al. (2011), Parameterization Improvements and Functional and Structural Advances in Version 4 of the Community Land Model, *J. Adv. Model. Earth Syst.*, *3*, M03,001, doi:[10.1029/2011MS000045](https://doi.org/10.1029/2011MS000045).
- Le Quéré, C., et al. (2005), Ecosystem dynamics based on plankton functional types for global ocean biogeochemistry models, *Glob. Change Bio.*, *11*, 2016–2040, doi:[10.1111/j.1365-2486.2005.01004.x](https://doi.org/10.1111/j.1365-2486.2005.01004.x).
- Ledwell, J., A. Watson, and C. Law (1998), Mixing of a tracer in the pycnocline, *Journ. Geophys. Res.*, *103*, 21,499–21,529, doi:[10.1029/98JC01738](https://doi.org/10.1029/98JC01738).
- Lee, S.-Y., J. Chiang, K. Matsumoto, and K. Tokos (2011), Southern Ocean wind response to North Atlantic cooling and the rise in atmospheric CO<sub>2</sub>: Modeling perspective and paleoceanographic implications, *Paleoceanography*, *26*, PA1214, doi:[10.1029/2010PA002004](https://doi.org/10.1029/2010PA002004).
- Lefauve, A., C. Muller, and A. Melet (2015), A three-dimensional map of tidal dissipation over abyssal hills, *J. Geophys. Res.*, *120*, 4760–4777, doi:[10.1002/2014JC010598](https://doi.org/10.1002/2014JC010598).
- Li, C., and D. Battisti (2008), Reduced Atlantic Storminess during Last Glacial Maximum: Evidence from a Coupled Climate Model, *J. Climate*, *21*, 3561–3579, doi:[10.1175/2007JCLI2166.1](https://doi.org/10.1175/2007JCLI2166.1).
- Li, C., D. Battisti, D. Schrag, and E. Tziperman (2005), Abrupt climate shifts in Greenland due to displacements of the sea ice edge, *Geophys. Res. Lett.*, *32*, L19,702, doi:[10.1029/2005GL023492](https://doi.org/10.1029/2005GL023492).
- Lindsay, K., G. Bonan, S. Doney, F. Hoffman, D. Lawrence, M. C. Long, N. Mahowald, J. Moore, J. Randerson, and P. Thornton (2014), Preindustrial-Control and Twentieth-Century Carbon Cycle Experiments with the Earth System Model CESM1(BGC), *J. Climate*, *27*, 8981–9005, doi:[10.1175/JCLI-D-12-00565.1](https://doi.org/10.1175/JCLI-D-12-00565.1).
- Locarnini, R., A. Mishonov, J. Antonov, T. Boyer, H. Garcia, O. Baranova, M. Zweng, and D. Johnson (2010), *World Ocean Atlas 2009, Volume 1: Temperature*, NOAA Atlas NESDIS 68.

- MacKinnon, J. A., et al. (2017), Climate process team on internal-wave driven ocean mixing, *Bull. Am. Meteorol. Soc.*, *In Press*, doi:[10.1175/BAMS-D-16-0030.1](https://doi.org/10.1175/BAMS-D-16-0030.1).
- Marinov, I., and A. Gnanadesikan (2011), Changes in ocean circulation and carbon storage are decoupled from air-sea pCO<sub>2</sub> fluxes, *Biogeosciences*, *8*, 505–513, doi:[10.5194/bg-8-505-2011](https://doi.org/10.5194/bg-8-505-2011).
- Marinov, I., M. Follows, A. Gnanadesikan, J. Sarmiento, and R. Slater (2008), How does ocean biology affect atmospheric pCO<sub>2</sub>? theory and models, *J. Geophys. Res.*, *113*, C07,032, doi:[10.1029/2007JGC004598](https://doi.org/10.1029/2007JGC004598).
- Markle, B., E. Steig, C. Buizert, S. Schoenemann, C. Bitz, T. Fudge, J. Pedro, Q. Ding, T. Jones, J. White, and T. Sowers (2017), Global atmospheric teleconnections during dansgaard-oeschger events, *Nat. Geosci.*, *10*, 36–40, doi:[10.1038/ngeo2848](https://doi.org/10.1038/ngeo2848).
- Marotzke, J. (1997), Boundary mixing and the dynamics of three-dimensional thermohaline circulation, *J. Phys. Oceanography*, *27*, 1713–1728, doi:[10.1175/1520-0485\(1997\)027<1713:BMATDO>2.0.CO;2](https://doi.org/10.1175/1520-0485(1997)027<1713:BMATDO>2.0.CO;2).
- McComas, C., and P. Müller (1981a), Time scales of resonant interactions among oceanic internal waves, *J. Phys. Oceanogr.*, *11*, 139–147, doi:[10.1175/1520-0485\(1981\)011<0139:TSORIA>2.0.CO;2](https://doi.org/10.1175/1520-0485(1981)011<0139:TSORIA>2.0.CO;2).
- McComas, C., and P. Müller (1981b), The dynamic balance of internal waves, *J. Phys. Oceanogr.*, *11*, 970–986, doi:[10.1175/1520-0485\(1981\)011<0970:TDBOIW>2.0.CO;2](https://doi.org/10.1175/1520-0485(1981)011<0970:TDBOIW>2.0.CO;2).
- Melet, A., R. Hallberg, S. Legg, and K. Polzin (2013), Sensitivity of the ocean state to the vertical distribution of internal-tide-driven mixing, *J. Phys. Oceanogr.*, *43*, 602–615, doi:[10.1175/JPO-D-12-055.1](https://doi.org/10.1175/JPO-D-12-055.1).
- Melet, A., R. Hallberg, S. Legg, and M. Nikurashin (2014), Sensitivity of the ocean state to lee wave-driven mixing, *J. Phys. Oceanogr.*, *44*, 900–921, doi:[10.1175/JPO-D-13-072.1](https://doi.org/10.1175/JPO-D-13-072.1).
- Melet, A., S. Legg, and R. Hallberg (2016), Climate impacts of parameterized local and remote tidal mixing, *J. Climate*, *29*, 3473–3500, doi:[10.1175/JCLI-D-15-0153.1](https://doi.org/10.1175/JCLI-D-15-0153.1).
- Menviel, L., A. Timmermann, A. Mouchet, and O. Timm (2008), Meridional reorganization of marine and terrestrial productivity during heinrich events, *Paleoceanography*, *23*, PA1203, doi:[10.1029/2007PA001445](https://doi.org/10.1029/2007PA001445).

- Menziel, L., P. Spence, and M. England (2015), Contribution of enhanced Antarctic Bottom Water formation to Antarctic warm events and millennial-scale atmospheric CO<sub>2</sub> increase, *Earth and Planetary Science Letters*, *413*, 37 – 50, doi:<https://doi.org/10.1016/j.epsl.2014.12.050>.
- Menziel, L., P. Spence, J. Yu, M. Chamberlain, M. R.J., K. Meissner, and M. England (2018), Southern Hemisphere westerlies as a driver of the early deglacial atmospheric CO<sub>2</sub> rise, *Nature Communications*, *9*, 2503, doi:[10.1038/s41467-018-04876-4](https://doi.org/10.1038/s41467-018-04876-4).
- Menziel, M., L. England, K. Meissner, A. Mouchet, and J. Yu (2014), Atlantic-pacific seesaw and its role in outgassing CO<sub>2</sub> during heinrich events, *Paleoceanogr.*, *29*, 58–70, doi:[10.1002/2013PA002542](https://doi.org/10.1002/2013PA002542).
- Moore, J., S. Doney, and K. Lindsay (2004), Upper ocean ecosystem dynamics and iron cycling in a global three-dimensional model, *Global Biogeochem. Cycles*, *18*, GB4028, doi:[10.1029/2004GB002220](https://doi.org/10.1029/2004GB002220).
- Moore, J., K. Lindsay, S. Doney, M. C. Long, and K. Misumi (2013), Marine Ecosystem Dynamics and Biogeochemical Cycling in the Community Earth System Model [CESM1(BGC)]: Comparison of the 1990s with the 2090s under the RCP4.5 and RCP8.5 Scenarios, *J. Climate*, *26*, 9291–9312, doi:[10.1175/JCLI-D-12-00566.1](https://doi.org/10.1175/JCLI-D-12-00566.1).
- Muglia, J., L. Skinner, and A. Schmittner (2018), Weak overturning circulation and high Southern Ocean nutrient utilization maximized glacial ocean carbon, *Earth and Planet. Sci. Lett.*, *496*, 47–56, doi:[10.1016/j.epsl.2018.05.038](https://doi.org/10.1016/j.epsl.2018.05.038).
- Müller, P., and M. Briscoe (1999), Diapycnal mixing and internal waves, in *Dynamics of Oceanic Internal Gravity Waves: Proc. 11th Aha Huliko'a Hawaiian Workshop*, pp. 289–294, University of Hawai'i at Mānoa.
- Müller, P., and A. Natarov (2003), The internal wave action model (IWAM), in *Near Boundary Processes and Their Parameterization: Proc. 13th Aha Huliko'a Hawaiian Winter Workshop*, pp. 95–105, University of Hawai'i at Mānoa.
- Munday, D., H. Johnson, and D. Marshall (2013), Eddy saturation of equilibrated circumpolar currents, *J. Phys. Oceanogr.*, *43*, 507–532, doi:[10.1175/JPO-D-12-095.1](https://doi.org/10.1175/JPO-D-12-095.1).
- Munk, W. (1966), Abyssal recipes, *Deep Sea Res.*, *13*, 707–730, doi:[10.1016/0011-7471\(66\)90602-4](https://doi.org/10.1016/0011-7471(66)90602-4).
- Munk, W. (1981), Internal Waves and Small-Scale Processes, in *Evolution of Physical Oceanography*, edited by B. Warren and C. Wunsch, pp. 264–291, The MIT Press.

- Munk, W., and C. Wunsch (1998), Abyssal recipes ii: energetics of tidal and wind mixing, *Deep Sea Res.*, *45*, 1977–2010, doi:[10.1016/S0967-0637\(98\)00070-3](https://doi.org/10.1016/S0967-0637(98)00070-3).
- Neale, R., J. Richter, S. Park, P. Lauritzen, S. Vavrus, P. Rasch, and M. Zhang (2013), The Mean Climate of the Community Atmosphere Model (CAM4) in Forced SST and Fully Coupled Experiments, *J. Climate*, *26*, 5150–5168, doi:[10.1175/JCLI-D-12-00236.1](https://doi.org/10.1175/JCLI-D-12-00236.1).
- Nielsen, S., M. Jochum, C. Eden, and R. Nuterman (2018), An energetically consistent vertical mixing parameterization in CCSM4, *Ocean Modell.*, *127*, 46–54, doi:[10.1016/j.ocemod.2018.03.002](https://doi.org/10.1016/j.ocemod.2018.03.002).
- Nikurashin, M., and R. Ferrari (2010), Radiation and dissipation of internal waves generated by geostrophic motions impinging on small-scale topography: Theory, *J. Phys. Oceanogr.*, *40*, 1055–1074, doi:[10.1175/2009JPO4199.1](https://doi.org/10.1175/2009JPO4199.1).
- Nikurashin, M., and R. Ferrari (2011), Global energy conversion rate from geostrophic flows into internal lee waves in the deep ocean, *Geophys. Res. Letters*, *38*, L08,610, doi:[10.1029/2011GL046576](https://doi.org/10.1029/2011GL046576).
- Nycander, J. (2005), Generation of internal waves in the deep ocean by tides, *J. Geophys. Res.*, *110*, C10,028, doi:[10.1029/2004JC002487](https://doi.org/10.1029/2004JC002487).
- Obata, A. (2007), Climate-carbon cycle model response to freshwater discharge into the North Atlantic, *Journal of Climate*, *20*(24), 5962–5976, doi:[10.1175/2007JCLI1808.1](https://doi.org/10.1175/2007JCLI1808.1).
- Ödalen, M., J. Nycander, K. Oliver, L. Brodeau, and A. Ridgwell (2018), The influence of the ocean circulation state on ocean carbon storage and CO<sub>2</sub> drawdown potential in an earth system model, *Biogeosciences*, *15*, 1367–1393, doi:[10.5194/bg-15-1367-2018](https://doi.org/10.5194/bg-15-1367-2018).
- Olbers, D. (1983), Models of the oceanic internal wave field, *Reviews of Geophysics and Space Physics*, *21*, 1567–1606, doi:[10.1029/RG021i007p01567](https://doi.org/10.1029/RG021i007p01567).
- Olbers, D., and C. Eden (2013), A global model for the diapycnal diffusivity induced by internal gravity waves, *J. Phys. Oceanogr.*, *43*, 1759–1779, doi:[10.1175/JPO-D-12-0207.1](https://doi.org/10.1175/JPO-D-12-0207.1).
- Omta, A., S. Dutkiewicz, and M. Follows (2011), Dependence of the ocean-atmosphere partitioning of carbon on temperature and alkalinity, *Global Biogeochem. Cycles*, *25*, GB1003, doi:[10.1029/2010GB003839](https://doi.org/10.1029/2010GB003839).
- Osborn, T. (1980), Estimates of the local rate of vertical diffusion from dissipation measurements, *J. Phys. Oceanogr.*, *10*, 83–89, doi:[10.1175/1520-0485\(1980\)010<0083:EOTLRO>2.0.CO;2](https://doi.org/10.1175/1520-0485(1980)010<0083:EOTLRO>2.0.CO;2).

- Pausata, F., L. Chafik, R. Caballero, and D. S. Battisti (2015), Impacts of high-latitude volcanic eruptions on enso and amoc, *PNAS*, *112*, 13,784–13,788, doi:[10.1073/pnas.1509153112](https://doi.org/10.1073/pnas.1509153112).
- Pedlosky, J. (2003), *Waves in the Ocean and Atmosphere*, 260 pp., Springer.
- Pedro, J., M. Jochum, C. Buizert, F. He, S. Barker, and S. Rasmussen (2018), Beyond the bipolar seesaw: Toward a process understanding of interhemispheric coupling, *Quat. Sci. Rev.*, *192*, 27–46, doi:[10.1016/j.quascirev.2018.05.005](https://doi.org/10.1016/j.quascirev.2018.05.005).
- Peltier, W., and G. Vettoretti (2014), Dansgaard-Oeschger oscillations predicted in a comprehensive model of glacial climate: A "kicked" salt oscillator in the Atlantic, *Geophys. Res. Lett.*, *41*, 7306–7313, doi:[10.1002/2014GL061413](https://doi.org/10.1002/2014GL061413).
- Petersen, S., D. Schrag, and P. Clark (2013), A new mechanism for dansgaard-oeschger cycles, *Paleoceanography*, *28*, 24–30, doi:[10.1029/2012PA002364](https://doi.org/10.1029/2012PA002364).
- Pollmann, F., C. Eden, and D. Olbers (2017), Evaluating the global internal wave model idemix using finestructure methods, *J. Phys. Oceanogr.*, *47*, 2267–2289.
- Polzin, K. (2009), An abyssal recipe, *Ocean Modell.*, *30*, 298–309, doi:[10.1016/j.ocemod.2009.07.006](https://doi.org/10.1016/j.ocemod.2009.07.006).
- Polzin, K., and Y. Lvov (2011), Toward regional characterizations of the oceanic internal wave field, *Rev. Geophys.*, *49*, RG4003, doi:[10.1029/2010RG000329](https://doi.org/10.1029/2010RG000329).
- Polzin, K., J. Toole, and R. Schmitt (1995), Finescale parameterizations of turbulent dissipation, *J. Phys. Oceanogr.*, *25*, 306–328, doi:[10.1175/1520-0485\(1995\)025<0306:FPOTD>2.0.CO;2](https://doi.org/10.1175/1520-0485(1995)025<0306:FPOTD>2.0.CO;2).
- Polzin, K., J. Toole, J. Ledwell, and R. Schmitt (1997), Spatial variability of turbulent mixing in the abyssal ocean, *Science*, *276*, 93–96, doi:[10.1126/science.276.5309.93](https://doi.org/10.1126/science.276.5309.93).
- Rahmstorf, S., and M. England (1997), Influence of southern hemisphere winds on north atlantic deep water flow, *J. Phys. Oceanogr.*, *27*, 2040–2054, doi:[10.1175/1520-0485\(1997\)027<2040:IOSHWO>2.0.CO;2](https://doi.org/10.1175/1520-0485(1997)027<2040:IOSHWO>2.0.CO;2).
- Rasmussen, S. O., M. Bigler, S. P. Blockley, T. Blunier, S. L. Buchardt, H. B. Clausen, I. Cvijanovic, D. Dahl-Jensen, S. J. Johnsen, H. Fischer, V. Gkinis, M. Guillevic, W. Z. Hoek, J. J. Lowe, J. B. Pedro, T. Popp, I. K. Seierstad, J. P. Steffensen, A. M. Svensson, P. Vallenga, B. M. Vinther, M. J. Walker, J. J. Wheatley, and M. Winstrup (2014), A stratigraphic framework for abrupt climatic changes during the last glacial period based on three synchronized greenland ice-core records: refining

- and extending the intimate event stratigraphy, *Quaternary Science Reviews*, *106*, 14–28, doi:<https://doi.org/10.1016/j.quascirev.2014.09.007>.
- Redi, M. H. (1982), Oceanic isopycnal mixing by coordinate rotation, *J. Phys. Oceanogr.*, *12*, 1154–1158.
- Samelson, R. (1998), Large-scale circulation with locally enhanced vertical mixing, *J. Phys. Oceanogr.*, *28*, 712–726, doi:[10.1175/1520-0485\(1998\)028<0712:LSCWLE>2.0.CO;2](https://doi.org/10.1175/1520-0485(1998)028<0712:LSCWLE>2.0.CO;2).
- Sandström, J. (1908), Dynamische verusche mit meerwasser, *Annals in Hydrodynamic Marine Meteorology*, *1*, 6–23.
- Sarmiento, J., and N. Gruber (2006), *Ocean Biogeochemical Dynamics*, 503 pp., Princeton University Press.
- Sarmiento, J., and J. Toggweiler (1984), A new model for the role of the oceans in determining atmospheric pCO<sub>2</sub>, *Nature*, *308*, 621–624, doi:[10.1038/308621a0](https://doi.org/10.1038/308621a0).
- Schmittner, A. (2005), Decline of the marine ecosystem caused by a reduction in the atlantic overturning circulation, *Nature*, *434*, 628–633, doi:[10.1038/nature03476](https://doi.org/10.1038/nature03476).
- Schmittner, A., and G. Egbert (2014), An improved parameterization of tidal mixing, *Geosci. Model Dev.*, *7*, 211–224, doi:[10.5194/gmd-7-211-2014](https://doi.org/10.5194/gmd-7-211-2014).
- Schmittner, A., and E. Galbraith (2008), Glacial greenhouse-gas fluctuations controlled by ocean circulation changes, *Nature*, *456*, 373–376, doi:[10.1038/nature07531](https://doi.org/10.1038/nature07531).
- Schmittner, A., and D. Lund (2015), Early deglacial atlantic overturning decline and its role in atmospheric CO<sub>2</sub> rise inferred from carbon isotopes  $\delta^{13}\text{C}$ , *Clim. Past*, *11*, 135–152, doi:[10.5194/cp-11-135-2015](https://doi.org/10.5194/cp-11-135-2015).
- Schmittner, A., O. Saenko, and A. Weaver (2003), Coupling of the hemispheres in observations and simulations of glacial climate change, *Quat. Sci. Rev.*, *22*, 659–671, doi:[10.1016/S0277-3791\(02\)00184-1](https://doi.org/10.1016/S0277-3791(02)00184-1).
- Schmittner, A., J. Green, and S. Wilmes (2015), Glacial ocean overturning intensified by tidal mixing in a global circulation model, *Geophys. Res. Lett.*, *42*, 4014–4022, doi:[10.1002/2015GL063561](https://doi.org/10.1002/2015GL063561).
- Scholze, M., W. Knorr, and M. Heimann (2003), Modelling terrestrial vegetation dynamics and carbon cycling for an abrupt climatic change event, *The Holocene*, *13*(3), 327–333, doi:[10.1191/0959683603hl625rp](https://doi.org/10.1191/0959683603hl625rp).

- Seierstad, I. K., P. M. Abbott, M. Bigler, T. Blunier, A. J. Bourne, E. Brook, S. L. Buchardt, C. Buizert, H. B. Clausen, E. Cook, D. Dahl-Jensen, S. M. Davies, M. Guillevic, S. J. Johnsen, D. S. Pedersen, T. J. Popp, S. O. Rasmussen, J. P. Severinghaus, A. Svensson, and B. M. Vinther (2014), Consistently dated records from the greenland grip, gisp2 and ngrip ice cores for the past 104 ka reveal regional millennial-scale  $\delta^{18}\text{O}$  gradients with possible heinrich event imprint, *Quaternary Science Reviews*, *106*, 29 – 46, doi:<https://doi.org/10.1016/j.quascirev.2014.10.032>.
- Shields, C., D. Bailey, G. Danabasoglu, M. Jochum, J. Kiehl, S. Levis, and S. Park (2012), The low-resolution CCSM4, *J. Climate*, *25*, 3993–4014, doi:[10.1175/JCLI-D-11-00260.1](https://doi.org/10.1175/JCLI-D-11-00260.1).
- Siegenthaler, U., and T. Wenk (1984), Rapid atmospheric CO<sub>2</sub> variations and ocean circulation, *Nature*, *308*, 624–626, doi:[10.1038/308624a0](https://doi.org/10.1038/308624a0).
- Sigman, D., and E. Boyle (2000), Glacial/interglacial variations in atmospheric carbon dioxide, *Nature*, *407*, 859–869, doi:[10.1038/35038000](https://doi.org/10.1038/35038000).
- Simmons, H., S. Jayne, L. St. Laurent, and A. Weaver (2004), Tidally driven mixing in a numerical model of the ocean general circulation, *Ocean Modell.*, *6*, 245–263, doi:[10.1016/S1463-5003\(03\)00011-8](https://doi.org/10.1016/S1463-5003(03)00011-8).
- Skinner, L., S. Fallon, C. Waelbrock, E. Michel, and S. Barker (2010), Ventilation of the deep southern ocean and deglacial CO<sub>2</sub> rise, *Science*, *328*, 1147–1151, doi:[10.1126/science.1183627](https://doi.org/10.1126/science.1183627).
- Smith, R., P. Jones, B. Briegleb, F. Bryan, G. Danabasoglu, J. Dennis, J. Dukowicz, C. Eden, B. Fox-Kemper, P. Gent, M. Hecht, S. Jayne, M. Jochum, W. Large, K. Lindsay, M. Maltrud, N. Norton, S. Peacock, M. Vertenstein, and S. Yeager (2010), *The Parallel Ocean Program (POP) reference manual*.
- St. Laurent, L., J. Toole, and R. Schmitt (2001), Buoyancy forcing by turbulence above rough topography in the abyssal brazil basin, *Jour. Phys. Oceanogr.*, *31*, 3476–3495, doi:[10.1175/1520-0485\(2001\)031<3476:BFBTAR>2.0.CO;2](https://doi.org/10.1175/1520-0485(2001)031<3476:BFBTAR>2.0.CO;2).
- St. Laurent, L., H. Simmons, and S. Jayne (2002), Estimating tidally driven mixing in the deep ocean, *Geophys. Res. Letters*, *29(23)*, 2106, doi:[10.1029/2002GL015633](https://doi.org/10.1029/2002GL015633).
- Steffensen, J., et al. (2008), High-Resolution Greenland Ice Core Data Show Abrupt Climate Change Happens in Few Years, *Science*, *321*, 680–684, doi:[10.1126/science.1157707](https://doi.org/10.1126/science.1157707).

- Stephens, B., and R. Keeling (2000), The influence of Antarctic sea ice on glacial-interglacial CO<sub>2</sub> variations, *Nature*, *404*, 171–174, doi:[10.1038/35004556](https://doi.org/10.1038/35004556).
- Stocker, T., and S. Johnsen (2003), A minimum thermodynamic model for the bipolar seesaw, *Paleoceanography*, *18* (4), 1087, doi:[10.1029/2003PA000920](https://doi.org/10.1029/2003PA000920).
- Takahashi, T., et al. (2009), Climatological mean and decadal change in surface ocean pCO<sub>2</sub>, and net sea-air CO<sub>2</sub> flux over the global oceans, *Deep Sea Res.*, *56*, 554–577, doi:[10.1016/j.dsr2.2008.12.009](https://doi.org/10.1016/j.dsr2.2008.12.009).
- Talley, L. (2013), Closure of the global overturning circulation through the Indian, Pacific, and Southern Oceans: Schematics and transports, *Oceanography*, *26*, 80–97, doi:[10.5670/oceanog.2013.07](https://doi.org/10.5670/oceanog.2013.07).
- Toggweiler, J. (1999), Variation of atmospheric CO<sub>2</sub> by ventilation of the ocean's deepest water, *Paleoceanography*, *14*, 571–588, doi:[10.1029/1999PA900033](https://doi.org/10.1029/1999PA900033).
- Toggweiler, J., and B. Samuels (1995), Effects of Drake Passage on the global thermohaline circulation, *Deep-Sea Res.*, *42*, 477–500, doi:[10.1016/0967-0637\(95\)00012-U](https://doi.org/10.1016/0967-0637(95)00012-U).
- Toggweiler, J., and B. Samuels (1998), On the ocean's large-scale circulation near the limit of no vertical mixing, *J. Phys. Oceanogr.*, *28*, 1832–1852, doi:[10.1175/1520-0485\(1998\)028<1832:OTOSLS>2.0.CO;2](https://doi.org/10.1175/1520-0485(1998)028<1832:OTOSLS>2.0.CO;2).
- Toggweiler, J., R. Murnane, S. Carson, A. Gnanadesikan, and J. Sarmiento (2003a), Representation of the carbon cycle in box models and GCMs: 2. Organic pump, *Global Biogeochem. Cycles*, *17*(1), 1027, doi:[10.1029/2001GB001841](https://doi.org/10.1029/2001GB001841).
- Toggweiler, J., A. Gnanadesikan, S. Carson, R. Murnane, and J. Sarmiento (2003b), Representation of the carbon cycle in box models and GCMs: 1. Solubility pump, *Global Biogeochem. Cycles*, *17*(1), 1026, doi:[10.1029/2001GB001401](https://doi.org/10.1029/2001GB001401).
- Toggweiler, J., J. Russell, and S. Carson (2006), Midlatitude westerlies, atmospheric CO<sub>2</sub>, and climate change during the ice ages, *Paleoceanography*, *21*, PA2005, doi:[10.1029/2005PA001154](https://doi.org/10.1029/2005PA001154).
- Volk, T., and M. Hoffert (1985), Ocean Carbon Pumps: Analysis of relative strengths and efficiencies in Ocean-driven Atmospheric CO<sub>2</sub> changes, in *The Carbon Cycle and Atmospheric CO<sub>2</sub>: Natural Variations Archean to Present*, *Geophysical Monograph Series*, vol. 32, edited by E. Sundquist and W. Broecker, pp. 99–110, American Geophysical Union (AGU), doi:[10.1029/GM032p0099](https://doi.org/10.1029/GM032p0099).

- WAIS Divide Project Members (2015), Precise inter-polar phasing of abrupt climate change during the last ice age, *Nature*, *520*, 661–665, doi:[10.1038/nature14401](https://doi.org/10.1038/nature14401).
- Wang, X., A. A.S., R. Edwards, H. Cheng, E. Ito, and M. Solheid (2006), Inter-hemispheric anti-phasing of rainfall during the last glacial period, *Quat. Sci. Rev.*, *25*, 3391–3403, doi:[10.1016/j.quascirev.2006.02.009](https://doi.org/10.1016/j.quascirev.2006.02.009).
- Wang, Y., H. Cheng, R. Edwards, A. An, J. Wu, C.-C. Shen, and J. Dorale (2001), A high-resolution absolute-dated late pleistocene monsoon record from hulu cave, china, *Science*, *294*, 2345–2348, doi:[10.1126/science.1064618](https://doi.org/10.1126/science.1064618).
- Wanninkhof, R. (1992), Relationship between wind speed and gas exchange over the ocean, *J. Geophys. Res.*, *97*, 7373–7382, doi:[10.1029/92JC00188](https://doi.org/10.1029/92JC00188).
- Waterhouse, A. F., et al. (2014), Global patterns of diapycnal mixing from measurements of the turbulent dissipation rate, *J. Phys. Oceanogr.*, *44*, 1854–1872, doi:[10.1175/JPO-D-13-0104.1](https://doi.org/10.1175/JPO-D-13-0104.1).
- Weiss, R. (1974), Carbon dioxide in water and seawater: The solubility of a non-ideal gas, *Mar. Chem.*, *2*, 203–215, doi:[10.1016/0304-4203\(74\)90015-2](https://doi.org/10.1016/0304-4203(74)90015-2).
- Whalen, C., L. Talley, and J. MacKinnon (2012), Spatial and temporal variability of global ocean mixing inferred from argo profiles, *Geophys. Res. Lett.*, *39*, L18,612, doi:[10.1029/2012GL053196](https://doi.org/10.1029/2012GL053196).
- Williams, R., and M. Follows (2011), *Ocean Dynamics and the Carbon Cycle*, 404 pp., Cambridge University Press.
- Wilmes, S.-B., and J. Green (2014), The evolution of tides and tidal dissipation over the past 21,000 years, *J. Geophys. Res.*, *119*, 4083–4100, doi:[10.1002/2013JC009605](https://doi.org/10.1002/2013JC009605).
- Wunsch, C. (1998), The work done by the wind on the oceanic general circulation, *J. Phys. Oceanogr.*, *28*, 2332–2340, doi:[10.1175/1520-0485\(1998\)028<2332:TWDBTW>2.0.CO;2](https://doi.org/10.1175/1520-0485(1998)028<2332:TWDBTW>2.0.CO;2).
- Wunsch, C., and R. Ferrari (2004), Vertical mixing, energy, and the general circulation of the oceans, *Annu. Rev. Fluid Mech.*, *36*, 281–314, doi:[10.1146/annurev.fluid.36.050802.122.121](https://doi.org/10.1146/annurev.fluid.36.050802.122.121).
- Xu, Z., P. Chang, I. Richter, W. Kim, and G. Tang (2014), Diagnosing southeast tropical atlantic sst and ocean circulation biases in the cmip5 ensemble, *Clim Dyn*, *43*, 3123–3145, doi:[10.1007/s00382-014-2247-9](https://doi.org/10.1007/s00382-014-2247-9).

Yeager, S., C. Shields, W. Large, and J. Hack (2006), The Low-Resolution CCSM3, *J. Climate*, 19, 2545-2566, doi:[10.1175/JCLI3744.1](https://doi.org/10.1175/JCLI3744.1).

Zhang, X., G. Knorr, G. Lohmann, and S. Barker (2017), Abrupt North Atlantic circulation changes in response to gradual CO<sub>2</sub> forcing in a glacial climate state, *Nat. Geosci.*, 10, 518-524, doi:[10.1038/NGEO2974](https://doi.org/10.1038/NGEO2974).



# Appendix

## A List of acronyms

AABW	Antarctic bottom water
ACC	Antarctic Circumpolar Current
ADCP	Acoustic Doppler Current Profiler
AIM	Antarctic Isotope Maxima
AMOC	Atlantic Meridional Overturning Circulation
AOU	Apparent oxygen utilization
BCE	Before the Common Era
CAM	Community Atmosphere Model
CE	Common Era
CCSM	Community Climate System Model
CTD	Conductivity-Temperature-Depth
DIC	Dissolved inorganic carbon
DO event	Dansgaard-Oeschger event
EKE	Eddy Kinetic Energy
GCM	General Circulation Model
GM	Garrett and Munk
IDEMIX	Internal wave, dissipation, energy and mixing
ITCZ	Intertropical convergence zone
KPP	K-Profile Parameterization
MOC	Meridional Overturning Circulation
NIW	Near-inertial waves
NPZD	Nutrient, phytoplankton, zooplankton, detritus
Pg	Petagram
PMOC	Indo-Pacific Meridional Overturning Circulation
POP2	Parallel Ocean Program
ppmv	Parts per million by volume
Sv	Sverdrup
SST	Sea surface temperature
TW	Terawatt
WKB	Wentzel-Kramers-Brillouin
WOA	World Ocean Atlas

## B List of figures

- 2.1 The GRIP  $\delta^{18}\text{O}$  record ([Dansgaard et al., 1993](#))
- 2.3 Schematic of the surface ocean chemistry
- 2.2 Column model IDEMIX mixing profiles
- 4.1 Southern Ocean wind stress forcing profiles
- 4.2 Spatial structure of diffusivity in CONT and IDE
- 4.3 Histogram of diffusivities and global averaged diffusivity profiles
- 4.4 Global average dissipation of CONT, IDE, IEDDY and observations ([Kunze, 2017](#))
- 4.5 SST and precipitation differences between IDE and CONT
- 4.6 Zonally averaged temperature and temperature difference between IDE and CONT
- 4.7 Time evolution of AMOC strength for forced simulations
- 4.8 Forced simulation Indo-Pacific overturning stream functions
- 5.1 Surface ocean-atmosphere fluxes of carbon for STLA and CONT
- 5.2 Basin averaged carbon inventory decomposition for STLA
- 5.3 Basin averaged carbon inventory decomposition differences between CONT and STLA
- 6.1 Surface temperature difference between THEN and CONT
- 6.2 Zonally averaged temperature difference and stratification profiles for THEN and CONT
- 6.3 Greenland and Antarctic temperature, atmospheric  $\text{pCO}_2$  and cumulative fluxes
- 6.4 Land flux of carbon and precipitation difference between THEN and CONT
- 6.5 Ocean fluxes of carbon in CONT and difference between THEN and CONT
- 6.6 Basin integrated cumulative carbon flux difference
- 6.7 DIC and  $\text{PO}_4$  in CONT and THEN
- 6.8 Chlorophyll difference
- 7.1 Calculated insolation over the last glacial ([Laskar et al., 2004](#))
- 7.2 Seasonal insolation differences
- 7.3 Relative stratification profiles
- 7.4 Relative vertical diffusivity profiles
- 7.5 Relative dissipation profiles
- 7.6 Export production differences between IDEMIX runs
- 7.7 Averaged vertical dissipation profiles for CONT, TIDE and IEDDY
- 7.8 Export production differences and relative  $\text{PO}_4$  concentrations for TIDE and IEDDY
- 7.9 Sea ice export as function of insolation and summer temperatures

## C List of tables

- 3.1 Full overview of all model simulations discussed in the thesis
- 4.1 Overview of model runs in Chapter 4
- 4.2 Overview of Overturning strengths in forced simulations
- 5.1 Overview of model runs in Chapter 5
- 6.1 Overview of model runs in Chapter 6
- 6.2 Carbon fluxes of CONT, THEN and estimates (*Gruber et al., 2009*)
- 7.1 Overview of model runs of changed insolation forcings
- 7.2 Overview of carbon pump strengths using different insolation forcing
- 7.3 Overview of model runs with changed internal wave forcing